COMPLEX DEFORMATIONS OF BIOLOGICAL SOFT TISSUE: TENDONS AND LIGAMENTS

A THESIS SUBMITTED TO THE UNIVERSITY OF MANCHESTER
FOR THE DEGREE OF DOCTOR OF PHILOSOPHY
IN THE FACULTY OF SCIENCE AND ENGINEERING

2022

James Gregory

Department of Mathematics

Contents

Word Count: 33212

List of Tables

List of Figures

Abstract

COMPLEX DEFORMATIONS OF BIOLOGICAL SOFT TISSUE: TENDONS AND LIGAMENTS

James Gregory

A thesis submitted to The University of Manchester
for the degree of Doctor of Philosophy, 2022

Tendons and ligaments are fibrous soft tissues which are vital for the structural and mechanical integrity of the human body. They possess a unique hierarchical microstructure, starting at the smallest scale with collagen molecules which aggregate to form collagen fibrils – the most important mechanical component of tendons and ligaments, whose crimped geometry gives rise to complex non-linear stress-strain behaviour at the macroscale. Achieving a complete understanding of the relationship between the micro- and macroscale mechanics of these tissues is of interest to research groups spanning the fields of mathematics, material science, biology, and engineering. Accurate and reliable mathematical models of tendons and ligaments can be applied to predict internal stress distributions *in vivo*, a feat not possible through direct experimentation alone, providing valuable information to clinicians in instances of tissue damage and rupture.

When researchers mathematically model tendons and ligaments, simplifying assumptions – such as incompressibility and transverse isotropy – have to be made. In the first part of this thesis, we analyse common assumptions by conducting finite element modelling of tendons and ligaments in idealised geometries. We show that if the direction of the collagen fibres is not carefully considered, unrealistic stress concentrations can form around the edge of the narrowest part of the tendon. We also evaluate the use of the isotropic von Mises yield criterion as an indicator of failure in soft tissue by comparing it with the anisotropic Hill yield criterion. We show that these two criteria produce different failure behaviour, adding to the emerging narrative that isotropic

failure criteria are not suitable for biological soft tissues.

In the second part of this thesis, we look more closely at failure in tendons and ligaments. We present a new microstructural model, based on the distribution of collagen fibril failure properties, which can produce the full range of stress-strain behaviour observed experimentally. Our model can account for certain features that existing models cannot capture, such as stress plateaus and step-like failure, whilst only including parameters that could, in principle, be measured experimentally. We fit our model to stress-strain data obtained from failure tests of mouse tail tendon fascicles and find good agreement. Most importantly, the parameter values found through fitting align with experimentally-obtained values within the literature.

Declaration

No portion of the work referred to in this thesis has been submitted in support of an application for another degree or qualification of this or any other university or other institute of learning.

Copyright

Acknowledgements

Thank you to Tom and Andrew – your help and support over the last three years is hugely appreciated. I am incredibly proud of what I have achieved over the course of my PhD and I could not have asked for better supervisors.

I also wish to thank my mum and dad for their constant support and for always trusting my decisions. Finally, thank you Zoey for your love and patience. I could not have got through this without you.

Dedicated to Bill.

Chapter 1

Introduction

Soft tissues are biological structures which serve an important purpose within the body – connecting and protecting the vital organs and skeleton/muscular systems that keep us alive and moving. From skin and muscle to blood vessels and body fat, each soft tissue possesses a unique arrangement of cells and microstructural components which allows it to fulfil a specific purpose within the body.

The focus of this thesis is on tendons and ligaments – fibrous soft tissues that join bone to muscle and bone to bone, respectively. These strong bands of connective tissue are key to the structural integrity of the body, with ligaments providing stability and support to joints, and tendons facilitating movement through the transmission of force from muscle to bone. Central to the strength of tendons and ligaments is their hierarchy of collagen-based microstructural components [1]. At the smallest scale, we see long collagen molecules arranged parallel to one another, grouping to form fibrils. Groups of fibrils are embedded within an extra-collagenous matrix of cells, proteins, and other molecules [2], and surrounded by a thin layer of connective tissue called the endotendineum – resulting in a fascicle. Finally, tendons and ligaments are comprised of several fascicles bound together, as shown in Figure 1.1.

This highly organised structure causes the tissue to have a high strength in the direction of the fascicles, allowing it to withstand the large forces experienced within the body during high impact activities such as running and jumping. Furthermore, it has been shown that collagen fibrils have differing degrees of waviness, commonly referred to as fibril crimp [3]. This non-uniform waviness means that as the tissue is subjected to

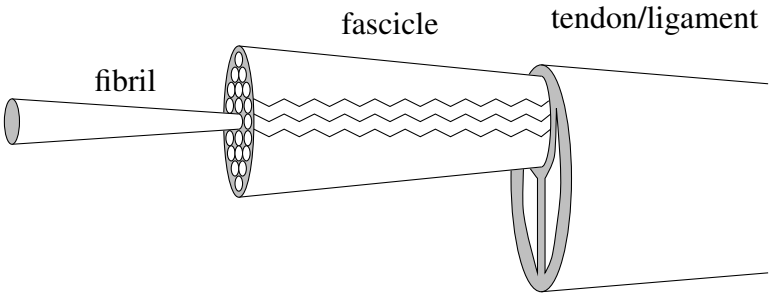

Figure 1.1: Crimped fibrils group together to form fascicles, which are bound together to form a tendon/ligament.

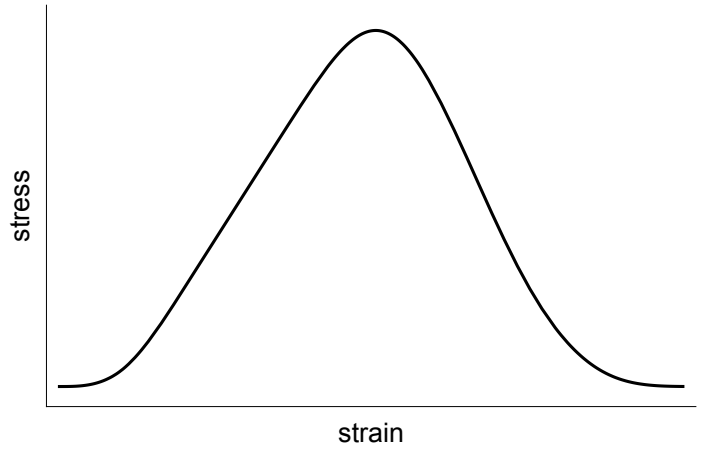

Figure 1.2: Typical stress-strain curve of a tendon/ligament stretched to failure. As the tissue is stretched, fibrils begin to become taut and the stiffness of the tendon increases. Eventually all fibrils become taut and the tissue exhibits a linear response until it yields.

higher strains, its stiffness increases due to the gradual tautening and recruitment of fibrils – allowing for the free movement of joints at low strains, whilst providing a higher degree of resistance at larger strains where permanent damage is more likely to occur. This mechanism leads to the distinctive non-linear stress-strain curve observed when tendons and ligaments are stretched, as shown in Figure 1.2.

Determining any sort of relationship between the microstructure and the macroscale mechanical behaviour of tendons and ligaments can be challenging due to their complex geometry and loading conditions, and the fact that they cannot be extracted and studied without compromising their structural integrity. It is therefore necessary to deploy mathematical modelling techniques to fully understand how the mechanical behaviour

of tendons and ligaments is influenced by their microstructure, and to make any predictions about how the tissue may respond under some specified load. Mathematical modelling of tendons and ligaments has useful applications in medicine, particularly in reconstructive surgery where large-scale experiments are time-consuming, expensive, and fraught with ethical concerns. Consider the anterior cruciate ligament (ACL) of the knee. At an estimated incidence of 30 to 78 per 100,000 people [4], ACL rupture is a common and devastating injury acquired during high impact activities. The ACL cannot heal naturally *in vivo* and therefore, in the most serious of cases where there is a large tear or complete rupture, surgical intervention is required to maintain joint stability. To repair a ruptured ACL, surgeons will typically use an autograft from the patient's patellar tendon or hamstring tendon [5]. A sample of tissue is extracted and fixed between the tibia and femur, acting as a replacement to the ACL and providing stability to the knee. There are many variables at play in this surgery, for example: the length of the graft, the source of the graft, the attachment site, and the graft fixations [6]. Determining the optimal combination of these parameters through experimentation alone is unfeasible, as different patients will have different joint geometries, degrees of activeness, and levels of willingness to adhere to post-surgery rehabilitation guidelines. The development of realistic mathematical models, capable of predicting the internal stresses in complex ligament geometries, has allowed research groups to investigate the effects of some of these parameters without the need for large patient trials. The effects of graft material [7], graft diameter [8], and attachment site [9] have all been investigated, providing clinicians with useful information about the internal mechanics of the replacement tissue that cannot be found through experimentation alone.

To determine the internal stresses in a tendon or ligament, it is important to have an accurate mathematical description of the underlying tissue. The study of the mechanical properties of biological soft tissue dates back to the early 19th century at least. In 1809, Thomas Young presented a lecture to the Royal Society entitled 'On the functions of the heart and arteries' [10], where the general elastic properties of arterial wall tissue were discussed in relation to blood flow. Young postulated that the tissue is perfectly elastic at low strains, meaning that the stress in the tissue is directly proportional to the strain, but suggested that at higher strains the material may "exhibit a force in tension proportional to the excess of the square, or the cube of their length". This statement is true for tendons when we consider small strains, but as we continue to stretch the tissue beyond the end

of its non-linear region, we see a macroscale linear region emerge as shown in Figure 1.2. This is followed by strain-softening as the tissue begins to yield. Young places emphasis on the need to combine both experimental and theoretical approaches to ensure that predictions are sensible and consistent with observation. Development of more sophisticated elastic and inelastic models of soft tissue began to accelerate with the advent of modern continuum mechanics in the 1950s [11]. Due to the small size of collagen fibrils (50–500nm [12]) relative to the tendon itself, using the continuum approximation is appropriate when modelling the tissue as a whole. Authors typically assume that soft tissue is hyperelastic, meaning that elastic deformations are adiabatic and that a single expression – the strain energy function – can be used to describe the constitutive behaviour of the tissue. In 1967, the first strain energy function derived specifically for soft tissue was introduced by Fung [13]. This constitutive model assumed that the stress in the tissue is exponential at large strains, providing a way to capture the non-linear behaviour predicted years earlier by Young. Many other constitutive models have been introduced in the intervening years (see Chapter 2 for more details), and a significant proportion of these are derived based solely on the shape of the stress-strain curved obtained through tensile testing, with material parameters that must be found by fitting the model to experimental data. These types of models are referred to as phenomenological, and since their parameter values cannot be independently measured, they cannot easily be used to relate the macro- and micro-scale mechanical behaviour. In contrast, mathematical models based explicitly on the tissue microstructure can be used to make useful predictions about the mechanical behaviour at the macroscale, provided we possess some microstructural information. Unfortunately, microstructural models are often more complicated, and as a result, research groups tend to favour phenomenological models when considering more complex problems.

In the 1990s, soft tissue mechanicians began to utilise the power of computers to solve more complicated modelling problems with realistic geometries and loading conditions [14]. The finite element method, a numerical method for solving systems of differential equations in complex geometries, became the default option for solving these types of problems. Finite element modelling boasted high accuracy, as demonstrated through its regular usage in other fields of engineering and mathematics. It was shown that the finite element method could be used to provide new insight into the internal

stress distributions present within tendons and ligaments – a feat not previously possible through experimentation. Over the years since then, research groups have used finite element modelling to investigate the mechanics of different tendons, ligaments, and even whole joints (see Chapter 3 for more details).

The first aim of this thesis is to evaluate common assumptions made during finite element modelling to see if they are valid, and to suggest alternatives if they are not. We seek to use mathematical models which capture as much of the microstructure as possible, with the aim to relate observed macroscale behaviour to microscale mechanics – increasing the likelihood that the results are useful to researchers working outside of numerical disciplines.

In Chapter 2, we provide a more detailed biological background and introduce the mathematics required to model the mechanical behaviour of tendons and ligaments. We discuss the internal structure of these tissues, focussing on the all-important collagen fibril. We show how the macroscale behaviour is influenced by the microstructure, and present ideas that are important when it comes to constitutive modelling, such as fibril continuity and cross-linking. A mathematical background follows, beginning with an outline of non-linear solid mechanics – the framework used for soft tissue modelling. Some of the constitutive models found in the literature are then presented and their assumptions discussed, before a model is selected for use in the following chapters.

Chapter 3 concerns finite element modelling of tendons and ligaments. We begin with a literature review, highlighting the areas where common modelling choices and assumptions may impact the results. The first of these areas is in the choice of constitutive model used. In the examples we reviewed, we found that the majority of authors used phenomenological constitutive models rather than microstructural models, precluding the model from being able to predict the effects of potential microstructural changes. We also found that the direction of the collagen fibres is either not discussed, or unrealistic given the geometry used to represent the tissue, and that an isotropic stress measure, the von Mises stress, is used extensively to report the internal stress distribution. We then formally introduce the finite element method as applied to non-linear solid mechanics problems. In order to determine the extent to which the identified areas for improvement affect the output of a finite element model, we define an idealised geometry which can be modified using three parameters. We then conduct a convergence study, before investigating the effects of fibre direction within our geometry. We

find that using an unrealistic fibre direction can have a significant effect on the stress distribution, leading to regions of high stress at the surface of the narrowest part of the tissue. When using geometric parameters chosen to approximate the geometry of the Achilles tendon, the maximum value of stress in the direction of the fibres was found to be 31% higher when an unrealistic fibre direction is used. Qualitatively similar stress concentrations have been reported in the literature [15], and we find that correcting the fibre direction to be more realistic removes these stress concentrations completely. Finally, we show that a slight change to the degree of anisotropy in the measure used to represent the stress in the tissue can completely change the predicted location of failure.

In Chapter 4, we present an article entitled "A microstructural model of tendon failure", which has been previously published in the Journal of the Mechanical Behaviour of Biomedical Materials. In this article, we focus on microstructural modelling of failure, beginning with a discussion of the literature and showing how certain experimental behaviour cannot be explained using existing microstructural models. We further demonstrate this by attempting to fit these models to data taken from mechanical tests on murine tail tendon, showing that plateaus and step-like failure behaviour cannot be accounted for. We then present a new model which can account for these features, by incorporating distributions of collagen fibril failure properties. After fitting our new model to the same set of data, we found that we can reduce the average root mean squared error from 4.53MPa to 2.29MPa – a reduction of 49%. Furthermore, we establish that post-yield plateaus in the stress-strain curve can be explained by non-overlapping fibril yield and rupture stretch distributions, whilst over-lapping distributions produce a well-defined peak. Step-like failure behaviour can be introduced by using a multimodal distribution of fibril rupture stretch.

Finally, in Chapter 5, we summarise our findings, present a conclusion, and discuss the natural extensions to our work.

Chapter 2

General background and literature review

2.1 Biological background

2.1.1 Tendons and ligaments

Tendons and ligaments are bands of connective soft tissue which are capable of withstanding high tensile forces. Tendons connect bone to muscle and passively transfer the force generated through muscular contraction to the skeletal system, whilst ligaments connect bone to bone, providing structure and stability to complex joints such as the knee. The strength of these tissues can be attributed to the complex hierarchical structure of their collagen-based components, and understanding the properties of these components is crucial in order to produce mathematical models which are capable of predicting complex behaviour across multiple length scales. The smallest substructure we typically consider when deriving continuum models of tendons and ligaments are collagen fibrils. Bundles of wavy fibrils group to form fascicles, which in turn group to form tendons and ligaments. The wavy pattern observed in collagen fibrils is referred to as crimping, and the amount of crimp present in each fibril can vary throughout the tissue. The fibrils are embedded within an extra-collagenous matrix containing elastin, glycoproteins, proteoglycans, and other macromolecules. Figure 1.1 shows a simple diagram outlining the hierarchical structure of a tendon/ligament.

Crimping in the fibrils plays an important role in the macroscale behaviour of tendons. When a tendon or ligament is stretched, only the fibrils that are taut will be load-bearing. Initially, most of the fibrils are crimped and the tissue stiffness is low. As further stretch is applied, crimp is gradually removed from the fibrils and the stiffness of the tendon increases until all of the fibrils are taut. At this point, the tissue behaves linearly until it yields, when there is a decrease in gradient followed by a peak in stress before the tendon fails. The exact mechanism that leads to macroscale yielding is widely debated but it is thought to be due to yielding in the fibrils or slippage between the fibrils and the matrix. Figure 1.2 shows the typical stress-strain behaviour of a tendon. In the following section, we will focus on the important structural properties of collagen fibrils and how these may influence a mathematical model of tendons and ligaments. For a more detailed discussion of collagen fibril mechanics and tendon failure, see Chapter 4.

2.1.2 Collagen fibrils

2.1.2.1 Structure and continuity

The collagen fibrils found in tendons and ligaments are composed of mostly type-I collagen molecules packed into a periodic array with a molecular stagger equal to some integer multiple of $D = 67$nm. This staggered pattern leads to a characteristic banding in electron microscopy images [16], as illustrated in Figure 2.1, and prevents the fibril from containing regions void of collagen, which would lead to weak spots in the tissue. Fibril diameters can vary from tissue to tissue, but are typically on the order of 10s–100s of nanometres [17]. It is common to see unimodal, bimodal, and even trimodal [18, 19] distributions of fibril diameters within a tendon/ligament. These distributions have been shown to change across both large timescales, e.g. during maturation and ageing [20, 18], and short timescales, e.g. over a circadian cycle [19]. Due to the large number of factors at play, the impact that any changes in diameter distribution have on the macroscale mechanical properties are uncertain. Despite this, Goh et al. [21] were able to relate age-related changes in diameter distribution to the tendons resilience and resistance to rupture.

It is understood that collagen fibrils can range in length from 0.3mm to over 10mm [22]; however, it remains unknown if fibrils are continuous or discontinuous through the length of tendon [23]. This frequently debated question has important consequences

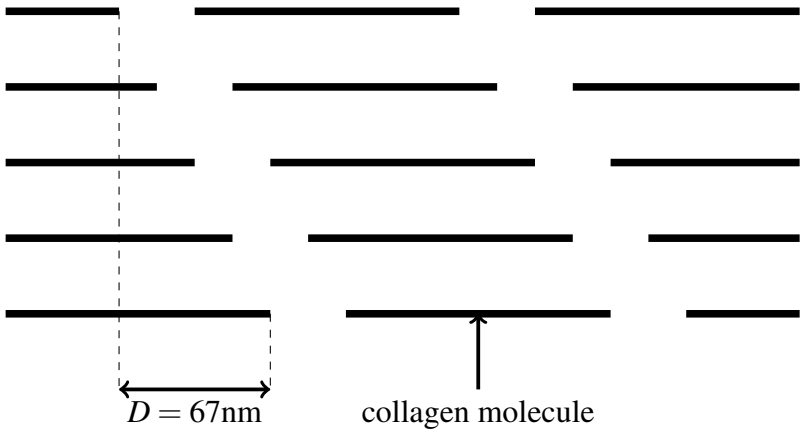

Figure 2.1: An illustration of the staggered pattern of collagen molecules observed within a fibril. Molecules are staggered by multiples of $D = 67$nm.

for multiscale modelling (particularly when conducting inelastic modelling) as it means there is some degree of uncertainty around how forces are transmitted within the tissue. Furthermore, if fibrils are discontinuous then it is argued that the mechanism that leads to yielding is the breakdown of interfibrillar components and the subsequent slippage of fibrils past one another. Whereas if fibrils are continuous, yielding in the tendon would occur due to yielding of the fibrils themselves.

Scanning electron microscopy has been used to image cross-sections of tendon tissue, with authors using various techniques to search for fibril ends, seeking to prove whether fibrils are continuous or not. Provenzano et al. [24] saw no fibril ends whilst looking at images taken from the tendons and ligaments of mature animals from several different species and argue that force transmission in tendons and ligaments occurs through the collagen fibrils themselves rather than through interfibrillar coupling. Svensson et al. [23] provided serial block-face electron microscopy evidence backing up this claim. Images were taken along 67.5mm of combined fibril length from a section of human tendon tissue, where only one fibril end was found. A statistical analysis was carried out which determined it likely that fibrils were structurally continuous. The fibrils were also found to be mechanically continuous, meaning that their length exceeds the critical length required for the fibril itself to yield before it slips within the matrix [25]. The authors conducted a follow-up experiment where collagen fibrils were traced down the entire length of a mouse stapedius tendon, finding them to be structurally

continuous [23]. Hijazi et al. [26] conducted scanning electron microscopy of tendons before and after subjecting them to high loads, during which yielding occurred. Images taken post-loading proved that yielding had occurred in the fibrils themselves and that slippage was not the cause of the macroscale yielding observed.

In contrast, the theory that fibrils are discontinuous is backed up in several papers by Szczensy et al. [27, 28], where a shear-lag model was used along with images of fibrils sliding relative to one another to determine if load is transferred through the fibres or the interfibrillar matrix. It was concluded that yielding occurred due to shearing of the matrix and the sliding of collagen fibrils relative to one another, after the shear lag model provided good estimates of the experimental data. In further experiments carried out by Szczensy et al. [29], tryspin digestion was used to remove extrafibrillar proteins thought to be responsible for transmitting loads between discontinuous collagen fibrils. Whilst it was found that removing these interfibrillar proteins affected the transverse properties of the material, the longitudinal stress response was not reduced. It was claimed that large diameter fibrils are load-bearing whilst smaller diameter fibrils are responsible for transferring load between the larger fibrils. The authors ruled out a number of possible components that could be responsible for transferring load, but there still remained other possible candidates that were not affected by the tryspin digestion, such as elastin and smaller diameter collagen fibrils.

2.1.2.2 Cross-linking

Cross-linking is the term used to describe the intermolecular bonds that form within the network of collagen molecules that make up a fibril. There are two types of bond present, enzymatic and non-enzymatic. During maturation, the presence of the enzyme lysyl oxidase (LOX) leads to the formation of enzymatic cross-links [30]. The concentration of non-enzymatic cross-links increases gradually over time and is therefore related to the age of the tissue. The importance of cross-linking to the mechanical properties of tendons is noted throughout the literature [16, 31]. Researchers have used tendons from rats fed with BAPN, a LOX inhibiting drug, to show that without the presence of enzymatic cross-links, the mechanical properties of the tendon are significantly different [32]. It was found that in the cross-link deficient rats, the tendon stiffness was lower, and the stress-strain curve obtained from stretching a tendon to failure contained

a plateau region.

2.1.3 The extra-collagenous matrix

Within a tendon/ligament, collagen fibrils are embedded within an extra-collagenous matrix consisting of proteoglycans, glycoproteins and elastin molecules. Proteoglycans are composed of a glycosaminoglycan chain bonded to a protein core. They help to support the structure of the tissue and with cell adhesion [33]. Glycoproteins are proteins which have a carbohydrate covalently bonded to them and can serve many biological purposes, including transport and protection [34]. Elastin molecules act as a recoil mechanism for the long collagen chains in soft tissue, pulling them back to their original length when a load has been removed [35].

2.2 Mathematical modelling of soft tissue

Tendons and other soft tissues containing a single family of collagen fibres can be modelled as transversely isotropic, hyperelastic materials [36]. The typical mechanical response of tendons and ligaments was described in Section 2.1.1, where it was shown that nonlinear stress-strain behaviour is observed when the tissue is subjected to strains which fall within the physiological range. In this section, the mathematics needed to describe such a material will be briefly presented, following the notational style of Spencer [37]. At certain points in the following chapters it will be more appropriate to use the notational style of Green and Zerna [38], and it will be made clear to the reader when the notation changes. The equations presented in this section are standard results in the field of nonlinear solid mechanics – for a more detailed derivation, see [37].

2.2.1 Definitions

Suppose we have a body Ω which is subject to some deformation such that at time t the deformed body is denoted by Ω_t. Position vectors to points in Ω and Ω_t are denoted by $\mathbf{X}$ and $\mathbf{x}$, respectively.

The deformation map $\chi : \Omega \to \Omega_t$ describes how the position vectors change under a given deformation, as represented in Figure 2.2. We can define the deformation gradient

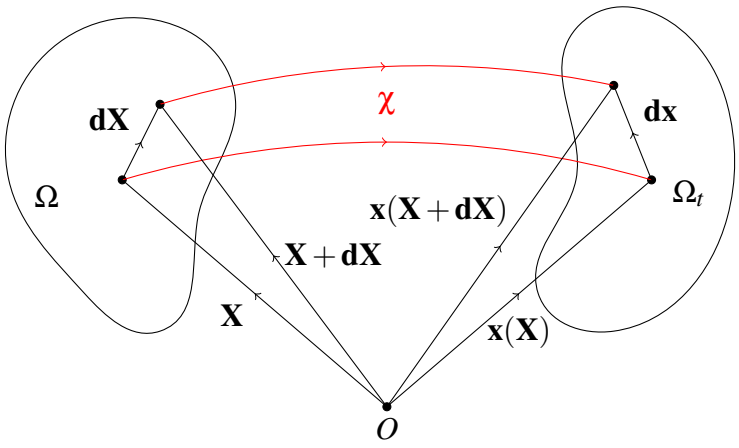

Figure 2.2: Line elements in the undeformed (left) and deformed (right) configurations.

tensor as $\mathbf{F} = \nabla_{\mathbf{X}}\chi$, (i, j)-th component of which is given by

$$\mathrm{F}_{ij} = \frac{\partial \mathrm{x}_i}{\partial \mathrm{X}_j} \tag{2.1}$$

in Cartesian coordinates. The deformation gradient tensor describes how line elements change in length during a deformation. For a body to deform it is not enough that the position vectors change, as this could just correspond to rigid body motion. Line elements are related through the relation

$$\mathbf{dx} = \mathbf{F}\mathbf{dX}. \tag{2.2}$$

A relationship between the square of deformed and undeformed line elements is given by

$$\mathbf{dx} \cdot \mathbf{dx} = (\mathbf{F}\mathbf{dX}) \cdot (\mathbf{F}\mathbf{dX}) = (\mathbf{F}^{\mathrm{T}}\mathbf{F})(\mathbf{dX} \cdot \mathbf{dX}), \tag{2.3}$$

leading to the definition of the right Cauchy-Green deformation tensor $\mathbf{C} = \mathbf{F}^{\mathrm{T}}\mathbf{F}$, and the left Cauchy-Green deformation tensor $\mathbf{B} = \mathbf{F}\mathbf{F}^{\mathrm{T}}$. There are three strain invariants

associated with **C** (and also with **B**). These are

$$I_1 = \mathrm{Tr}(\mathbf{C}), \tag{2.4}$$

$$I_2 = \frac{1}{2}(\mathrm{Tr}(\mathbf{C})^2 - \mathrm{Tr}(\mathbf{C}^2)), \tag{2.5}$$

$$I_3 = \det(\mathbf{C}), \tag{2.6}$$

yielding quantities associated with the deformation which remain the same regardless of the coordinate system used. The third invariant is equal to the square of the ratio between the undeformed and deformed volumes of the body. If the material is incompressible then we have that $I_3 = 1$. By considering a small force $\delta\mathbf{f}$ applied to the surface of an arbitrarily small subset of the deformed body $\delta S_t \subset \partial\Omega_t$ and allowing the area of δS_t to tend to zero, the surface traction at a point can be defined as

$$\mathbf{t} = \lim_{\delta S_t \to 0} \frac{\delta\mathbf{f}}{\delta S_t}. \tag{2.7}$$

The traction **t** at a point with outer unit normal **n** is related to **n** by

$$\mathbf{t} = \sigma\mathbf{n}, \tag{2.8}$$

where σ is the symmetric Cauchy stress tensor, which describes the internal forces acting within the body in its deformed state. We can define the second Piola-Kirchhoff stress by τ by

$$\sigma = \frac{1}{\det(\mathbf{F})}\mathbf{F}\tau\mathbf{F}^{\mathrm{T}}, \tag{2.9}$$

which relates the force in the deformed configuration to areas in the undeformed configuration.

2.2.2 Governing Equations

By considering the conservation of mass through a small region of the body as it undergoes deformation, we arrive at the first governing equation

$$\frac{\rho_0}{\rho} = \det\mathbf{F}, \tag{2.10}$$

where ρ and ρ_0 are the densities in the deformed and undeformed configurations, respectively. By considering the balance of forces acting on the body due to body forces and surface tractions, the equation of motion for the body can be written as

$$\frac{\partial \sigma_{ij}}{\partial \mathrm{x}_j} + \rho F_i^b = \rho a_i, \tag{2.11}$$

where F_i^b and a_i are the i-th components of the body force and acceleration, respectively, and the Einstein summation convention has been applied. By considering the balance of angular momentum on the body it can be shown that the Cauchy stress tensor is symmetric,

$$\sigma_{ij} = \sigma_{ji}. \tag{2.12}$$

The final governing equation is derived by considering energy changes in the system. By balancing the rate at which work is done on the body with changes in heat flux, internal energy and work done by body forces, we arrive at

$$\rho \frac{De}{Dt} = \sigma_{ij} \mathrm{D}_{ij} - \frac{\partial q_i}{\partial \mathrm{x}_i}, \tag{2.13}$$

where e is the internal energy density of the body, $\frac{D}{Dt}(\cdot)$ is the material derivative, D_{ij} is the rate of strain tensor, and q_i is the i-th component of heat flux leaving the body. The material derivative and rate of strain tensor are defined by

$$\frac{D}{Dt}(\cdot) = \frac{\partial}{\partial t}(\cdot) + \mathbf{v} \cdot \nabla(\cdot) \tag{2.14}$$

and

$$\mathrm{D}_{ij} = \frac{1}{2}\left(\frac{\partial v_i}{\partial x_j} + \frac{\partial v_j}{\partial x_i}\right), \tag{2.15}$$

respectively, where $\mathbf{v}$ is the velocity field and the gradient operator is with respect to the deformed coordinates. These governing equations, derived from conservation laws, are given here in Cartesian coordinates but can be rewritten for a general curvilinear coordinate system where appropriate. The above four expressions define a system containing more unknowns than equations. In order to solve the system, we need more information. By introducing material-specific constitutive equations, we can close the system and solve for all unknowns.

2.2.3 Constitutive Equations

Tendons and other soft tissues are often modelled as hyperelastic materials when only the loading path is being considered, or when assuming that the strain rate is very small (quasi-static deformation). The behaviour of a hyperelastic material can be captured with an appropriate strain energy function $W = \rho_0 e$, where ρ_0 is the density in the reference configuration. In nonlinear elasticity, the strain energy function is a function of the deformation gradient, $W = W(\mathbf{F})$. Using this and equation (2.13), for an adiabatic deformation ($\frac{\partial q_i}{\partial \mathrm{x}_i} = 0$), we have

$$\begin{aligned} \frac{\rho}{\rho_0}\frac{DW}{Dt} &= \sigma_{ij} D_{ij} \\ \implies J^{-1}\frac{\partial W}{\partial F_{ij}}\frac{DF_{ij}}{Dt} &= \sigma_{ij} D_{ij}, \end{aligned} \tag{2.16}$$

where $J = \rho_0/\rho$. Replacing D_{ij} with $\frac{\partial v_i}{\partial x_j}$ and using the definition of the deformation gradient (2.1) gives

$$J^{-1}\frac{\partial W}{\partial F_{ij}}\frac{D}{Dt}\left(\frac{\partial x_i}{\partial X_j}\right) = \sigma_{ij}\frac{\partial v_i}{\partial x_j}. \tag{2.17}$$

Changing the order of differentiation and using the definition of the material derivative yields

$$\begin{aligned} J^{-1}\frac{\partial W}{\partial F_{ij}}\frac{\partial}{\partial X_j}\Big(\underbrace{\frac{\partial x_i}{\partial t}}_{=0} + v_k \underbrace{\frac{\partial x_i}{\partial x_k}}_{=\delta_{ik}}\Big) &= \sigma_{ij}\frac{\partial v_i}{\partial x_j} \\ \implies J^{-1}\frac{\partial W}{\partial F_{ij}}\frac{\partial v_i}{\partial X_j} &= \sigma_{ij}\frac{\partial v_i}{\partial x_j} \\ \implies J^{-1}\frac{\partial W}{\partial F_{ij}}\frac{\partial v_i}{\partial x_k}\frac{\partial x_k}{\partial X_j} &= \sigma_{ij}\frac{\partial v_i}{\partial x_j}. \end{aligned} \tag{2.18}$$

This holds true for all $\frac{\partial v_i}{\partial x_j}$, allowing us to write

$$\sigma_{ij} = J^{-1}\mathrm{F}_{jk}\frac{\partial W}{\partial \mathrm{F}_{ki}}. \tag{2.19}$$

At this stage it is useful to write equation (2.13) in terms of components of the right Cauchy-Green tensor, C_{ij}. Writing the left hand side of (2.13) in terms of $C_{ij} = F_{ki}F_{kj}$ gives

$$\begin{aligned} J^{-1}\frac{\partial W}{\partial C_{ij}}\frac{DC_{ij}}{Dt} &= J^{-1}\frac{\partial W}{\partial C_{ij}}\frac{D}{Dt}(F_{ki}F_{kj}) \\ &= J^{-1}\frac{\partial W}{\partial C_{ij}}\frac{D}{Dt}\left(\frac{\partial x_k}{\partial X_i}\frac{\partial x_k}{\partial X_j}\right) \\ &= J^{-1}\frac{\partial W}{\partial C_{ij}}\left(\frac{D}{Dt}\left(\frac{\partial x_k}{\partial X_i}\right)\frac{\partial x_k}{\partial X_j} + \frac{\partial x_k}{\partial X_i}\frac{D}{Dt}\left(\frac{\partial x_k}{\partial X_j}\right)\right) \\ &= J^{-1}\frac{\partial W}{\partial C_{ij}}\frac{D}{Dt}\left(\frac{\partial v_k}{\partial X_i}\frac{\partial x_k}{\partial X_j} + \frac{\partial x_k}{\partial X_i}\frac{\partial v_k}{\partial X_j}\right), \end{aligned} \tag{2.20}$$

which leads to

$$J^{-1}\frac{\partial W}{\partial C_{ij}}\frac{DC_{ij}}{Dt} = 2J^{-1}\frac{\partial W}{\partial C_{ij}}\frac{\partial v_k}{\partial X_i}\frac{\partial x_k}{\partial X_j}. \tag{2.21}$$

Exploiting the symmetry of C_{ij} yields

$$J^{-1}\frac{\partial W}{\partial C_{ij}}\frac{DC_{ij}}{Dt} = J^{-1}\left(\frac{\partial W}{\partial C_{ij}} + \frac{\partial W}{\partial C_{ji}}\right)\frac{\partial v_k}{\partial X_i}\frac{\partial x_k}{\partial X_j}. \tag{2.22}$$

Using the chain rule, we find that

$$\begin{aligned} J^{-1}\frac{\partial W}{\partial C_{ij}}\frac{DC_{ij}}{Dt} &= J^{-1}\left(\frac{\partial W}{\partial C_{ij}} + \frac{\partial W}{\partial C_{ji}}\right)\frac{\partial v_k}{\partial x_l}\frac{\partial x_l}{\partial X_i}\frac{\partial x_k}{\partial X_j} = \sigma_{kl}\frac{\partial v_k}{\partial x_l} \\ \implies \sigma_{kl} &= J^{-1}\left(\frac{\partial W}{\partial \mathrm{C}_{ij}} + \frac{\partial W}{\partial \mathrm{C}_{ji}}\right)\frac{\partial \mathrm{x}_l}{\partial \mathrm{X}_i}\frac{\partial \mathrm{x}_k}{\partial \mathrm{X}_j}, \end{aligned} \tag{2.23}$$

giving us a non-linear stress-strain relationship in terms of W and C_{ij}. This expression can also be written in tensor notation as

$$\boldsymbol{\sigma} = 2J^{-1}\mathbf{F}\cdot\frac{\partial W}{\partial \mathbf{C}}\cdot\mathbf{F}^{\mathrm{T}}. \tag{2.24}$$

For a material with n strain invariants, the derivative of the strain energy can be written as

$$\frac{\partial W}{\partial \mathrm{C}_{ij}} = \sum_{\alpha}^{n} \frac{\partial W}{\partial I_\alpha} \frac{\partial I_\alpha}{\partial \mathrm{C}_{ij}}, \tag{2.25}$$

in Cartesian coordinates using the chain rule. For materials with the same properties in each direction (referred to as isotropic), we have the three strain invariants defined in equations (2.4) – (2.6), whose derivatives are given by

$$\frac{\partial I_1}{\partial \mathrm{C}_{ij}} = \delta_{ij}, \tag{2.26}$$

$$\frac{\partial I_2}{\partial \mathrm{C}_{ij}} = I_1 \delta_{ij} - \mathrm{C}_{ij}, \tag{2.27}$$

$$\frac{\partial I_3}{\partial \mathrm{C}_{ij}} = I_2 \delta_{ij} + I_1 \mathrm{C}_{ij} + \mathrm{C}_{jk}\mathrm{C}_{ki}. \tag{2.28}$$

Inserting these derivatives into (2.23) gives

$$\begin{aligned}
\sigma_{kl} &= 2J^{-1} \left(W_1 \frac{\partial I_1}{\partial C_{ij}} + W_2 \frac{\partial I_2}{\partial C_{ij}} + W_3 \frac{\partial I_3}{\partial C_{ij}} \right) \frac{\partial x_k}{\partial X_i} \frac{\partial x_l}{\partial X_j} \\
&= 2J^{-1} \left(W_1 \delta_{ij} + W_2 (I_1 \delta_{ij} - C_{ij}) + W_3 (I_2 \delta_{ij} + I_1 C_{ij} + C_{jm} C_{mi}) \right) F_{ki} F_{lj} \\
&= 2J^{-1} F_{ki} \left((W_1 + I_1 W_2 + I_2 W_3) \delta_{ij} - (W_2 + I_1 W_3) C_{ij} + W_3 C_{jm} C_{mi} \right) F_{lj},
\end{aligned} \tag{2.29}$$

where $W_i = \frac{\partial W}{\partial I_i}$. Using $J = \det\mathbf{F} = \sqrt{\det\mathbf{C}} = \sqrt{I_3}$, and writing the above in tensor notation leads to

$$\sigma = \frac{2}{\sqrt{I_3}} \mathbf{F} \left((W_1 + I_1 W_2 + I_2 W_3)\mathbf{I} - (W_2 + I_1 W_3)\mathbf{F}^{\mathrm{T}}\mathbf{F} + W_3 (\mathbf{F}^{\mathrm{T}}\mathbf{F})(\mathbf{F}^{\mathrm{T}}\mathbf{F}) \right) \mathbf{F}^{\mathrm{T}}. \tag{2.30}$$

Using $\mathbf{B} = \mathbf{F}\mathbf{F}^{\mathrm{T}}$, we find that

$$\sigma = \frac{2}{\sqrt{I_3}} \left((W_1 + I_1 W_2 + I_2 W_3)\mathbf{B} - (W_2 + I_1 W_3)\mathbf{B}^2 + W_3 \mathbf{B}^3 \right). \tag{2.31}$$

Since soft tissue is made up mostly of water and collagen, we can approximate it as incompressible, allowing us to simplify equation (2.31) further. We set $I_3 = 1$, but must now introduce a Lagrange multiplier $\mathcal{L}(p) = -\frac{1}{2}p$, to account for the degree of freedom

removed by assuming incompressibility. We write

$$W(I_1, I_2, I_3) = \tilde{W}(I_1, I_2) - \frac{1}{2}p(I_3 - 1). \tag{2.32}$$

Using equations (2.31) and (2.32) along with $I_3 = 1$ and the Cayley-Hamilton theorem (given in Appendix A.1), we arrive at the constitutive relation for an incompressible, isotropic, hyperelastic solid [39],

$$\sigma = -p\mathbf{I} + 2W_1\mathbf{B} - 2W_2\mathbf{B}^{-1}. \tag{2.33}$$

Our choice of Lagrange multiplier means that p in equation (2.33) corresponds to the hydrostatic pressure in the tissue.

Tendons and ligaments can be modelled as transversely isotropic materials with a single preferred direction corresponding to the orientation of the collagen fibres. Assuming that the collagen fibres are initially oriented in the direction of the unit vector $\mathbf{M}$, two new strain invariants are introduced,

$$I_4 = \mathbf{M} \cdot \mathbf{CM}, \tag{2.34}$$

$$I_5 = \mathbf{M} \cdot (\mathbf{C}^2\mathbf{M}). \tag{2.35}$$

These strain invariants are related to the square of the stretch in the direction of the fibres. The derivatives of these two strain invariants with respect to C_{ij} are given by

$$\frac{\partial I_4}{\partial \mathrm{C}_{ij}} = \mathrm{M}_i\mathrm{M}_j,$$

$$\frac{\partial I_5}{\partial \mathrm{C}_{ij}} = \mathrm{M}_i\mathrm{C}_{jm}\mathrm{M}_m + \mathrm{M}_k\mathrm{C}_{ki}\mathrm{M}_j.$$

Using these two derivatives and equation (2.23), it can be shown that the constitutive relation for an incompressible, hyperalstic, transversely isotropic solid is given by

$$\sigma = -p\mathbf{I} + 2W_1\mathbf{B} - 2W_2\mathbf{B}^{-1} + 2W_4\mathbf{m}\otimes\mathbf{m} + 2W_5(\mathbf{m}\otimes\mathbf{Bm} + \mathbf{Bm}\otimes\mathbf{m}), \tag{2.36}$$

where $\mathbf{m} = \mathbf{FM}$ is the push forward of the direction vector $\mathbf{M}$.

2.2.4 Viscoelasticity

Soft tissues are examples of viscoelastic solids, exhibiting viscous, as well as elastic, phenomena. This means that the history of strain in a tissue sample affects the current stress. Viscoelastic materials can be modelled as systems containing different combinations of springs and dashpots in series or parallel. A dashpot produces a velocity which is proportional to the force applied to it, thus introducing time dependence into the system. When a viscoelastic solid is suddenly subjected to strain which is then kept constant, the stress in the material decreases over time. This is known as stress relaxation. The phenomenon of creep is observed when a viscoelastic solid is subject to stresses which are kept constant over time, causing the material to continue to deform without an increase in load. Because of these two effects, when tissue samples are subject to periodic loading, the force-displacement graph produced is not the same for loading and unloading. This effect is known as hysteresis and is observed in all soft tissue [13].

A range of viscoelastic models seeking to capture the rate effects observed during tensile testing of soft tissue have been developed alongside the purely elastic models discussed in the following sections. In 1980, Decreamer et al. [40] derived a non-linear viscoelastic constitutive equation for soft biological tissues by assuming that there are internal friction forces acting between the collagen fibres, all of which have identical linear viscoelastic properties. In 2004, Limbert et al. [41] developed a phenomenological constitutive law for the posterior cruciate ligament, assuming the tissue to be anisotropic and viscohyperelastic. A Helmholtz free energy function containing both elastic and viscous parts was used, and the resulting model showed good agreement with experimental results. This model showed a significant improvement over that of Decreamer et al. in that anisotropy was assumed, therefore providing a better representation of the underlying tissue. More recently, Shearer et al. [42] developed a fully microstructural viscoelastic model of tendons. In this work, macroscopic viscoelastic effects such as creep and stress relaxation can be recovered by incorporating viscosity on the microscale in combination with a distribution of fibril critical stretch (the stretch required to tauten the fibril). By using a microstructural approach, the authors were able to predict changes in fibril length distribution over the course of a deformation, a feat not possible using a phenomenological approach.

We choose to ignore viscoelasticity in our modelling – a valid assumption provided deformations are quasi-static [43], and only the loading curve is considered. To fully capture the behaviour of soft tissue during both loading and unloading at different strain rates, it would be necessary to include viscoelastic effects. For further discussions of non-linear viscoelasticity, see [44].

2.2.5 Existing elastic models

The equations outlined in Sections 2.2.1 and 2.2.2 allow us to determine the stress distribution within a tendon or ligament under some prescribed boundary conditions, once a strain energy function has been chosen. Selecting an appropriate constitutive model is one of the most challenging parts of soft tissue modelling, however, as models which seek to accurately represent all aspects of the tissue microstructure can quickly become complex. We therefore find that concessions are often made for the sake of simplicity. In this section we will discuss the constitutive models most commonly used in the field of soft tissue mechanics and evaluate their suitability for modelling tendons and ligaments. We split the models into two categories – phenomenological and microstructural. Phenomenological models contain parameters that must be found through curve fitting and therefore have no physical interpretation. Conversely, microstructural models contain only parameters that could be directly measured from the tissue. In this section we will only consider elastic models which are capable of capturing the behaviour of the tissue up until it yields. For a discussion of inelastic models, which can describe the behaviour of tendons and ligaments beyond their elastic limit, see Chapter 4.

2.2.5.1 Phenomenological

It is common amongst phenomenological models to see the non-linear part of the stress-strain curve being represented by an exponential function. In 1967, Fung [13] published a continuum model of soft tissue, deriving the strain energy function

$$W(I_1) = \frac{\mu}{2b}\left[e^{b(I_1-3)} - 1\right], \tag{2.37}$$

where μ is the ground state shear modulus, b is a constant [45] and it is assumed that the tissue is incompressible. The author points out that this is the simplest model capable of

describing the highly non-linear behaviour exhibited at finite strain. They acknowledge that the concept of Young's modulus is not appropriate for soft tissues as they exhibit non-linear behaviour. However, since this strain energy function only depends on the strain invariant I_1, it is only capable of describing isotropic materials, reducing the extent to which it can be applied to soft tissue. Several years later, Veronda *et al.* introduced a strain energy function similar to Fung's, but with an additional term involving the invariant I_2,

$$W(I_1,I_2) = \alpha e^{\beta(I_1-3)} - \frac{\alpha\beta}{2}(I_2-3), \tag{2.38}$$

where α and β are constants. This model provides a good fit to experimental data, but suffers from the same problems as the strain energy function derived by Fung – it assumes isotropy and is therefore not suitable for modelling anisotropic soft tissues.

In 1996, Weiss *et al.* developed a transversely isotropic strain energy function that is still used extensively in soft tissue modelling to this day. Their strain energy function takes the form

$$W(I_1,I_2,I_4) = C_1(I_1-3) + C_2(I_2-3) + C_3(e^{(I_4)-1} - I_4), \tag{2.39}$$

where C_i are constants. This is an extension of the Mooney-Rivlin strain energy function [46], often used for modelling rubber-like materials, but with an additional term involving I_4 to account for the presence of fibres. This is a significant improvement on the models of Fung and Veronda, because the fibrous structure of the tissue is better-represented.

Another important model is the HGO model, introduced by Holzapfel *et al.* [47] in 2000 to describe arterial wall mechanics, but which can be easily applied to other soft tissues. For a tissue with one family of fibres, the HGO strain energy function is given by

$$W(I_1,I_4) = \frac{c}{2}(I_1-3) + \frac{k_1}{2k_2}\left(e^{k_2(I_4-1)^2} - 1\right), \tag{2.40}$$

where c, k_1, and k_2 are constants. The authors find good qualitative agreement between their model and experimental data obtained from tensile tests on arterial wall tissue. We choose to classify this model as phenomenological, despite the fact that it is derived from microstructural considerations. This is because the material parameters cannot be determined by direct measurement and must be found through curve fitting, making

it difficult to estimate the mechanical properties of a tissue sample without explicitly carrying out tensile tests.

2.2.5.2 Microstructural

Early models based on tissue microstructure typically considered the tissue to be a fibre composite material, with fibril constitutive behaviour derived by considering the undulating shape of the fibrils. In 1975, Beskos and Jenkins [48] modelled collagen fibrils as inextensible helices, resulting in a model that could explain the initial non-linear toe region as stiffening due to the helices being stretched out. This model proved to be unrealistic for large strains, however, as the inextensibility of the fibrils meant that the gradient of the stress-strain curve approached infinity for some finite value of strain. By modelling collagen fibrils as sinusoidal beams, Comninou and Yannas [49] were able to reproduce more of the typical tendon behaviour displayed in Figure 1.2. The non-linear region arose due to the beam increasing in stiffness as the crimp is removed, and the behaviour approached linearity once all beams had been straightened out. Whilst these models are capable of reproducing some of the macroscale properties of tendons, they do not allow for the natural variations in microstructural properties that exist within tendons, such as a varying amount of crimp between fibrils.

A popular framework used to account for the non-linearity of the toe region in soft tissues and allowing for variations in crimp between fibrils, is sequential straightening and loading (SSL). This was first used by Kastelic et al. [3], where tendon tissue was modelled as parallel fibres with a crimp angle θ that varied through the radius of the tendon. The stress in the tendon is computed by considering only the fibrils that have been straightened out for a given tendon stretch. The effect of the matrix is ignored here but can easily be included through the inclusion of an isotropic term. Lanir [50] developed a microstructural viscoelastic model by assuming that soft tissue is a continuum composed of fibres embedded in a fluid matrix. The nonuniform crimping in the fibres is introduced via an undulation density distribution function, accounting for the fact that not all fibres will be load-bearing for part of the deformation. Continuum models which consider the tissue microstructure in their derivation often follow a similar framework – modelling the tissue as an incompressible composite of one-dimensional fibres embedded in an isotropic matrix. In these instances it is common to see the strain energy

function W written as

$$W(I_1, I_4) = W_m(I_1) + W_f(I_4), \tag{2.41}$$

where W_m and W_f are the strain energy functions of the matrix and fibres, respectively. This can be seen in the Weiss and HGO strain energy functions defined in Section 2.2.5.1. A specific form of W_f was derived by Shearer [43, 51], based on the work of Kastelic [3], assuming that the crimp angle is dependent on the radial position of the fibril within the fascicle $\theta = \theta(r)$,

$$W_f(I_4) = \begin{cases} 0 & I_4 < 1, \\ \frac{\phi E}{6\sin^2\theta_0}(4\sqrt{I_4} - 3\log I_4 - \frac{1}{I_4} - 3), & 1 \leq I_4 \leq \frac{1}{\cos^2\theta_0}, \\ \phi E(\beta\sqrt{I_4} - \frac{1}{2}\log I_4 + \eta), & I_4 > \frac{1}{\cos^2\theta_0}, \end{cases} \tag{2.42}$$

where ϕ is the collagen volume fraction, E is the Young's modulus of a collagen fibril, θ_0 is the initial crimp angle at the outside of the fascicle, and η and β are constant functions of θ_0. All of these parameters can, in principle, be measured experimentally, but whilst the model can produce stress-strain plots that capture the full range of macroscale behaviour observed in tendons, the function chosen for $\theta(r)$ is not based on experimental observations.

2.2.6 Yield criteria

We describe materials as elastic if they return to their initial shape after a load has been removed. If we subject an elastic material to high enough stresses, however, we can cause permanent deformation – referred to as plasticity. For simple materials under uniaxial tension or compression (therefore possessing one non-zero component of stress), the onset of failure can be categorised by a single point in stress-strain space, referred to as the elastic limit or yield point. For more complex deformations, the idea of a yield point can be extended to a yield surface, defined by a yield criterion. The Cauchy stress tensor contains six independent components of stress which must all be taken into consideration when evaluating whether a material will yield under complex loading conditions. We can therefore define a surface in 6-dimensional stress-space which will form the boundary between elastic and plastic behaviour. If a stress state falls within the boundary, the deformation is described as elastic, whereas if it falls outside, we refer to

it as plastic. One of the most widely used yield criteria is the von Mises yield criterion [52], defined by

$$\Phi_{\text{vm}}(\sigma) = \sigma_{\text{vm}}^2(\sigma) - \sigma_Y^2 = 0, \tag{2.43}$$

where σ_Y is the yield strength of the material under simple extension/compression, and σ_{vm} is the von Mises stress defined by

$$\sigma_{\text{vm}}^2 = \frac{1}{2}\left[(\sigma_{11}-\sigma_{22})^2 + (\sigma_{22}-\sigma_{33})^2 + (\sigma_{33}-\sigma_{11})^2 + 6(\sigma_{23}^2+\sigma_{31}^2+\sigma_{12}^2)\right]. \tag{2.44}$$

This scalar stress measure was derived for use with isotropic materials, however it is regularly used in soft tissue mechanics[1]. The von Mises yield criterion can be extended to include material anisotropy, as was demonstrated by Hill [53]. We refer to their criterion as the Hill yield criterion and it is expressed as

$$\Phi_{\text{H}}(\sigma) = \sigma_{\text{H}}^2(\sigma) - 1, \tag{2.45}$$

where σ_{H} is the Hill stress, defined by

$$\sigma_{\text{H}}^2 = F(\sigma_{22}-\sigma_{33})^2 + G(\sigma_{33}-\sigma_{11})^2 + H(\sigma_{11}-\sigma_{22})^2 + 2L\sigma_{23}^2 + 2M\sigma_{31}^2 + 2N\sigma_{12}^2, \tag{2.46}$$

where σ_{ij} are the components of the Cauchy stress and F,G,H,L,M,N are constants which must be found experimentally, being related to the strengths of the materials in each direction. If the yield strengths in each direction are given by X, Y and Z, then the constants can be calculated using

$$F = \frac{1}{2}\left(\frac{1}{Y^2}+\frac{1}{Z^2}-\frac{1}{X^2}\right), \tag{2.47}$$

$$G = \frac{1}{2}\left(\frac{1}{Z^2}+\frac{1}{X^2}-\frac{1}{Y^2}\right), \tag{2.48}$$

$$H = \frac{1}{2}\left(\frac{1}{X^2}+\frac{1}{Y^2}-\frac{1}{Z^2}\right). \tag{2.49}$$

[1]See Chapter 4 for more discussion surrounding the application of yield criteria and other failure models to soft tissue.

The remaining three constants are related to the maximum shear strengths of the material,

$$L = \frac{1}{2\tau_{YZ}^2}, \tag{2.50}$$

$$M = \frac{1}{2\tau_{ZX}^2}, \tag{2.51}$$

$$N = \frac{1}{2\tau_{XY}^2}, \tag{2.52}$$

where τ_{YZ}, τ_{ZX}, and τ_{XY} are the yield stresses under shear. This criterion differs from the isotropic yield criterion given in equation (2.43), as the strength of the material can vary in three perpendicular directions, allowing us to model yielding in orthotropic materials. If we assume the material is transversely isotropic, rather than orthotropic, with the z-axis as the direction of anisotropy, the number of constants is reduced, since $F = G$ and $L = M$. Assuming isotropy reduces the Hill criterion to the von Mises criterion.

2.3 Summary

2.3.1 Modelling considerations and assumptions

One of the aims of this thesis is to determine which factors must be taken into consideration when conducting mathematical modelling of tendons and ligaments. In the following chapters, we will explore the extent to which macroscale geometric and microstructural parameters influence the mechanical properties of these tissues. There is a vast amount of literature in the field of soft tissue modelling, and the examples outlined in Section 2.2.5 are some of the most widely adopted models, many of which follow a similar framework, in which the tissue is treated as a fibre composite. We choose to follow the same framework, treating tendons and ligaments as incompressible, transversely isotropic, hyperelastic materials consisting of a family of one-dimensional fibres embedded within an isotropic matrix. We choose to ignore viscous effects, an assumption which is valid if the deformation is carried out at very low strain rates [43], a regime in which hysteresis is minimized.

2.3.2 Choosing a model

In the following chapters, we wish to deploy a simple microstructurally-based constitutive model that will produce comparable results to existing phenomenological models, whilst hopefully providing more insight into the microscale mechanics. We require all material parameters in our model to be measurable in an attempt to move away from phenomenological material parameters. To do this, we will use an SSL approach, similar to Lanir [50] and Shearer [43, 51, 42]. We will assume that collagen fibrils are linearly elastic and have some critical stretch λ_C at which they become taut. The stress in a 1D fibril is therefore given by

$$\sigma_f(\lambda,\lambda_C) = \begin{cases} 0, & \lambda < \lambda_C, \\ E\left(\dfrac{\lambda}{\lambda_C} - 1\right), & \lambda \geq \lambda_C, \end{cases} \tag{2.53}$$

where E is the Young's modulus of a fibril and λ is the macroscale stretch applied to the tissue. We will assume that the critical stretch of the fibrils follows some distribution $\Lambda_C(\lambda_C)$, meaning that the overall stress in the fibres is given by

$$\sigma(\lambda) = \phi \int_1^{\lambda} \sigma_f(\lambda,\lambda_C)\Lambda_C(\lambda_C)\mathrm{d}\lambda_C, \tag{2.54}$$

where ϕ is the collagen volume fraction. There is not enough data available to make an informed decision on the form that Λ_C should take. We therefore choose a simple triangular distribution defined by

$$\Lambda_C(\lambda_C) = \begin{cases} 0, & \lambda_C < a, \\ \dfrac{2(\lambda_C - a)}{(b-a)(c-a)}, & a \leq \lambda_C < c, \\ \dfrac{2(b - \lambda_C)}{(b-a)(b-c)}, & c \leq \lambda_C < b, \\ 0, & \lambda_C \geq b, \end{cases} \tag{2.55}$$

where a is the lower bound, b is the upper bound, and c is the mode. Using a triangular distribution is common in the literature [54] and has the additional benefit of producing

an analytic strain energy function [55]

$$W(I_1, I_4) = (1-\phi)\frac{\mu}{2}(I_1 - 3) + \phi E\left(\frac{A}{2}\log I_4 + (B-D)\sqrt{I_4} + \frac{C}{2}\sqrt{I_4}\log I_4 + F\right), \tag{2.56}$$

where A, B, C, D, and F are piecewise-defined functions of I_4. These functions, along with a derivation of equation (2.56), can be found in Appendix A.2. In the derivation of equation (2.56), we have assumed that the matrix can be represented by a Neo-Hookean solid – an assumption introduced by Holzapfel *et al.* [47] and justified in the work of Gundiah *et al.* [56].

In this chapter we have outlined the mathematics and biology prerequisite for modelling tendons and ligaments. We have chosen a constitutive model based on the tissue microstructure and presented the governing equations of non-linear elasticity, which can now be used to examine more complex deformations. In the next Chapter, we will introduce the finite element method, a mathematical method which can be used to solve systems of PDEs in complex 3D domains. We will use our chosen model to explore the effects of various geometric properties, such as shape and fibre direction, on the macroscale mechanical properties of tendons and ligaments.

Chapter 3

Finite element modelling of tendons and ligaments

3.1 Overview

It is not possible to produce analytic solutions to the governing equations of elasticity (outlined in Section 2.2) within the complex geometries associated with soft tissues such as tendons and ligaments. To produce reliable mathematical models of these tissues, we choose to deploy the finite element method – a numerical method used widely across many fields of science and engineering for its ability to efficiently and accurately solve systems of PDEs in complex, unstructured domains. The finite element method is often used to more efficiently design mechanical components because it can quickly predict the internal stresses without the need of a prototype [57]. When it comes to modelling tendons and ligaments, the finite element method is particularly useful because it allows us to vary the geometric and microstructural properties of the tissue and observe the effects of these changes on the stress distribution within the tissue – a feat not possible through experimentation alone. In Section 3.2, we will introduce the finite element method and discuss its applications in the literature (a summary of these findings can be found in Table 3.1). We will give examples of the types of problems that can be studied using this powerful technique, and critically analyse the underlying constitutive models where appropriate. In Section 3.3, we introduce the mathematics required to understand the finite element method in relation to non-linear solid mechanics problems, before

discussing our specific implementation in Section 3.4. Section 3.5 begins with a simple problem which will form the basis of all of our further modelling – the uniaxial extension of a transversely isotropic, hyperelastic, right circular cylinder. We then discuss how we will vary the geometric and microstructural properties to make the model more realistic. Once we have established the problem we are trying to solve, we will introduce oomph-lib, an open-source finite element library written in C++, and discuss how we will use it to solve our problem. In Section 3.6, we investigate the effects of geometry and fibre direction on the elastic behaviour of tendons by perturbing the initial geometry away from a cylinder, before using geometries based on real tendons and ligaments in Section 3.7. Finally, we will consider a more complex deformation, incorporating a twist applied to the end of the tendon, in order to evaluate the effectiveness of isotropic yield criteria when applied to tendons and ligaments.

3.2 Literature review

There are multiple review articles discussing finite element modelling of tendons and ligaments in different contexts. Benos *et al*. [58] provide an extensive and up-to-date analysis of simulations of anterior cruciate ligament (ACL) reconstructions, outlining the geometry, constitutive models, and number of elements used in each case. Galbusera *et al*. [59] present a comprehensive history of general finite element modelling of the knee ligaments, showing citation charts which clearly map out the most important research in the field. In this literature review, we focus on the shortfalls present in a selection of works spanning the history of finite element modelling, as applied to tendons and ligaments. For a complete summary of the models discussed in this section, see Table 3.1.

One of the earliest examples of the finite element method being applied to study tendons and ligaments (treating them as 3D continua rather than simple springs), was by Pioletti *et al*. [14] in 1998. In this work, the authors modelled the ACL as a transversely isotropic, hyperelastic material attached to two isotropic bone segments. The strain energy function used was from Veronda *et al*. [60] and can be seen in equation (2.38). The bone-ligament-bone system was subjected to boundary conditions mimicking knee flexion. The distribution of the von Mises stress (defined in equation (2.44)) and hydrostatic stress were presented and good correlation was found between the numerical

output and existing experimental data.

A significant number of subsequent attempts to model complex systems involving tendons and ligaments have limitations in their representations of the tissue microstructure. Some authors used an isotropic constitutive law for the tissue [61, 62, 63, 64, 65, 66, 67, 68], despite the fact that tendons are known to be much stiffer in the longitudinal direction than the transverse direction [69]. This simplification could significantly change the stress distribution when complex loading conditions are applied to the tissue, particularly when using a scalar stress measure which combines the components of the stress in each direction.

The implicit assumption that the material strength of soft tissue is independent of direction can be found throughout the literature, due to the widespread adoption of the von Mises stress as an indicator of failure. The von Mises stress has been used by those who use both isotropic [66, 64, 65, 67] and anisotropic models of tendons and ligaments [14, 70, 15, 71, 72, 73, 74]. The consequences of applying isotropic yield criteria to soft tissue has been studied by Korenczuk *et al*. [75], who determined that they are not appropriate for use with anisotropic tissues. This conclusion was reached after comparing the output of a finite element model, which used the von Mises yield criterion to indicate failure, against experimental data. It was found that the von Mises criterion failed to capture the type of failure, the location of failure, and the direction of crack propagation. This important result could impact the conclusions of many of the groups who use the von Mises stress to indicate where a tendon might fail. For example, Sano *et al*. [66] used an isotropic constitutive law to investigate the effects of tear size on stress distribution in a model of the rotator cuff tendon. The authors concluded that stress concentration increases with increasing tear size, and suggested that crescent- and L-shaped tears may propagate in different directions. The first of these points is unlikely to change if a more realistic constitutive model is used. However, if the authors instead assumed that the material strength was anisotropic, they may have reached different conclusions about the direction of tear propagation.

Within the literature, authors often seek to model complex joint structures consisting of multiple bones, tendons, ligaments, and cartilage [76, 61, 74, 77, 78]. As a result of this, it is common to see realistic geometry within these models. Research groups often harness the power of commercial software packages like ABAQUS and ANSYS to produce unstructured meshes based on 3D scans of real tissues. Whilst this approach

clearly increases the realism of the model, it has the potential to introduce errors when the direction of the fibres in the tendons and ligaments is not carefully considered. Many authors choose to simply set the direction of the fibres to be parallel to the longitudinal axis of the tissue [79, 41, 76, 71]. Whilst this is suitable for cylindrical tendons and ligaments, it is unrealistic in more complex geometries, because it implies that fibres stop and start at the surface of the tissue as the cross-sectional area changes. Some authors use the local element geometry to define the fibre direction [74, 78, 77, 8], a concept introduced by Weiss *et al*. [80]. In these examples, the longitudinal axis of the tendon/ligament is no longer a straight line. Because of this, planes transverse to the centre line of the tendon are not parallel to one-another, and the fibre direction is therefore set to be normal to these transverse planes. Whilst this significantly increases the realism of the model, it does not prevent the issue of fibres intersecting the outer boundary of the tissue when the cross-sectional area changes. In order to overcome these shortcomings, we propose a variation to this fibre configuration, where fibres in the centre are aligned with the longitudinal axis, fibres towards the edge of the tendon are aligned with the outer surface, and the direction of fibres in the bulk of the tendon interpolate between these two extremes. In this configuration, fibres are continuous throughout the length of the tendon, an assumption that was discussed in Section 2. A comparison of these fibre orientations along with our proposed variation can be seen in Figure 3.1, and more detail can be found in Section 3.5.3.

Many of the authors who choose a transversely isotropic constitutive law opt to use a phenomenological, or semi-phenomenological (some of the parameters are microstructural and others are not) strain energy function, rather than one derived exclusively from the microstructure. This choice is commonplace both in the finite element modelling literature and in the wider soft tissue mechanics community. Within finite element modelling, commonly used strain energy functions are those introduced by Weiss *et al*. [80], Veronda *et al*. [60], and when the authors assume isotropy, the Mooney-Rivlin strain energy function [46]. Whilst the use of a phenomenological constitutive model may not have much impact on the stress distribution in the tissue, it can limit the applicability of the model because the material parameters are not based on measurable quantities. Using a fully microstructural model can allow the effects of processes such as ageing, injury, and disease to be investigated, provided we know their effects on the microstructure. This approach could be particularly useful in models which seek to find

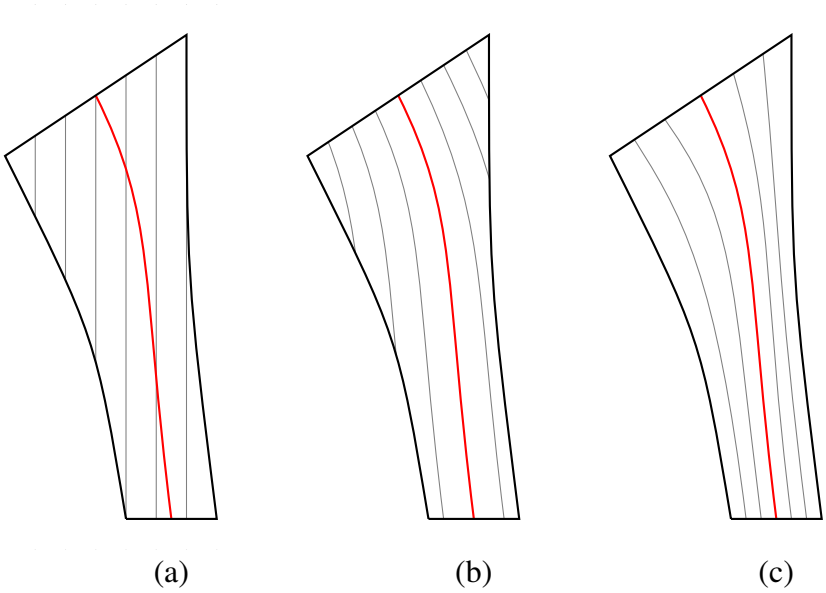

Figure 3.1: Comparison of three fibre orientations within the cross-section of a tendon, with the longitudinal axis shown in red. In (a), fibres are aligned with the z-axis. In (b), the fibres are aligned with the longitudinal axis of the tendon and are parallel within transverse planes. In (c), the fibres follow the contours of the geometry, meaning the direction changes with perpendicular distance from the longitudinal axis. The configuration in (c) is more realistic, because fibres are continuous through the length of the tendon.

the optimal graft tissue for a patient undergoing ligament reconstruction surgery, for example. Suggs *et al*. [7] used finite element modelling to compare the post-operative joint stability for three different types of ACL graft: bone-patellar tendon-bone (BPTB) sections of two different lengths, and non-specified ligament tissue with a similar stiffness to the intact ACL. The difference between the graft materials in this model was just in the length and stiffness. If a more realistic model based on the microstructure was used, it might have been possible to learn more about the internal stress distributions, any potential failure locations, and how these might change over time.

In summary, the literature surrounding finite element modelling of tendons and ligaments is rife with assumptions that require further consideration. As computers have become more powerful, research groups have consistently increased the realism in their models, incorporating complex geometries derived from 3D scans and realistic boundary conditions determined through processes such as gait analysis. Despite these advancements, there are a number of underlying issues which must be addressed. One common simplification is in the choice of constitutive model used to represent the tissue itself. Phenomenological models are often used, reducing the applicability of the model, and in some cases little attention is given to the direction of anisotropy. We therefore set out to quantify the impact that some of these simplifications have when carrying out finite element modelling of tendons and ligaments. We will focus on the effects of geometry and fibre direction on the mechanical properties of tendons, whilst using the microstructural constitutive model first introduced in Section 2.3.2.

Author(s)	Year	Constitutive model	Geometry	Fibre direction	Stress measure
Pioletti *et al.* [14]	1998	Veronda (1970) [60]	ACL	Longitudinal	von Mises stress
Bandak *et al.* [61]	1999	Linear model	Ankle joint	Isotropic	von Mises stress
Song *et al.* [62]	2003	Veronda (1970) [60]	ACL	Isotropic	Cauchy stress
Sano *et al.* [63]	2006	Linear model	Supraspinatus tendon	Isotropic	von Mises stress
Gu *et al.* [64]	2007	Mooney-Rivlin [46]	Achilles tendon	Isotropic	von Mises stress
Gu *et al.* [65]	2008	Mooney-Rivlin [46]	Achilles tendon	Isotropic	von Mises stress
Sano *et al.* [66]	2013	Linear model	Rotator cuff tendons	Isotropic	von Mises stress
Aniţaş *et al.* [67]	2013	Mooney-Rivlin [46]	Achilles tendon	Isotropic	von Mises stress
Firminger *et al.* [68]	2021	Marlow [81]	Patellar tendon	Isotropic	Maximum principal stress
Farha *et al.* [70]	2014	Exponential model	ACL	Not discussed	von Mises stress
Shim *et al.* [15]	2014	Gardiner & Weiss (2003) [77]	Achilles tendon	Longitudinal	von Mises stress
Debski *et al.* [71]	2005	Weiss (1996) [80]	Inferior glenohumeral ligament	Longitudinal	von Mises stress
Hortin *et al.* [72]	2016	Weiss (1996) [80]	Ligaments of the spine	Longitudinal	von Mises stress
Hansen *et al.* [73]	2017	Weiss (1996) [80]	Achilles tendon	Longitudinal	von Mises stress
Penrose *et al.* [74]	2002	Fibre/matrix composite model	Cruciate ligaments	Longitudinal	von Mises stress
Pena *et al.* [76]	2005	Weiss (1996) [80]	Knee joint	Longitudinal	Maximum principal stress
Gardiner *et al.* [77]	2003	Weiss (1996) [80]	Medial collateral ligament (MCL)	Longitudinal	Maximum principal stress
Baldwin *et al.* [78]	2009	2D non-linear hyperelastic	Knee joint	Longitudinal	N/A
Hirokawa *et al.* [79]	2000	Custom dispersed fibre model	ACL	Longitudinal and dispersed	Longitudinal component of Kirchhoff stress
Limbert *et al.* [41]	2003	Custom exponential model	ACL	Longitudinal	Maximum principal stress
Westermann *et al.* [8]	2013	HGO Model [47]	ACL	Longitudinal	von Mises stress
Suggs *et al.* [7]	2002	Non-linear spring model	ACL	N/A	N/A

Table 3.1: A summary of the finite element models discussed in Section 3.2.

3.3 Mathematical background

In this section we will introduce the mathematical background to the finite element method as applied to non-linear solid mechanics problems. Specifically, we will consider the problem of a hyperelastic material subjected to a prescribed displacement on part of its boundary. Throughout Section 3.3, we use a different notation to Section 2.2, instead following the notation of Green and Zerna [38], because the finite element library we will use, oomph-lib, uses this notation throughout its documentation. Unless otherwise stated, throughout this chapter we use lowercase letters to represent undeformed quantities, and uppercase letters to denote their deformed counterparts.

3.3.1 The principle of virtual displacements

Suppose we have an undeformed body Ω that deforms due to a prescribed displacement applied on part of its boundary $\partial\Omega_{\text{prescribed}}$. We consider a set of general curvilinear Lagrangian coordinates ξ^i (in the reference configuration) and denote the position vector to a point in the undeformed body as $\mathbf{r} = \mathbf{r}(\xi^i)$ and the deformed body as $\mathbf{R} = \mathbf{R}(\xi^i)$. We can define a set of undeformed covariant basis vectors by differentiating the position vector $\mathbf{r}$ with respect to the general coordinates ξ^i,

$$\mathbf{g}_i = \frac{\partial \mathbf{r}}{\partial \xi^i}. \tag{3.1}$$

The resulting vectors will be tangent to the coordinate lines in the undeformed configuration. Similarly for the deformed covariant basis vectors we have

$$\mathbf{G}_i = \frac{\partial \mathbf{R}}{\partial \xi^i}. \tag{3.2}$$

The strain in the deformed body can be measured using the Green-Lagrange strain tensor, defined by

$$\gamma_{ij} = \frac{1}{2}(G_{ij} - g_{ij}), \tag{3.3}$$

where $g_{ij} = \mathbf{g}_i \cdot \mathbf{g}_j$ and $G_{ij} = \mathbf{G}_i \cdot \mathbf{G}_j$ are the metric tensors in the undeformed and deformed configurations, respectively. The boundary on which a displacement is prescribed can be parametrised in terms of two coordinates ζ_1 and ζ_2, leading to

$$\xi^i|_{\partial\Omega_{\text{prescribed}}} = \xi^i_{\partial\Omega_{\text{prescribed}}}(\zeta^1, \zeta^2). \tag{3.4}$$

We can use equation (3.4) to write the displaced boundary constraint as a function of ζ_1 and ζ_2,

$$\mathbf{R}(\xi^i_{\partial\Omega_{\text{prescribed}}}(\zeta_1, \zeta_2)) = \mathbf{R}_{\text{prescribed}}(\zeta_1, \zeta_2). \tag{3.5}$$

The principle of virtual displacements states that for a system to be in equilibrium, the work done by any imposed forces is equal to zero for an infinitesimal change in the configuration of the system, provided all kinematic constraints are satisfied [82]. This can be used to relate the stresses and strains in the body, which, in the absence of any body forces, leads to

$$\int_\Omega \tau^{ij} \delta\gamma_{ij} \mathrm{dv} + \delta\Pi_{\text{constraint}} = 0, \tag{3.6}$$

where τ^{ij} is the second Piola-Kirchhoff stress, $\delta\gamma_{ij}$ is the variation of γ_{ij} [83], and the summation convention is used for repeated indices. The volume integral in equation (3.6) is carried out with respect to the undeformed volume, and $\delta\Pi_{\text{constraint}}$ is a Lagrange multiplier term included due to the prescribed displacement on the boundary $\partial\Omega_{\text{prescribed}}$. This Lagrange multiplier term is given by

$$\Pi_{\text{constraint}} = \int_{\partial\Omega} \left(\mathbf{R}(\xi^i(\zeta)) - \mathbf{R}_{\text{prescribed}}(\zeta)\right) \cdot \mathbf{\Lambda} \mathrm{dS}, \tag{3.7}$$

where $\mathbf{\Lambda}$ is a Lagrange multiplier vector for the traction which must be applied to maintain the prescribed displacement, and dS is the deformed area element. We can find the variation $\delta\gamma_{ij}$ using the definition of the Green-Lagrange strain tensor (3.3), along with

the fact that $\delta\mathbf{r} = 0$, since $\mathbf{r}$ is fixed, and τ_{ij} is symmetric. We find that

$$\begin{aligned}\delta\gamma_{ij} &= \frac{1}{2}\delta\left(\frac{\partial\mathbf{R}}{\partial\xi^i}\cdot\frac{\partial\mathbf{R}}{\partial\xi^j} - \frac{\partial\mathbf{r}}{\partial\xi^i}\cdot\frac{\partial\mathbf{r}}{\partial\xi^j}\right)\\ &= \frac{1}{2}\left(\delta\frac{\partial\mathbf{R}}{\partial\xi^i}\cdot\frac{\partial\mathbf{R}}{\partial\xi^j} + \frac{\partial\mathbf{R}}{\partial\xi^i}\cdot\delta\frac{\partial\mathbf{R}}{\partial\xi^j}\right)\\ &= \frac{\partial\mathbf{R}}{\partial\xi^i}\cdot\delta\frac{\partial\mathbf{R}}{\partial\xi^j}.\end{aligned} \tag{3.8}$$

Equation 3.6 can therefore be rewritten in terms of the unknown deformed position vector as

$$\int_\Omega \tau^{ij}\frac{\partial\mathbf{R}}{\partial\xi^i}\cdot\delta\frac{\partial\mathbf{R}}{\partial\xi^j}\mathrm{dv} + \int_{\partial\Omega}\mathbf{\Lambda}\cdot\left(\delta\mathbf{R}(\xi^i(\zeta)) - \delta\mathbf{R}_{\text{prescribed}}(\zeta)\right)\mathrm{dS} = 0. \tag{3.9}$$

The system of equations in (3.9) is now in the correct form to apply the finite element method to find the unknown position vector $\mathbf{R}$.

3.3.2 The finite element method

The finite element method can be used to find an approximate solution for $\mathbf{R}$ in the system of equations in (3.9). At this stage, we can simplify the problem by expressing all position vectors in terms of their Cartesian basis vectors $\mathbf{e}_i$,

$$\mathbf{R}(\xi^j) = R_i(\xi^j)\mathbf{e}_i. \tag{3.10}$$

We can then discretise our continuous body Ω by splitting the undeformed body into a finite set of elements using N nodes. The resulting network of nodes and elements is referred to as a mesh, and is a discrete representation of our continuous body. We write the unknown position vector $\mathbf{R}$ as a finite sum of unknown coefficients X_{ij} multiplied by some basis functions ψ_j. This approximation is written as

$$\mathbf{R}(\xi^k) = \sum_{j=1}^{N} X_{ij}\psi_j(\xi^k)\mathbf{e}_i. \tag{3.11}$$

Similarly, the unknown Lagrange multiplier traction field can be approximated using coefficients L_{ij} as

$$\mathbf{\Lambda}(\xi^k) = \sum_{j=1}^{N} L_{ij}\psi_j(\xi^k)\mathbf{e}_i. \tag{3.12}$$

In the finite element method we choose our basis functions ψ_j so that they have finite support, being non-zero only around node j. For quadratic elements with three nodes, there are three associated shape functions per element,

$$\psi_j^{(1)}(s) = \frac{1}{2}s(s-1), \quad \psi_j^{(2)}(s) = 1-s^2, \quad \psi_j^{(3)}(s) = \frac{1}{2}s(s+1), \tag{3.13}$$

where $s \in [-1,1]$ is a local coordinate defined on each element. At $s=-1$, $x = x_{j-1}$, at $s=0$, $x = x_j$, and at $s=1$, $x = x_{j+1}$. One of the benefits of using the finite element method is that it is simple to interpret the meanings of the unknown coefficients X_{ij}. Since the shape functions equal one at their corresponding nodes and zero elsewhere, the coefficients X_{ij} are simply the value of our unknown function at node x_j (in this case X_{ij} correspond to the components of the deformed position vector $\mathbf{R}$). Inserting equations (3.11) and (3.12) into equation (3.9), and using the fact that the variation of the position vector on the boundary on which a displacement is prescribed is zero, $\delta\mathbf{R}_{\text{prescribed}}(\zeta) = 0$, we arrive at

$$\sum_{m=1}^{N}\left\{\int_\Omega \tau^{ij}\left(\sum_{l=1}^{N} X_{kl}\frac{\partial\psi_l}{\partial\xi^i}\right)\frac{\partial\psi_m}{\partial\xi^j}\mathrm{dv} + \int_{\partial\Omega}\left(\sum_{l=1}^{N} L_{kl}\psi_l\right)\psi_m \mathrm{dS}\right\}\delta X_{km} = 0, \tag{3.14}$$

where, again, the summation convention is used for repeated indices. Since equation (3.14) must be equal to zero for arbitrary variations of X_{km}, the term in the braces must be equal to zero. This results in a set of discrete equations for the unknown values of X_{km} and L_{km},

$$f_{km} = \int_\Omega \tau^{ij}\left(\sum_{l=1}^{N} X_{kl}\frac{\partial\psi_l}{\partial\xi^i}\right)\frac{\partial\psi_m}{\partial\xi^j}\mathrm{dv} + \int_{\partial\Omega}\left(\sum_{l=1}^{N} L_{kl}\psi_l\right)\psi_m \mathrm{dS} = 0. \tag{3.15}$$

To solve this set of equations we must also provide a constitutive relation for the material in question, which will allow us to write τ_{ij} in terms of X_{ij}. We then have a system of equations which can be solved using Newton's method. In doing so, we immediately

see another benefit of using the piecewise linear functions defined in equation (3.13) – the Jacobian matrix with respect to X_{km} is sparse, reducing computation time. Once the unknown coefficients X_{ij} have been found, the deformed position vector $\mathbf{R}$ can be constructed using equation (3.11). When using Newton's method to solve these equations, we will converge quadratically to a solution if a good enough initial guess is provided – meaning that the error in the solution at step $i+1$ is proportional to the square of the error at step i. We typically increment the displacement of the prescribed boundary by some small amount and use the solution at the current step as an initial guess for the next step. The accuracy can be improved by increasing the number of elements in the mesh (referred to as h-refinement), or by increasing the degree of the polynomial basis functions ψ_i (referred to as p-refinement).

3.4 Finite element implementation

3.4.1 Oomph-lib

To solve our system of equations using the finite element method, we will use oomph-lib – an open-source finite element library written in C++ [84]. This library makes use of the object-oriented features of C++ to define high-level objects, such as elements and constitutive laws, which can be overwritten to cater towards a specific problem. Oomph-lib has been used to solve various non-linear solid mechanics problems, and as a result it contains the functionality for modelling isotropic hyperelastic materials. To solve our specific problem, we must therefore extend this functionality to cater for transversely isotropic materials.

Oomph-lib includes an `IsotropicStrainEnergyFunctionConstitutiveLaw` class which contains member functions for computing the stress given a specific isotropic strain energy function. When we write driver code using this constitutive law class, the Piola-Kirchhoff stress is calculated using a function `get_stress()`, which is then fed through a series of internal functions to eventually update the position of the nodes in the mesh. We must therefore overwrite this constitutive law class and redefine the `get_stress()` function to account for the presence of the fibres. We use 3D `QPVDElementsWithContinuousPressure` for the bulk of the tissue. These are quadratic

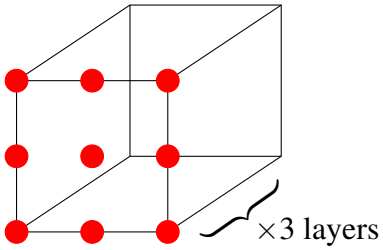

Figure 3.2: Illustration of the nodes in a quadratic 3D element. There are three layers of nine nodes, for a total of 27 nodes.

elements with three nodal points per spatial dimension, for a total of 27 nodes per element, as shown in Figure 3.2. The underlying shape functions used with these elements can be found in the oomph-lib source code [84]. The hydrostatic pressure in the body is enforced through an incompressibility constraint, and its value is stored as data at each of the nodes. For our chosen element type, the pressure is interpolated between the nodes. On the upper surface of the tendon, we use 2D `LagrangeMultiplier` elements. The full 3D mesh comprises these two sets of elements.

3.4.2 The new stress function

In the existing `IsotropicStrainEnergyFunctionConstitutiveLaw` class, the stress measure being computed is the deviatoric part of the second Piola-Kirchhoff stress. In the notation of Green and Zerna [38], this is given by

$$\tau^{ij} = -PG^{ij} + 2W_1 g^{ij} + 2W_2(I_1 g^{ij} - G_{rs} g^{ri} g^{sj}), \tag{3.16}$$

where τ^{ij} is the second Piola-Kirchhoff stress, P is the hydrostatic pressure, and all other terms are as previously defined in Sections 2.2 and 3.3.1. To find the corresponding expression for the transversely isotropic constitutive equation first given in equation (2.36), we start by writing down the definition of the second Piola-Kirchhoff stress for an incompressible material,

$$\boldsymbol{\tau} = \mathbf{F}^{-1}\boldsymbol{\sigma}\mathbf{F}^{-\mathrm{T}}. \tag{3.17}$$

Combining this with (2.36) leads to the expression

$$\boldsymbol{\tau} = -p\mathbf{F}^{-1}\mathbf{F}^{-\mathrm{T}} + 2W_1\mathbf{I} + 2W_2(I_1\mathbf{I} - \mathbf{C}) + 2W_4\mathbf{M}\otimes\mathbf{M} + 2W_5(\mathbf{M}\otimes\mathbf{C}\mathbf{M} + \mathbf{C}\mathbf{M}\otimes\mathbf{M}). \tag{3.18}$$

We must now write the above expression in terms of the deformed and undeformed metric tensors and take the deviatoric part to put it in line with equation (3.16). The definitions of the deformed and undeformed basis vectors, given in equations (3.2) and (3.1) respectively, can be rewritten in terms of Cartesian basis vectors $\mathbf{e}_i$ as

$$\mathbf{g}_r = \frac{\partial x^s}{\partial \xi^r}\mathbf{e}_s, \quad \mathbf{g}^r = \frac{\partial \xi^r}{\partial x^s}\mathbf{e}^s, \quad \mathbf{G}_r = \frac{\partial y^s}{\partial \xi^r}\mathbf{e}_s, \quad \mathbf{G}^r = \frac{\partial \xi^r}{\partial y^s}\mathbf{e}^s. \tag{3.19}$$

The upper index signifies a contravariant vector, ξ^i are general curvilinear coordinates, and x^i and y^i are the undeformed and deformed Cartesian coordinates, respectively. Inverting these expressions gives the following equivalent expressions for the Cartesian basis vectors:

$$\mathbf{e}_r = \mathbf{e}^r = \frac{\partial x^r}{\partial \xi^s}\mathbf{g}^s = \frac{\partial \xi^s}{\partial x^r}\mathbf{g}_s = \frac{\partial y^r}{\partial \xi^s}\mathbf{G}^s = \frac{\partial \xi^s}{\partial y^r}\mathbf{G}_s. \tag{3.20}$$

The deformation gradient tensor is given by

$$\mathbf{F} = \frac{\partial y^i}{\partial x^j}\mathbf{e}_i\otimes\mathbf{e}^j = \frac{\partial y^i}{\partial \xi^r}\frac{\partial \xi^r}{\partial x^j}\mathbf{e}_i\otimes\mathbf{e}^j = \left(\frac{\partial y^i}{\partial \xi^r}\mathbf{e}_i\right)\otimes\left(\frac{\partial \xi^r}{\partial x^j}\mathbf{e}^j\right) = \mathbf{G}_r\otimes\mathbf{g}^r. \tag{3.21}$$

Similar expressions for the inverse and transpose of the deformation gradient can be found:

$$\mathbf{F}^{-1} = \frac{\partial x^i}{\partial y^j}\mathbf{e}_i\otimes\mathbf{e}^j = \mathbf{g}_r\otimes\mathbf{G}^r, \tag{3.22}$$

$$\mathbf{F}^{\mathrm{T}} = \frac{\partial y^j}{\partial x^i}\mathbf{e}_i\otimes\mathbf{e}^j = \mathbf{g}^r\otimes\mathbf{G}_r, \tag{3.23}$$

$$\mathbf{F}^{-\mathrm{T}} = \frac{\partial x^j}{\partial y^i}\mathbf{e}_i\otimes\mathbf{e}^j = \mathbf{G}^r\otimes\mathbf{g}_r. \tag{3.24}$$

The right Cauchy-Green tensor can be found by taking the combination $\mathbf{C} = \mathbf{F}^{\mathrm{T}}\mathbf{F}$, giving

$$\mathbf{C} = \mathbf{F}^{\mathrm{T}}\mathbf{F} = \left(\frac{\partial y^r}{\partial x^i}\mathbf{e}_i\otimes\mathbf{e}^r\right)\cdot\left(\frac{\partial y^j}{\partial x^s}\mathbf{e}_j\otimes\mathbf{e}^s\right) = \frac{\partial y^r}{\partial x^i}\frac{\partial y^j}{\partial x^s}\delta^r_j\mathbf{e}_i\otimes\mathbf{e}^s, \tag{3.25}$$

where we define tensor contraction such that

$$(\mathbf{a}\otimes\mathbf{b})\cdot(\mathbf{c}\otimes\mathbf{d}) = (\mathbf{b}\cdot\mathbf{c})(\mathbf{a}\otimes\mathbf{d}), \tag{3.26}$$

and use $\mathbf{e}^r\cdot\mathbf{e}_j = \delta^r_j$. Expanding out the partial derivatives using the chain rule gives

$$\begin{aligned}\mathbf{C} = \frac{\partial y^r}{\partial\xi^s}\frac{\partial\xi^s}{\partial x^i}\frac{\partial y^r}{\partial\xi^t}\frac{\partial\xi^t}{\partial x^j}\mathbf{e}_i\otimes\mathbf{e}^j &= G_{st}\left(\frac{\partial\xi^s}{\partial x^i}\mathbf{e}_i\right)\otimes\left(\frac{\partial\xi^t}{\partial x^j}\mathbf{e}^j\right)\\ &= G_{st}\mathbf{g}^s\otimes\mathbf{g}^t\\ &= G_{rs}g^{ri}g^{sj}\mathbf{g}_i\otimes\mathbf{g}_j,\end{aligned} \tag{3.27}$$

where we have used

$$G^{rs} = \mathbf{G}^r\cdot\mathbf{G}^s = \frac{\partial\xi^r}{\partial y^j}\frac{\partial\xi^s}{\partial y^j}, \tag{3.28}$$

and the index lowering and switching property of the metric tensor g^{ij}. The square of the right Cauchy-Green tensor is given by

$$\begin{aligned}\mathbf{C}^2 &= \left(G_{rs}g^{ri}g^{sj}\mathbf{g}_i\otimes\mathbf{g}_j\right)\cdot\left(G_{kl}g^{km}g^{ln}\mathbf{g}_m\otimes\mathbf{g}_n\right)\\ &= G_{rs}g^{ri}g^{sj}G_{kl}g^{km}g^{ln}(\mathbf{g}_j\cdot\mathbf{g}_m)(\mathbf{g}_i\otimes\mathbf{g}_n)\\ &= G_{rs}g^{ri}g^{sj}G_{kl}g^{km}g^{ln}g_{jm}\mathbf{g}_i\otimes\mathbf{g}_n\\ &= G_{rs}g^{ri}G_{kl}g^{km}g^{ln}\delta^s_m\mathbf{g}_i\otimes\mathbf{g}_n\\ &= G_{rs}g^{ri}G_{kl}g^{ks}g^{ln}\mathbf{g}_i\otimes\mathbf{g}_n.\end{aligned} \tag{3.29}$$

To find expressions for the terms associated with the anisotropy, we write the alignment vector $\mathbf{M}$ as $\mathbf{M} = M^i\mathbf{g}_i$. This leads to

$$\mathbf{M}\otimes\mathbf{CM} = M^iG_{rs}g^{rj}M^s\mathbf{g}_i\otimes\mathbf{g}_j, \tag{3.30}$$

$$\mathbf{CM}\otimes\mathbf{M} = G_{rs}g^{rj}M^sM^i\mathbf{g}_i\otimes\mathbf{g}_j. \tag{3.31}$$

In order to write out equation (3.18) in terms of the metric tensors, we also need expressions for the strain invariants. These are given by

$$I_1 = \mathrm{Tr}(\mathbf{C}) = g^{ij}G_{ij}, \tag{3.32}$$

$$I_2 = \frac{1}{2}[(\mathrm{Tr}\mathbf{C}^2) - \mathrm{Tr}(\mathbf{C}^2)] = g_{ij}G^{ij}, \tag{3.33}$$

$$I_3 = 1, \tag{3.34}$$

$$I_4 = \mathbf{M}\cdot(\mathbf{CM}) = M^r M^s G_{rs}, \tag{3.35}$$

$$I_5 = \mathbf{M}\cdot(\mathbf{C}^2\mathbf{M}) = M^i M^j g^{rs} G_{ir} G_{sj}. \tag{3.36}$$

Since we are assuming incompressibility, we have $I_3 = 1$. The two new strain invariants, I_4 and I_5, are due to the presence of the fibres. Substituting these expressions into equation (3.18) gives

$$\begin{aligned}\tau^{ij} =& -pG^{ij} + 2W_1 g^{ij} + 2W_2\left(I_1 g^{ij} - G_{rs}g^{ri}g^{sj}\right)\\ &+ 2W_4 M^i M^j + 2W_5\left(M^i G_{rs} g^{rj} M^s + G_{rs} g^{ri} M^s M^j\right),\end{aligned} \tag{3.37}$$

where $\boldsymbol{\tau} = \tau^{ij}\mathbf{g}_i \otimes \mathbf{g}_j$. We define

$$B^{ij} = I_1 g^{ij} - G_{rs}g^{ri}g^{sj}, \tag{3.38}$$

$$M^{ij} = M^i M^j, \tag{3.39}$$

$$C^{ij} = M^i G_{rs} g^{rj} M^s + G_{rs} g^{ri} M^s M^j, \tag{3.40}$$

and

$$\Phi = 2W_1, \quad \Psi = 2W_2, \quad \chi = 2W_4, \quad \Omega = 2W_5, \tag{3.41}$$

leading to the final expression for the second Piola-Kirchhoff stress,

$$\tau^{ij} = -pG^{ij} + \Phi g^{ij} + \Psi B^{ij} + \chi M^{ij} + \Omega C^{ij}. \tag{3.42}$$

It should be noted that B^{ij} and C^{ij} are not the same as the left and right Cauchy-Green deformation tensors introduced in Section 2.2.1. Finally, we must find the deviatoric part of (3.42). To do this we remove the part of the Cauchy stress associated with the mechanical pressure (in terms of $\boldsymbol{\tau}$) and then convert back to find the corresponding

expression for the deviatoric part of the second Piola-Kirchhoff stress. The mechanical pressure is given by

$$\begin{aligned}
P &= \frac{1}{3}\mathrm{Tr}\{\boldsymbol{\sigma}\} = \frac{1}{3}\mathrm{Tr}\{\mathbf{F}\boldsymbol{\tau}\mathbf{F}^{\mathrm{T}}\} \\
&= \frac{1}{3}\mathrm{Tr}\left\{\left(\frac{\partial y^r}{\partial x^s}\mathbf{e}_r\otimes\mathbf{e}^s\right)\cdot(\tau^{ij}\mathbf{g_i}\otimes\mathbf{g}_j)\cdot\left(\frac{\partial y^k}{\partial x^l}\mathbf{e}_l\otimes\mathbf{e}^k\right)\right\} \\
&= \frac{1}{3}\mathrm{Tr}\left\{\left(\frac{\partial y^r}{\partial x^s}\mathbf{i}_r\otimes\mathbf{e}^s\right)\cdot\left(\tau^{ij}\frac{\partial x^m}{\partial\xi^i}\mathbf{e}_m\otimes\frac{\partial x^n}{\partial\xi^j}\mathbf{e}_n\right)\cdot\left(\frac{\partial y^k}{\partial x^l}\mathbf{e}_l\otimes\mathbf{e}^k\right)\right\} \\
&= \frac{1}{3}\mathrm{Tr}\left\{\frac{\partial y^r}{\partial x^s}\tau^{ij}\frac{\partial x^m}{\partial\xi^i}\frac{\partial x^n}{\partial\xi^j}\frac{\partial y^k}{\partial x^l}\delta^s_m\delta_{nl}\mathbf{e}_r\otimes\mathbf{e}^k\right\} \\
&= \frac{1}{3}\mathrm{Tr}\left\{\frac{\partial y^r}{\partial x^m}\tau^{ij}\frac{\partial x^m}{\partial\xi^i}\frac{\partial x^l}{\partial\xi^j}\frac{\partial y^k}{\partial x^l}\mathbf{e}_r\otimes\mathbf{e}^k\right\} \\
&= \frac{1}{3}\mathrm{Tr}\left\{\frac{\partial y^r}{\partial\xi^i}\frac{\partial y^k}{\partial\xi^j}\tau^{ij}\mathbf{e}_r\otimes\mathbf{e}^k\right\} = \frac{1}{3}\frac{\partial y^r}{\partial\xi^i}\frac{\partial y^k}{\partial\xi^j}\tau^{ij}\delta^k_r = \frac{1}{3}\tau^{ij}G_{ij}.
\end{aligned} \tag{3.43}$$

Substituting in the expression for τ^{ij} given in (3.42), we find

$$P = \frac{1}{3}\big(-3p + I_1\Phi + 2I_2\Psi + I_4\chi + 2I_5\Omega\big). \tag{3.44}$$

The deviatoric part of the 2nd Piola-Kirchhoff stress is therefore given by

$$\overline{\boldsymbol{\tau}} = \mathbf{F}^{-1}(\boldsymbol{\sigma} - P\mathbf{I})\mathbf{F}^{-\mathrm{T}} = \boldsymbol{\tau} - P\mathbf{F}^{-1}\mathbf{F}^{-\mathrm{T}}, \tag{3.45}$$

leading to

$$\overline{\tau}^{ij} = \tau^{ij} - PG_{ij} = \Phi g^{ij} + \Psi B^{ij} + \chi M^{ij} + \Omega C^{ij} - KG^{ij}, \tag{3.46}$$

where

$$K = \frac{1}{3}\big(I_1\Phi + 2I_2\Psi + I_4\chi + 2I_5\Omega\big). \tag{3.47}$$

We can now implement equation (3.46) in the new `get_stress()` function, allowing us to model transversely isotropic hyperelastic materials.

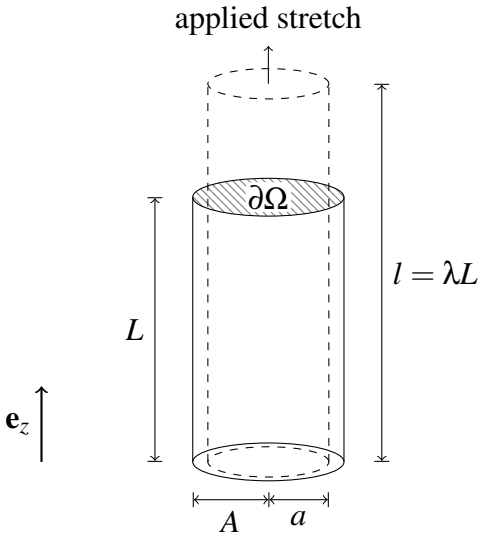

Figure 3.3: Outline of the cylinder extension problem used as a base case for investigating the effects of tendon geometry on mechanical behaviour.

3.5 Problem outline

To assess the effect that geometry has on the mechanical properties of tendons, we will first consider the base case of a right circular cylinder. We will then make small changes to this geometry and see how the mechanical properties differ from the base case. Throughout Section 3.5, we use the same notation as in Section 2.2, but continue using capital letters for quantities in the initial configuration, and lowercase letters for quantities in the deformed configuration.

3.5.1 Base case

Consider a circular cylinder composed of an incompressible, transversely isotropic, hyperelastic material with fibres aligned parallel to the z-axis and strain energy function given by $W = W(I_1, I_4)$. The cylinder has initial length L and radius A. A displacement field $\boldsymbol{u}(\mathbf{X})$ is applied to the upper surface of the cylinder such that $u_z(R, \Theta, Z = L) = l = \lambda L$ and $u_r(R = A, \Theta, Z = L) = a$. The bottom surface of the cylinder is fixed in the z-direction and the curved surface is assumed to be traction-free. A diagram outlining this problem can be seen in Figure 3.3.

Due to incompressibility, stretching the cylinder by a factor of λ will cause the radius

to contract uniformly by a factor of $1/\sqrt{\lambda}$. In cylindrical polar coordinates, this leads to the deformation field

$$r(R,\Theta,Z) = \frac{R}{\sqrt{\lambda}}, \quad \theta(R,\Theta,Z) = \Theta, \quad z(R,\Theta,Z) = \lambda Z. \tag{3.48}$$

From this we can compute a number of useful quantities defined in Section 2.2.1. The deformation gradient tensor is given by

$$\mathbf{F} = \begin{pmatrix} \frac{\partial r}{\partial R} & \frac{1}{R}\frac{\partial r}{\partial \Theta} & \frac{\partial r}{\partial Z} \\ r\frac{\partial \theta}{\partial R} & \frac{r}{R}\frac{\partial \theta}{\partial \Theta} & r\frac{\partial \theta}{\partial Z} \\ \frac{\partial z}{\partial R} & \frac{1}{R}\frac{\partial z}{\partial \Theta} & \frac{\partial z}{\partial Z} \end{pmatrix} = \begin{pmatrix} \frac{1}{\sqrt{\lambda}} & 0 & 0 \\ 0 & \frac{1}{\sqrt{\lambda}} & 0 \\ 0 & 0 & \lambda \end{pmatrix}. \tag{3.49}$$

The fibres are aligned with the z-axis so that $\mathbf{M} = (0,0,1)^{\mathrm{T}}$, leading to the following strain invariants:

$$I_1 = \frac{2}{\lambda} + \lambda^2, \qquad I_2 = \frac{1}{\lambda^2} + 2\lambda, \qquad I_3 = 1, \qquad I_4 = \lambda^2, \qquad I_5 = \lambda^4. \tag{3.50}$$

In this section we will focus on two constitutive models: the semi-phenomenological HGO model [47], and a microstructural model which incorporates distributions of fibril length, as defined in Section 2.3.2. Both strain energy functions derived from these models only depend on I_1 and I_4, allowing us to write down a simplified expression for the Cauchy stress based on equation (2.36),

$$\boldsymbol{\sigma} = -p\mathbf{I} + 2W_1\mathbf{B} + 2W_4\mathbf{m}\otimes\mathbf{m}, \tag{3.51}$$

where $\mathbf{m} = \mathbf{FM}$ and $\mathbf{B} = \mathbf{FF}^{\mathrm{T}}$. Since we assume that there are no body forces and that gravity is negligible, the momentum equation given in equation (2.11) reduces to the equilibrium equation,

$$\boldsymbol{\nabla}\cdot\boldsymbol{\sigma} = \mathbf{0}. \tag{3.52}$$

The traction-free boundary conditions on the curved surface of the cylinder can be written as

$$\boldsymbol{\sigma}\cdot\mathbf{n} = \mathbf{0}, \tag{3.53}$$

at $r = a$, where a is the radius of the cylinder in the deformed configuration, and $\mathbf{n}$ is the outer unit normal to the curved surface. By solving this system of equations for σ, we

find that the there is only one non-zero component of the Cauchy stress: σ_{zz}. Written in terms of the derivatives of the strain energy function W, we have

$$\sigma_{zz} = -p + 2W_1\lambda^2 + 2W_4\lambda^2, \tag{3.54}$$

where $p = 2W_1/\lambda$ is the hydrostatic pressure required to maintain incompressibility, found using the traction-free boundary condition. Using the HGO model, we find that

$$\sigma_{zz}^{\mathrm{HGO}}(\lambda) = \mu\left(\lambda^2 - \frac{1}{\lambda}\right) + 2k_1(\lambda^2-1)\lambda^2 e^{k_2(\lambda^2-1)^2}, \tag{3.55}$$

where μ, k_1, and k_2 are constants. The corresponding expression for the crimped fibril model is

$$\sigma_{zz}^{\mathrm{crimp}}(\lambda) = \mu(1-\phi)\left(\lambda^2 - \frac{1}{\lambda}\right) + E(A + B\lambda + C\lambda^2 + D\lambda\log\lambda), \tag{3.56}$$

where ϕ is the collagen volume fraction, E is the fibril Young's modulus, and A, B, C, and D are piecewise constant functions of λ defined in Section 2.3.2.

3.5.2 Macroscale geometry

Tendons and ligaments are typically described as long, flat bands of connective soft tissue, but their shape can vary significantly. Some, such as the flexor digitorum profundus, are close to cylindrical [85], but others, such as the Achilles tendon, have a flattened cross-section that can vary in size down its length. Instead of using specific, individual geometries taken from 3D scans of tendons, we use an idealised geometry in order to explore how certain generic geometric features may affect the mechanical response of the tissue. To produce an idealised geometry, we start with an elliptic cylinder with semi-major axis A and semi-minor axis sA, where $s \in (0,1]$, and apply a transformation to every point in the cylinder. We start with the Cartesian position of a point in the cylinder $(\overline{X},\overline{Y},\overline{Z})$ and convert to cylindrical polar coordinates (R,Θ,Z). We then apply our transformation and convert back to Cartesian coordinates, leading to

$$X = R\cos\Theta\cdot f(\overline{Z}), \qquad Y = R\sin\Theta\cdot f(\overline{Z}), \qquad Z = \overline{Z}, \tag{3.57}$$

where (X,Y,Z) is the transformed position and $f(\overline{Z})$ is a function that specifies how the radius of the tendon or ligament changes along its length. The transformation in equation (3.57) changes both the width and the thickness of the tendon. To maintain a constant thickness, we can simply set $Y = \overline{Y}$. We choose f to be the product of a linear function and a sine function with period equal to twice the length of the tendon,

$$f(\overline{Z}) = \left[(1-t_1)\frac{\overline{Z}}{L} + t_1\right] \cdot \left[1-(1-t_2)\sin\left(\frac{\pi\overline{Z}}{L}\right)\right], \tag{3.58}$$

where $t_1 \in (0,1]$ is the ratio between the upper and lower diameters of the tendon, and $t_2 \in (0,1]$ is the ratio between the upper and middle diameters of the tendon in the absence of linear taper, and L is the length of the tendon, as defined in Section 3.5.1. This form of f allows for a linearly tapered tendon, an hourglass shaped tendon, and combinations thereof. After the mesh transformation has been applied, the ratio between the central and upper radii of the tendon is $t_2(1+t_1)/2$.

To test the effects that a certain combination of parameters (s,t_1,t_2) has on the mechanical properties of the tendon/ligament, we must first match its volume to that of a reference circular cylinder of radius A_0 and length L. This ensures that when we use a new set of parameters, we are not adding or removing material – we only want to study the effects of redistributing the existing material into a new shape. Since we have used an analytic expression to transform the shape of the cylinder, we can compute the exact volume of our geometry using the expression

$$V = \int_0^L \int_0^{2\pi} \int_0^A \left|\frac{\partial(X,Y,Z)}{\partial(R,\Theta,Z)}\right| \mathrm{d}R\mathrm{d}\Theta\mathrm{d}Z. \tag{3.59}$$

For the transformation in equation (3.57), this volume is given by

$$\begin{aligned} V = \frac{sA^2L}{12\pi^2}\Big(& -96(t_1-1)^2(t_2-1) + 24\pi^2(1+t_1^2)(t_2-1) \\ & -3\pi(t_1-1)^2(t_2-1)^2 + 2\pi^3(1+t_1+t_1^2)(3-2t_2+t_2^2)\Big), \end{aligned} \tag{3.60}$$

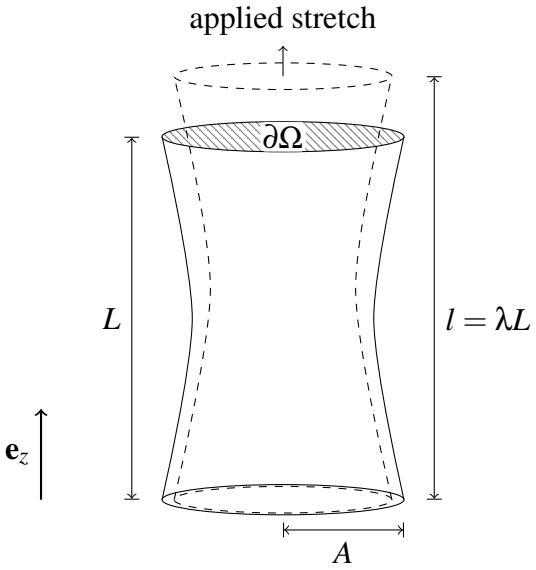

Figure 3.4: Outline of the transformed cylinder problem.

and for a transformed cylinder of constant width we have

$$V = \frac{sA^2L}{2}(1+t_1)(\pi+2t_2-2). \tag{3.61}$$

Once a transformation has been chosen, we can select A to ensure that $V = \pi A_0^2 L$. When applying this process to our finite element model, we start with a cylindrical mesh of nodes, apply the transformation outlined above, then set those nodal positions to be the initial configuration of the tendon. We can then apply the same boundary conditions as in the cylindrical base case, which are described in Section 3.5.4. This new problem is outlined in Figure 3.4.

3.5.3 Fibre direction

Many groups who have attempted to model tendons using finite element modelling fail to specify the direction of the fibres. This is not an issue when the tendon is cylindrical because it can be assumed that the fibres are aligned with the longitudinal axis of the tendon. However, when a realistic geometry is used, it is often not clear if the fibres in these models follow the contours of the geometry or are simply aligned with the

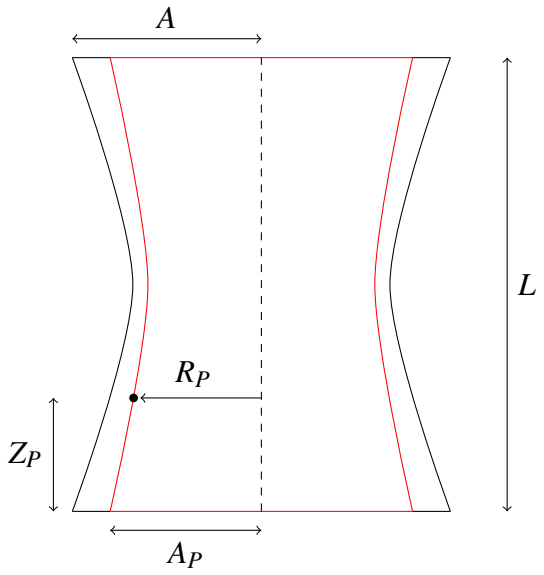

Figure 3.5: The outline of a tapered, elliptic cylinder containing the point P. To find the collagen fibre direction vector at this point we imagine the point is on the surface of a smaller tapered cylinder, shown here in red.

longitudinal axis of the tendon. This could have an impact on the mechanical response of a tendon if fibres are stopping and starting as the surface undulates. There is strong evidence that fibres are continuous throughout the length of the tendon (as discussed in Section 2.1.2), suggesting that the fibre direction field should follow the contours of the geometry. A further aim of our modelling work is to explore the effects that the fibre orientation has on the mechanical properties of the tendon, in order to determine if this should be given more attention when applied to more complex geometries. We can explore this question using the idealised geometry previously described.

For a tendon of upper semi-major axis A, with shape defined by equations (3.57) and (3.58), we can derive the fibre direction at a point $P : (X_P, Y_P, Z_P)$ by considering a similar tendon with a smaller semi-major axis A_P, centred at $Z = 0$, on the surface of which P lies (as shown in Figure 3.5). Since the cross section of our tendon is elliptical, we can use the polar equation of an ellipse to write down an expression for A_P,

$$A_P = \frac{R_P}{f(Z_P)\sqrt{\cos^2\Theta_P + s^2\sin^2\Theta_P}}, \tag{3.62}$$

where (R_P, Θ_P, Z_P) are the coordinates of our point in cylindrical polar coordinates. We can now use $0 \leq u \leq 2\pi$ and $0 \leq v \leq L$ to parametrise a point $\mathbf{P}$ on the surface of our smaller tendon,

$$\mathbf{P}(u,v) = X(u,v)\mathbf{e}_x + Y(u,v)\mathbf{e}_y + Z(u,v)\mathbf{e}_z, \tag{3.63}$$

where

$$X(u,v) = A_P \cos u \cdot f(v), \tag{3.64}$$

$$Y(u,v) = sA_P \sin u \cdot f(v), \tag{3.65}$$

$$Z(u,v) = v. \tag{3.66}$$

We assume that the fibres do not twist about the longitudinal axis of the tendon, although it has been shown that they can form helical wave patterns within the ACL and the patellar tendon [86]. For the fibres to not twist around the tendon, we want the fibre direction field to be parallel to $\frac{\partial \mathbf{P}}{\partial v}$. We therefore have that the fibre direction at a point (X_P, Y_P, Z_P) is equal to $M_x\mathbf{e}_x + M_y\mathbf{e}_y + M_z\mathbf{e}_z$, where

$$M_x = A_P \cos u f'(v) \tag{3.67}$$

$$M_y = sA_P \sin u f'(v) \tag{3.68}$$

$$M_z = 1, \tag{3.69}$$

where u is the angle between the vector (X_P, Y_P) and the half-plane $Y_P = 0$ for $X_P > 0$, and $v = Z_P$. If we choose to give the tendon a constant semi-minor axis (in the y-direction), we set $M_y = 0$. Figure 3.6 shows an example of this direction field. We refer to fibres that follow the contours of the tendon geometry as contour-aligned or c-aligned. The method outlined above is appropriate for finding the direction field of c-aligned fibres in an idealised geometry defined by known mathematical expressions. For more realistic geometries based on 3D scans of real tendons and ligaments, a different method would need to be used. For example, the fibre direction at a node could be found by considering the slope of the face of the element on which it lies.

Despite the fibres in this example no longer being parallel to one another, we can still describe the material as transversely isotropic because at each point there is one plane of symmetry defined by the vector $\mathbf{M}$. We can therefore use the simplified transversely

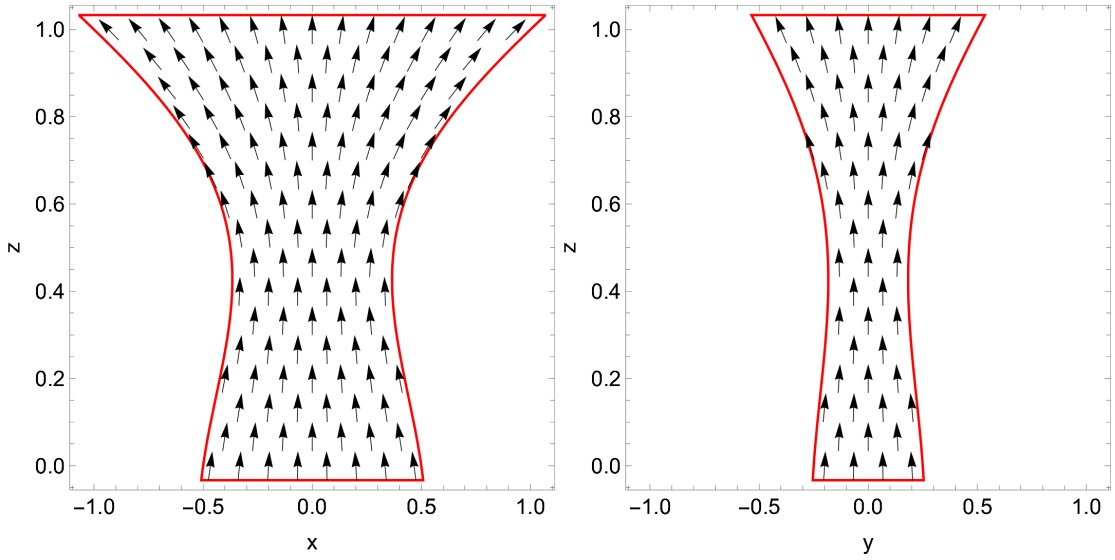

Figure 3.6: The fibre direction field defined in equation (3.67) shown from two angles. Subfigure (a) shows the plane $y = 0$, whilst (b) shows the plane $x = 0$. In this example we have $s = t_1 = t_2 = 0.5$ and $A = L = 1$.

isotropic version of the Hill yield criterion (equation (2.45)) if we wish to study failure in our tendon/ligament, provided we apply a suitable transformation to the Cauchy stress. We choose the transformation which aligns the zz-component of the Cauchy stress with the deformed fibre direction $\mathbf{m} = \mathbf{FM}$, as shown in Figure 3.7. To find the rotation matrix $\mathbf{R}$ required to rotate $\mathbf{e}_z$ to be in line with $\mathbf{m}$, we can use Rodrigues' rotation formula [87],

$$\mathbf{R} = \mathbf{I} + \sin\theta\mathbf{K} + (1 - \cos^2\theta)\mathbf{K}^2, \tag{3.70}$$

where $\mathbf{I}$ is the 3×3 identity matrix, θ is the angle between $\mathbf{e}_z$ and $\mathbf{m}$, and $\mathbf{K}$ is the skew-symmetric matrix satisfying

$$\mathbf{K}\mathbf{e}_z = \mathbf{e}_z \times \mathbf{m}. \tag{3.71}$$

The transformed Cauchy stress tensor σ' can then be found using

$$\sigma' = \mathbf{R}\sigma\mathbf{R}^{\mathrm{T}}. \tag{3.72}$$

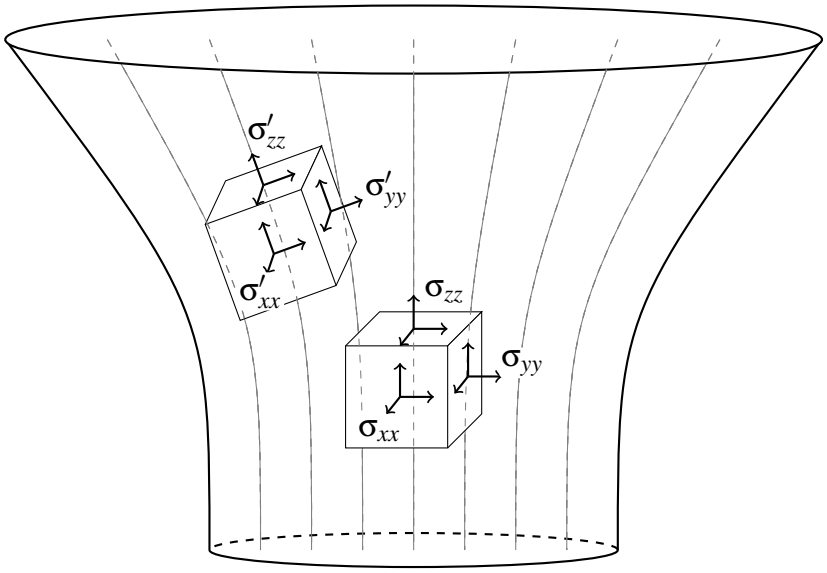

Figure 3.7: Three components of the Cauchy stress $\boldsymbol{\sigma}$, and the transformed stress tensor $\boldsymbol{\sigma}'$ which has been rotated to align with the fibre direction.

3.5.4 Application of boundary conditions

To apply the deformation described in Section 3.5.1, we firstly pin all the nodes on the bottom face of the tendon in the z-direction. Additionally, we pin any nodes on this surface that lie on the x-axis in the y-direction and vice versa. This pinning process ensures that the tendon does not undergo any rigid-body rotations or translations, whilst allowing the tissue to contract in the transverse plane. On the upper face of the tendon, we use Lagrange multiplier elements to prescribe a certain displacement, which gets incremented gradually. We must also prescribe the in-plane deformation, for which we use the expression for a right circular cylinder given in equation (3.48). In reality, tendons would also experience torsion, bending, and shearing forces which could all contribute significantly to the internal stress field, and our choice to ignore these forces means that our model does not accurately represent a tendon/ligament *in vivo*. Whilst our boundary conditions do not exactly recreate the conditions that a real tendon or ligament would be subjected to inside the body, they are still similar to the conditions experienced by a tendon when it is subjected to tensile testing *ex vivo*. Our choice to impose a radial contraction on the upper surface of the tendon is unrealistic for these

types of tensile tests, as the tissue would need to be placed in some sort of grip in order to be stretched. Our model can therefore only provide a good approximation to tensile tests carried out on tendons *ex vivo*, in the bulk of the tendon, away from the attachment sites.

3.5.5 Post-processing

Alongside the distributions of stress within the tissue, we should consider the macroscale stress-strain curve generated over the course of the deformation, to ensure that our results can be compared with experimental data. To do this, we must consider the traction applied to the upper surface of the tendon through the Lagrange multiplier elements. We can find the force applied by integrating the traction over this surface, and convert to engineering stress by dividing the force by the initial area of this surface. The i-th component of the resultant force acting on the upper surface of the tendon is given by

$$F_i = \int_{\partial\Omega} \Lambda_i \mathrm{dS}, \tag{3.73}$$

where Λ_i is the traction acting at the surface, first introduced in equation (3.7). To find the engineering stress, we average the $z-$component of this force over the initial area of the surface over which it is applied,

$$\sigma_e = \frac{F_z}{\pi s A^2}. \tag{3.74}$$

3.6 Results for idealised geometries

In this section, we first perform a convergence study to determine the resolution required for our finite element model. We then move on to extract data using idealised geometries and generic parameter values. We look at the distribution of stress within the tendon and the maximum value of stress in the direction of the fibres for different values of t_1, t_2, and s, along with the different fibre directions discussed in Section 3.5.3. This allows us to predict the effects of different geometric features on the macroscale mechanical properties of the tissue.

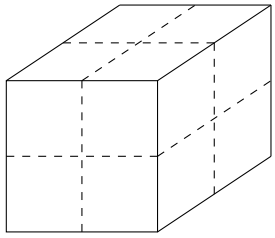

Figure 3.8: Illustration of the uniform refinement procedure applied to a single element. The solid line shows the unrefined element, which gets split up into 8 new elements during refinement.

3.6.1 Convergence testing

When using the finite element method to solve a problem, the accuracy of the solution will depend on the resolution of the mesh. Using too few elements will result in the expression in equation (3.11) being truncated too early, potentially missing important terms and reducing the overall accuracy of the solution. As we increase the resolution of the mesh, the solution will eventually become independent of the number of elements, suggesting that we are converging to a solution. We must therefore perform a resolution study to find the optimal number of elements required to provide an accurate solution without wasting computation time.

The simplest way to refine a mesh within oomph-lib is to use the function `refine_uniformly()`. This function adds an extra node to the edge between existing nodes, splitting a single 3D element into eight new elements, as shown in Figure 3.8. We can also change the number of vertical layers in the underlying mesh by setting a parameter `nlayer`. This provides us with two methods of controlling the number of elements, and we will consider the combinations presented in Table 3.2 for both the base case and for a non-cylindrical tendon. For the base case we can compare our finite element solution to the analytic solution, whereas for the non-cylindrical tendon we must check that the solution converges to some value.

For our resolution study we use the HGO model with material parameters $C = 1$MPa, $k_1 = 10$MPa, and $k_2 = 10$. These parameter values were chosen so that the final engineering stress values would be roughly in-line with those observed experimentally. During our initial implementation, we found that having a realistic ratio ($\sim 1,000,000$ [42]) between the stiffness of the matrix and the fibres would lead to the Newton solver

# uniform refinements	# layers	# elements
0	5	25
0	10	50
0	20	100
1	5	200
1	10	400
1	20	800
2	5	1600
2	10	3200

Table 3.2: The number of elements used during the resolution study and the parameter values used to obtain the stated resolution.

diverging, prompting us to use a lower ratio in all subsequent tests. We also found that stress concentrations would arise more frequently when the HGO model was used (this is discussed more in Section 3.6.3). As a result of this, we only used the HGO model in our convergence study, assuming that we would converge to a solution in the same geometry when using the crimped fibril model. Plots of the engineering stress against stretch can be seen in Figure 3.9 for the cylindrical base case, and Figure 3.10 for the transformed geometry. For the cylindrical geometry, we increased the stretch in increments of 0.01 until reaching $\lambda = 1.2$. For non-cylindrical geometries, we only stretched up to a final value of $\lambda = 1.1$ because a smaller step size was necessary.

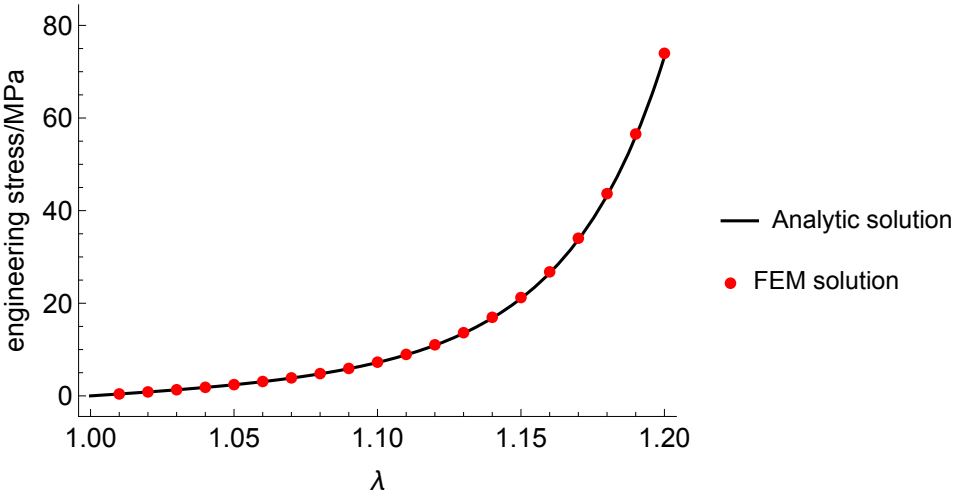

Figure 3.9: Comparison of the analytic and finite element solution for a transversely isotropic cylinder. We use the HGO model in both cases with $C = 1$MPa, $k_1 = 10$MPa, and $k_2 = 10$. The finite element solution uses 25 elements, the lowest number in our resolution study.

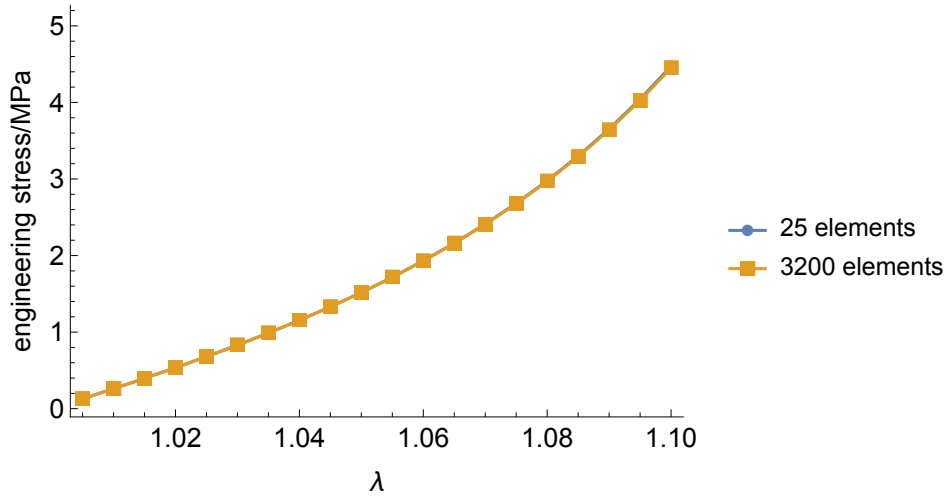

Figure 3.10: Comparison of the least and most refined solutions for a tendon with idealised geometry stretched by a factor of $\lambda = 1.1$. The geometric parameters used were $s = 0.5$, $t_1 = t_2 = 0.8$. Both curves lie on top of one another.

From Figures 3.9 and 3.10, it appears as though the engineering stress is unaffected by the number of elements in both geometries. For the cylindrical mesh we can obtain

a very accurate solution using a low number of elements because the deformation is homogeneous. For the non-cylindrical mesh we find that the engineering stress alone is not enough to determine convergence, since it averages out any discrepancies between the solutions. If we observe the solution at individual points within the mesh, we find that there is indeed a difference between the different levels of refinement. Shown in Figure 3.11 is the final position of two points in the initial configuration: $p_1(0.085, 0.0, 0.8)$ and $p_2(0.050, 0.026, 0.4)$ (shown in Figure 3.12), as a function of the number of elements in the mesh. These points were chosen by selecting one random point in the bulk of the tendon, and one random point on the surface of the tendon and finding the nodes closest to those points. Figures 3.11 (a) and (c)–(f) all show a jump in the solution when the number of elements increases from 100 to 200. To produce a mesh with 200 elements, we refine the mesh uniformly rather than by increasing the number of vertical layers. As a result of the new in-plane refinement, the shape of the cross-section changes and the final solution differs. We find that any mesh with over 200 elements, corresponding to one uniform refinement, is a high enough resolution to produce a mesh-converged solution. Since we can refine a second time whilst maintaining a moderate computation time, we choose to use a mesh containing 1600 elements in future tests, allowing for some degree of computational overhead.

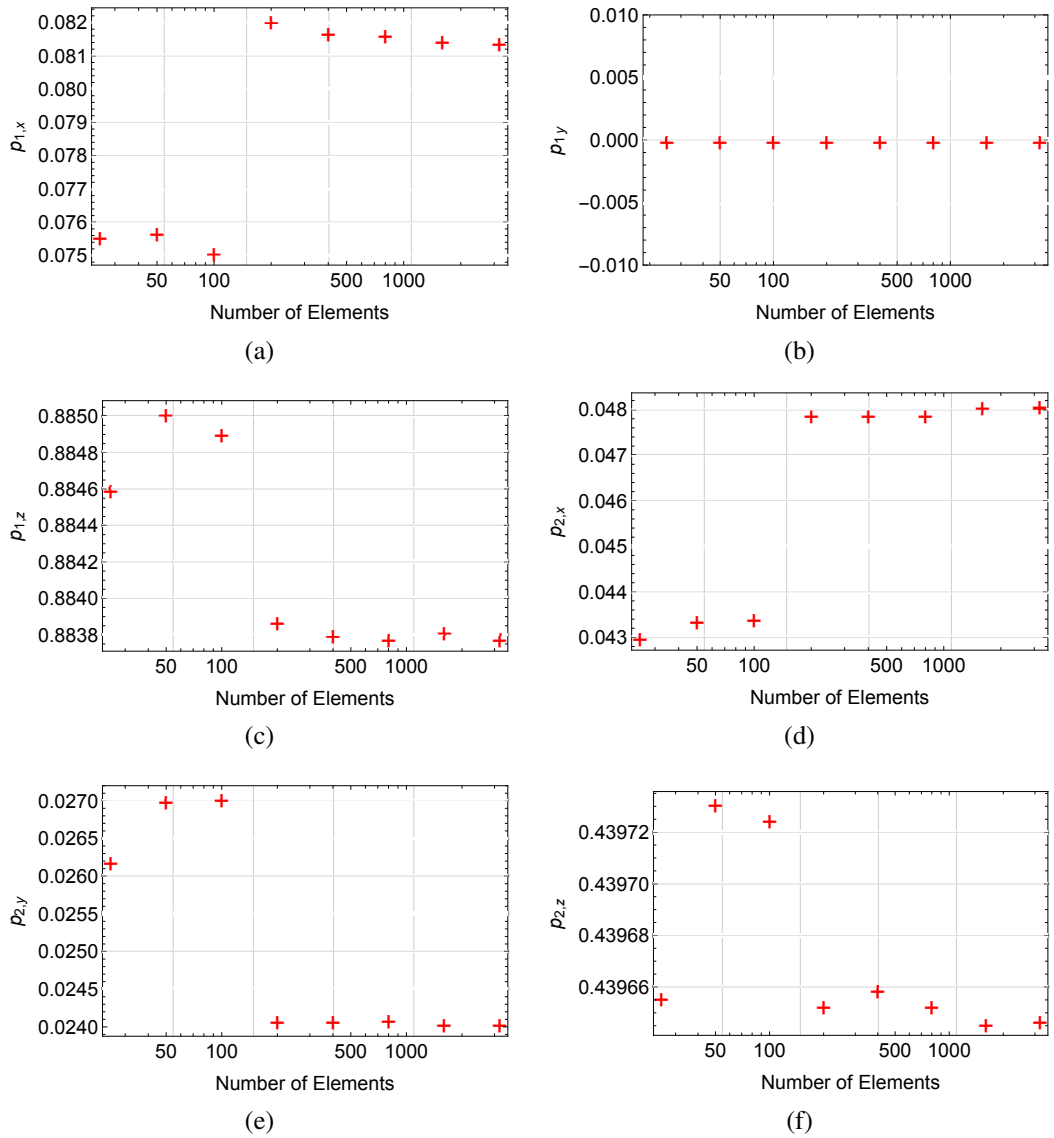

Figure 3.11: The x-, y-, and z-components of two points p_1 and p_2 in the final deformed configuration as a function of the number of elements in the mesh.

3.6.2 Ellipticity

To study the effects of ellipticity on the macroscale mechanical behaviour of tendons and ligaments, we vary the ellipticity parameter s between $s = 1.0$ and $s = 0.5$, holding all other geometric and material properties constant. We set the volume of each test

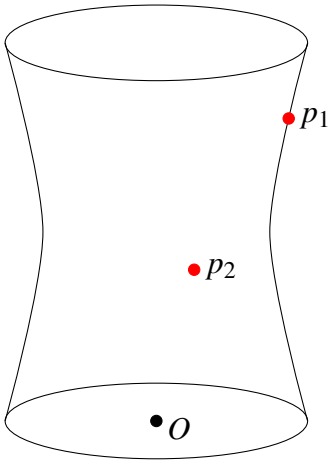

Figure 3.12: The position of p_1 and p_2 within the tendon. The origin is denoted by O.

to be equal to that of a reference circular cylinder of radius $A = 0.1$ and length $L = 1$. When using the HGO model, we use $\mu = 1$MPa, $k_1 = 10$MPa, and $k_2 = 10$, and for the crimped fibril model we use $\mu = 1$MPa, $E = 10$MPa, $\phi = 0.8$, $a = 1.0$, $b = 1.05$, and $c = 1.025$. The parameter values used for the crimped fibril model are in-line with those observed experimentally, whilst maintaining a similar fibre to matrix stiffness ratio as in the tests that used the HGO model. For both models, we find that decreasing s does not affect the stress-strain curves or the internal stress distributions, because the prescribed displacement on the upper surface of the tendon yields a homogeneous stress field with one non-zero value of stress σ_{zz}. The stress-strain curves obtained in these tests are identical to the analytic expression for the base case of a right-circular cylinder, because the internal deformation field is identical. Figure 3.13 shows the engineering stress-strain curves obtained through finite element modelling for the two different constitutive models being considered in this section.

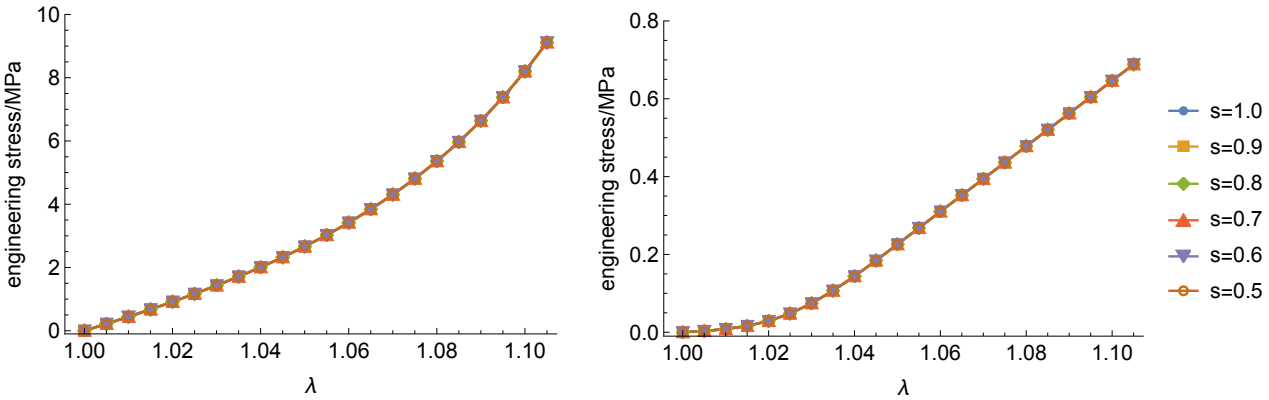

Figure 3.13: Engineering stress against stretch for elliptic tendons of equal volume. The HGO model is used in (a), whilst the crimped fibril model is used for (b). All curves lie on top of one another.

3.6.3 Linear taper

Yoo *et al.* found that the width of the patellar tendon decreases from 30.3mm at the proximal part, to 24.0mm at the distal part [88], tapering linearly from one end to the other. We now investigate the effects of such a linear taper on the mechanical properties of the tendon/ligament, by varying the geometric parameter t_1. We choose to vary t_1 between $t_1 = 1.0$ and $t_1 = 0.5$, with all other parameters (including t_2 and s) held constant. Whilst this lower limit is below the value observed by Yoo *et al.* ($t_1 = 0.79$), it will allow us to explore an extreme limit. We start by aligning the fibres with the z-axis, before changing the fibre direction to follow the contours of the geometry. The engineering stress-strain curve obtained using these parameters with the HGO model and z-aligned fibres can be seen in Figure 3.14. As t_1 decreases, the bottom area of the tendon also decreases, meaning that to keep a constant volume, the top area must increase. Because the resultant force acting on the top surface is being spread over a larger area, the engineering stress decreases. For $t_1 = 0.6$ and $t_1 = 0.5$, we found that the Newton solver did not converge to a solution for the chosen parameter values. By looking at the maximum value of σ_{zz} in the tendon, as shown in Figure 3.14, we can see that the stress begins to increase sharply at a certain value of stretch. The heat plot in Figure 3.16 shows the distribution of σ_{zz} within a cross-section of the tendon with $t_1 = 0.5$ at a stretch value

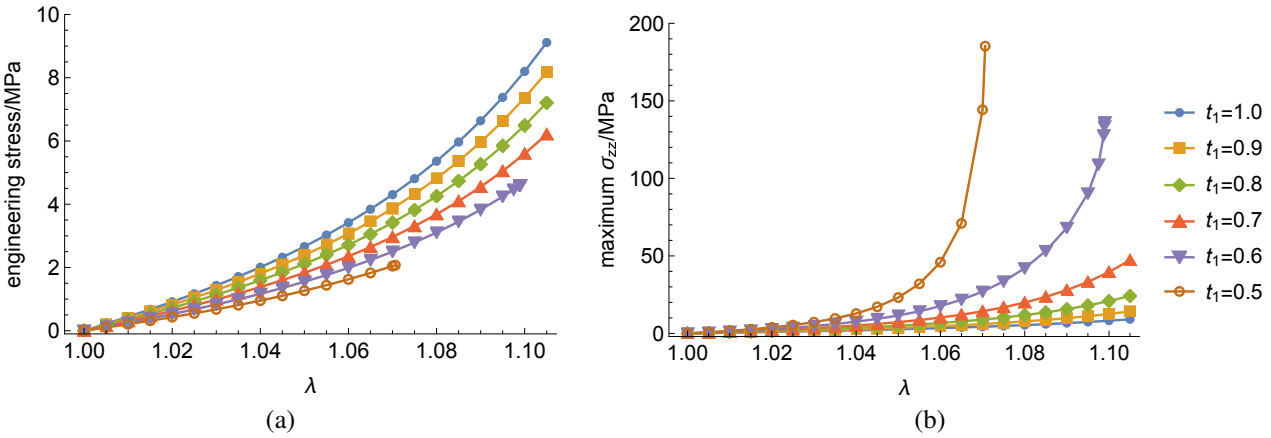

Figure 3.14: Engineering stress (a) and maximum σ_{zz} (b) against stretch for linearly tapered tendons with z-aligned fibres using the HGO model. The maximum value of σ_{zz} is located at the edge of the smallest cross-section, as shown in Figure 3.16.

of $\lambda = 1.065$. In this figure we can clearly see a large stress concentration building up around the bottom edge of the tendon, where there is no solution for large λ.

When we align the fibres to follow the contours of the geometry, we see a similar general trend, as shown in Figure 3.15. As t_1 decreases, the engineering stress at a given strain will decrease, and the maximum value of σ_{zz} will increase because the smallest cross-section is decreasing in size. However, with this fibre orientation we do not see the same stress concentrations forming around the lower edge of the tendon, as can be seen in Figure 3.16. We instead see that the magnitude of σ_{zz} increases smoothly as the radius of the tendon decreases, reaching a maximum on the bottom surface. For $t_1 = 0.5$ and $\lambda = 1.065$, we found that changing from z- to c-aligned fibres reduces the maximum value of σ_{zz} by 94%.

When using the crimped fibril model, we see the same general trends emerge. The engineering stress and maximum value of σ_{zz} for linearly tapered tendons using this model can be seen in Figures 3.17 and 3.18. To generate these figures we used $\mu =$ 1.0MPa, $E = 10$MPa, $\phi = 0.8$, $a = 1.0$, $b = 1.05$, and $c = 1.025$. In Figure 3.17 the fibres are aligned with the z-axis, whilst in Figure 3.18 they follow the contours of the geometry. In the most extreme case ($t_1 = 0.5$), we find that changing the fibre orientation from z-aligned to c-aligned reduces the final value of peak stress by 38.6%, whilst the final value of engineering stress increases by 5%. This decrease in peak stress is still significant, but it is much smaller than in the case of the HGO model (reduction of 94%

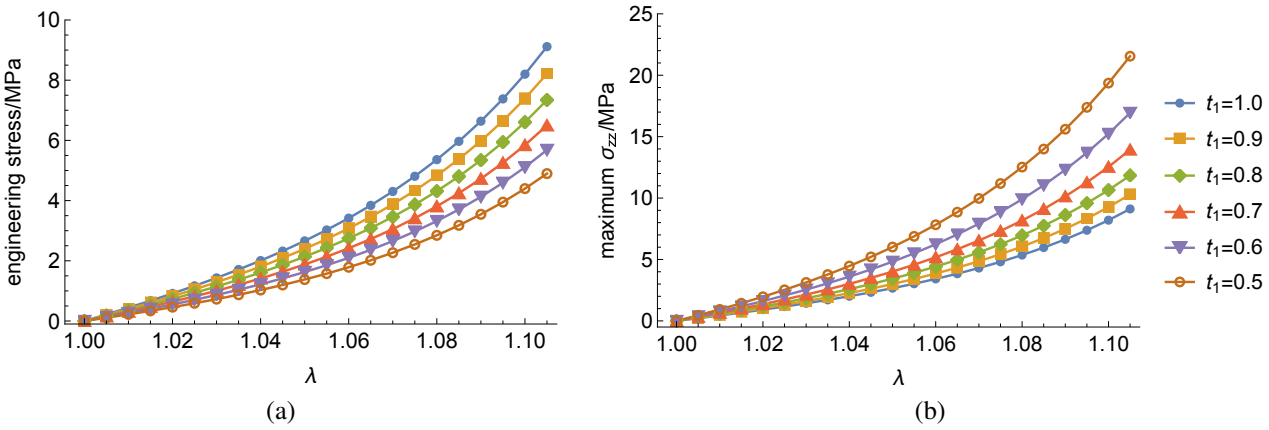

(a) (b)

Figure 3.15: Engineering stress (a) and maximum σ_{zz} (b) against stretch for linearly tapered tendons with c-aligned fibres using the HGO model. The maximum value of σ_{zz} is located in the centre of the smallest cross-section.

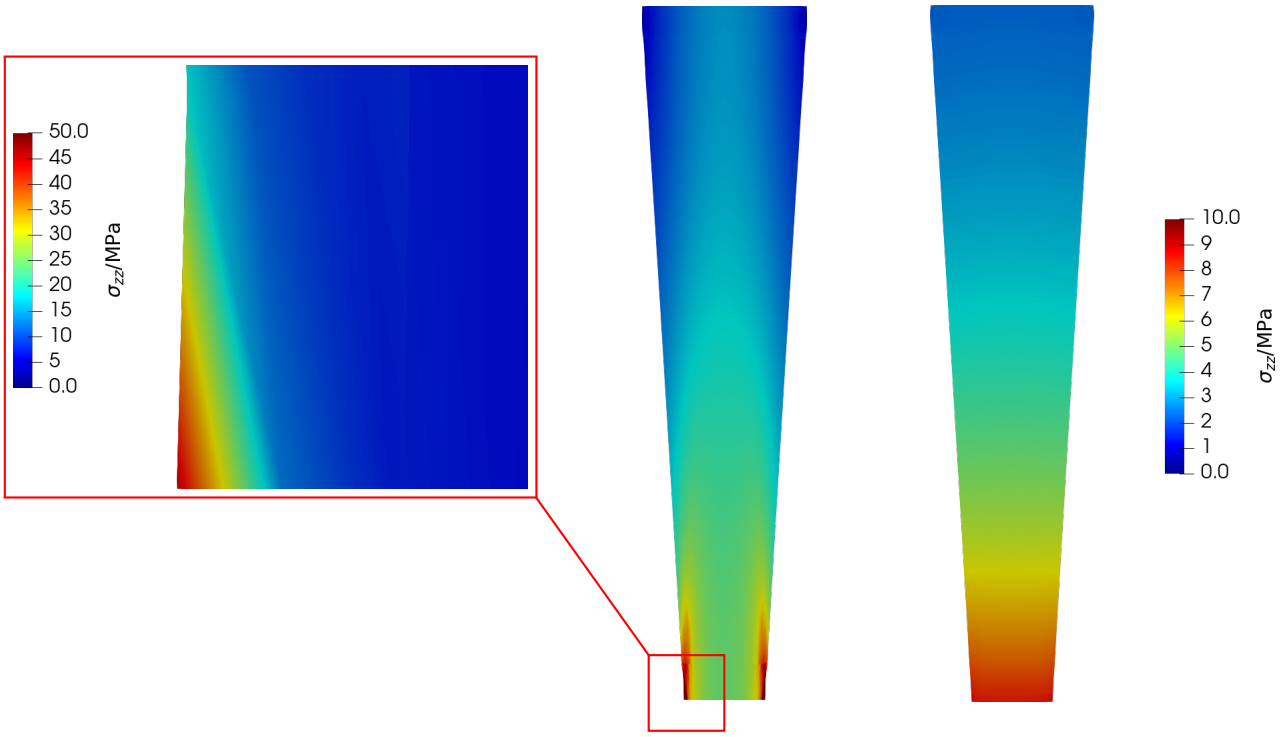

Figure 3.16: Distributions of σ_{zz} within the cross-section of a linearly tapered tendon with $t_1 = 0.5$ at a stretch value of $\lambda = 1.065$. On the left, the fibre direction is aligned with the longitudinal axis of the tendon. On the right, the fibre direction follows the contours of the geometry.

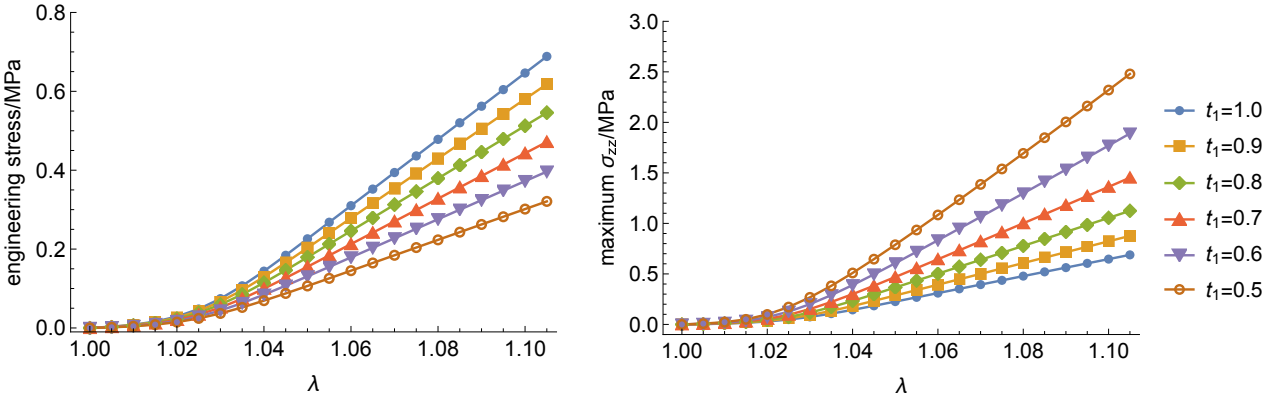

Figure 3.17: Engineering stress (a) and maximum value of σ_{zz} for a linearly tapered tendon with z-aligned fibres using the crimped fibril model. The maximum value of σ_{zz} is located at the outer edge of the smallest cross-section.

at $\lambda = 1.065$), showing that using the crimped fibril model reduces the magnitude of the stress concentrations.

3.6.4 Hourglass taper

Whilst the patellar tendon exhibits a linear taper, other tendons/ligaments, such as the ACL, have a smaller cross-sectional area in the middle than at each end. To incorporate this into our model we can vary t_2, causing the base cylinder to transform into an hourglass shape. We apply the same process as in Section 3.6.3, but we hold s and t_1 constant, whilst varying t_2. Figure 3.19 shows the engineering stress and maximum value of σ_{zz} for a tendon with different values of t_2 using the HGO model with the same material parameters as in Section 3.6.3. We again find that as t_2 decreases, the upper surface of the tendon must increase in size to maintain a constant volume, leading to a decrease in engineering strain. As the centre portion of the tendon decreases in size, the peak value of σ_{zz} increases, as in the linearly tapered case. Figure 3.20 shows the same tests but with c-aligned fibres. Changing from z-aligned fibres to c-aligned fibres with $t_2 = 0.5$ causes the peak stress to decrease by 48% and the maximum engineering stress to increase by 24%.

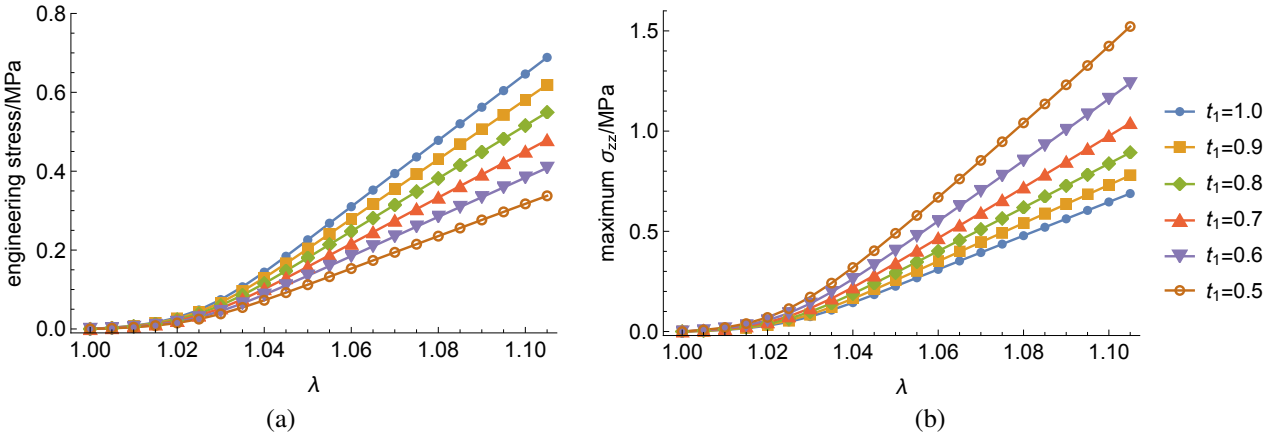

Figure 3.18: Engineering stress (a) and maximum value of σ_{zz} for a linearly tapered tendon with c-aligned fibres using the crimped fibril model. The maximum value of σ_{zz} is located in the centre of the smallest cross-section.

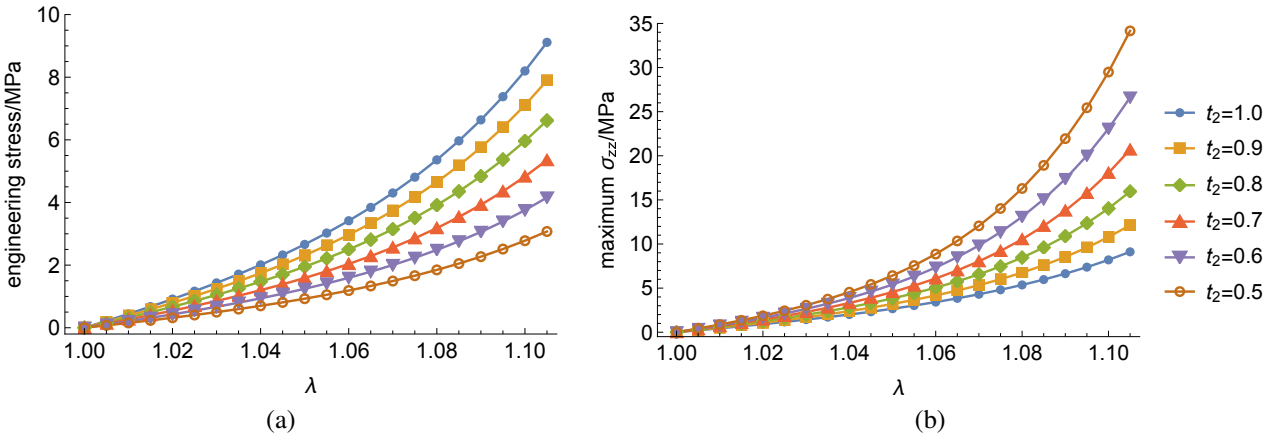

Figure 3.19: Engineering stress (a) and maximum value of σ_{zz} for an hourglass-shaped tendon with z-aligned fibres using the HGO model. The maximum value of σ_{zz} is located at the outer edge of the smallest cross-section.

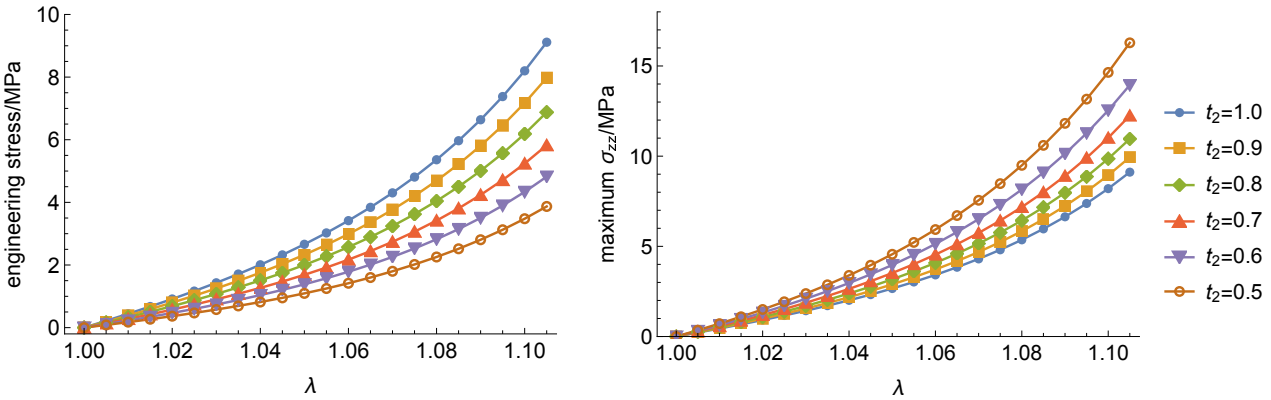

(a) (b)

Figure 3.20: Engineering stress (a) and maximum value of σ_{zz} for an hourglass-shaped tendon with c-aligned fibres using the HGO model. The maximum value of σ_{zz} is located in the centre of the smallest cross-section.

For the crimped fibril model, the figures corresponding to Figure 3.19 and 3.20 can be seen in Figures 3.21 and 3.22, respectively. We find that for $t_2 = 0.5$, when switching from z-aligned to c-aligned fibres, the peak value of σ_{zz} decreases by 14%, whilst the maximum engineering stress increases by 12%.

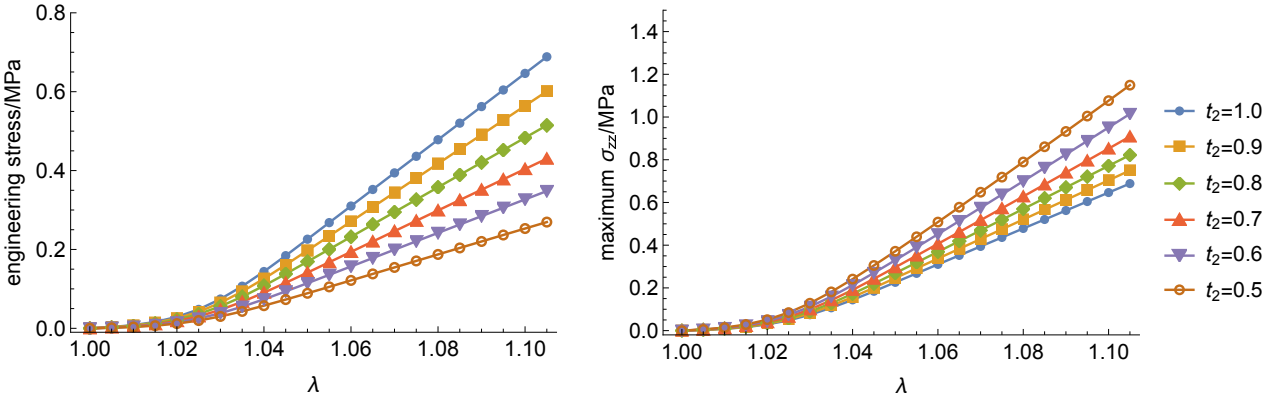

(a) (b)

Figure 3.21: Engineering stress (a) and maximum value of σ_{zz} for an hourglass-shaped tendon with z-aligned fibres using the crimped fibril model.The maximum value of σ_{zz} is located at the outer edge of the smallest cross-section.

From these results we gain some important knowledge about finite element modelling of tendons and ligaments. We find that changing the cross-section of the tendon from circular to elliptic had no effect on the deformation field in the tendon.

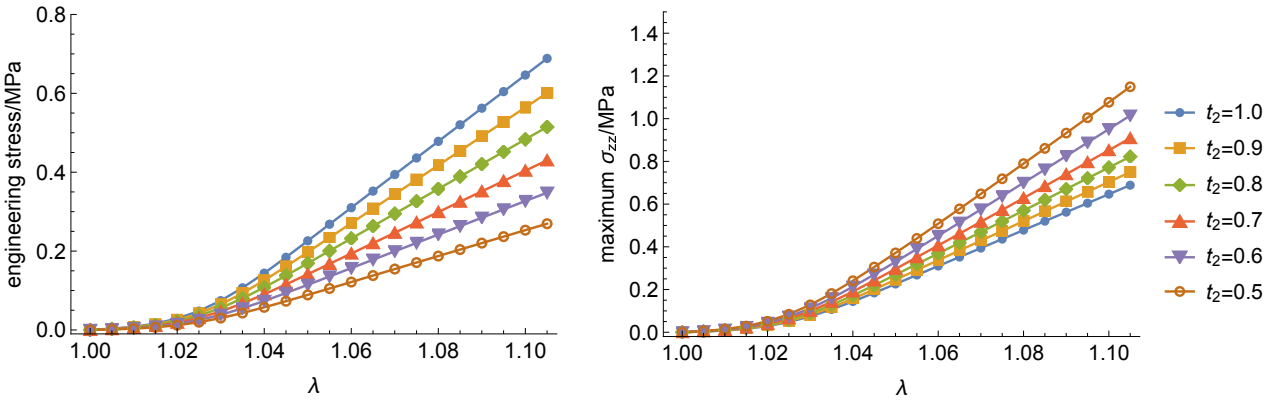

(a) (b)

Figure 3.22: Engineering stress (a) and maximum value of σ_{zz} for an hourglass-shaped tendon with c-aligned fibres using the crimped fibril model. The maximum value of σ_{zz} is located in the centre of the smallest cross-section.

When we allow the cross-sectional area to vary along the length of the tendon, we find that the peak stress increases around the smallest cross-section. We determined that high stress concentrations can arise in certain geometries when the fibres are aligned with the z-axis, rather than following the contours of the geometry. When using the semi-phenomenological HGO model in a tendon with a linear taper, we found that, in the most extreme case, changing the fibres from z- to c-aligned reduced the peak stress by up to 94%. For the crimped fibril model, the corresponding peak stress reduced by 39% – still a significant reduction, but much less than the HGO model. This difference between the two models is because the crimped fibril model is linear above a certain value of stretch, but the HGO model is not.

3.7 Results for specific tendons/ligaments

The results in Section 3.6 allow us to identify some general trends which we can explore further using more realistic geometries and material parameters. We determined that having a cross-section which varies along the length of the tendon introduces a region with a higher peak stress. We found that there is a significant difference between this peak stress, in all geometries, when we change the direction of the fibres from z-aligned to c-aligned. We will therefore focus on the fibre direction in two very different tendon geometries – the Achilles tendon and the ACL. This will allow us to determine

if the differences found in Section 3.6 are equally as significant when more realistic geometries are used. We will also consider different yield criteria in these more realistic geometries in order to test the validity of the von Mises yield criterion. Since there was little qualitative difference between the results produced by the HGO and crimped fibril models, we choose to use the microstructurally-based crimped fibril constitutive model to ensure that all parameters could be measured experimentally.

In addition to the z- and c-aligned fibre configurations, we will consider a third configuration based on the findings of Mommersteeg *et al*. [89], who determined that collagen density increases in the mid-section of the knee ligaments, where the cross-sectional area is smallest. Until now we have assumed that the collagen area fraction, often computed from cross-sectional images of tendons, is equal to the collagen volume fraction. If the fibres follow the geometry of the tendon and are continuous down its length, it may be the case that the density of the collagen fibres increases in regions where the cross-sectional area is smaller, leading to the non-uniform collagen density found by Mommersteeg *et al*. To test the effects this would have on our model, we will assume that the *area* of collagen at height z is constant, rather than the *area fraction*. This leads to a spatially-dependent area fraction of the form

$$\phi(z) = \phi_{\min} \frac{\mathrm{CSA}(z_{\min})}{\mathrm{CSA}(z)}, \tag{3.75}$$

where $\mathrm{CSA}(z)$ is the cross-sectional area at height z, $z_{\min}$ is the height with the smallest cross-section, and $\phi_{\min}$ is the area fraction at $z_{\min}$. We choose

$$\phi_{\min} = \frac{\phi_{\mathrm{const}} V}{\mathrm{CSA}(z_{\min}) L}, \tag{3.76}$$

where V is the volume of the tendon, to match the volume of collagen with a tendon possessing a uniform distribution of collagen with constant area fraction ϕ_{const}, thereby ensuring that $\phi(z) < 1$ for $0 \leq z \leq L$.

3.7.1 Achilles tendon

The first tendon we will model is the Achilles tendon, which stretches from the heel to the soleus muscles of the calf. The Achilles tendon is the thickest in the body and

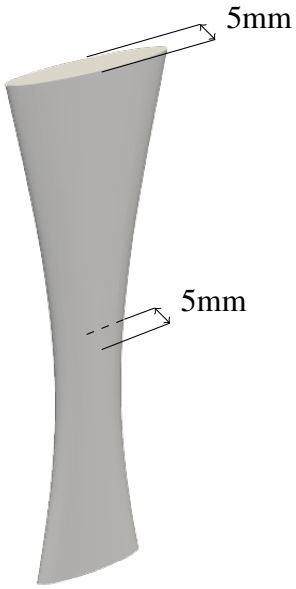

Figure 3.23: When modelling the Achilles tendon, we assume a constant semi-minor axis of 2.5mm. The upper semi-major axis is 1.64cm, the central semi-major axis is 0.81cm, and the lower semi-major axis is 1.61cm.

has a broad, flat shape which narrows towards the centre [90]. We use measurements presented by Reeves *et al.* [91] to approximate the Achilles tendon geometry. We assume an upper semi-major axis of 1.64cm, a lower semi-major axis of 1.61cm and a central semi-major axis of 0.81cm. We assume a constant semi-minor axis of 2.5mm down the entire length of the tendon, as shown in Figure 3.23. These measurements lead to geometric parameter values of $s = 0.15$, $t_1 = 0.98$ and $t_2 = 0.50$[1], and ensure that the cross-sectional area at the top, centre, and bottom of the tendon match the values calculated by Reeves *et al.* We use $L = 17$cm and choose $\phi_{\text{const}} = 0.65$, leading to a value of $\phi_{\text{min}} = 0.86$ for the spatially-varying collagen fraction. The value of ϕ_{const} is chosen arbitrarily to ensure $\phi_{\text{min}} < 1$, but both values fall within the experimentally observed range [20].

A plot of $\phi(z)$ for this geometry can be seen in Figure 3.24. We use a ground state shear modulus of $\mu = 50$MPa and a collagen Young's modulus of 2.5GPa. This value of E is consistent with values obtained experimentally, and μ was chosen to ensure the

[1]The actual value used in the finite element model was $t_2 = 0.53$.

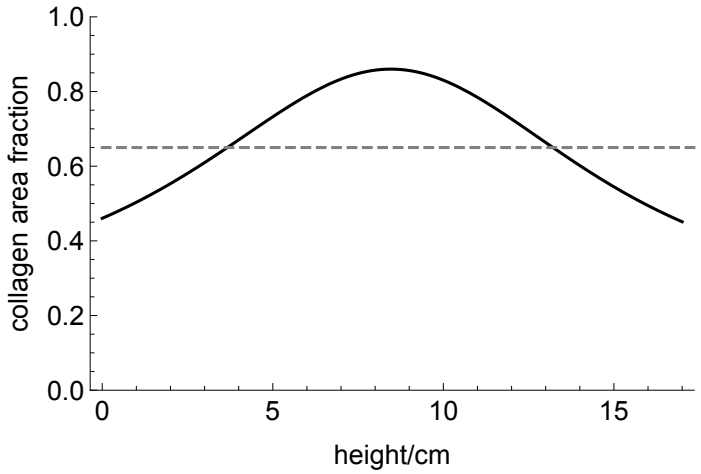

Figure 3.24: Collagen area fraction as a function of height for the Achilles tendon. The solid line shows the spatially varying area fraction defined in equation (3.75), whilst the dashed line shows the equivalent constant area fraction. In both cases the total volume of collagen is equal.

ratio between the two values was not too large. The distribution parameters remain unchanged at $a = 1.0$, $b = 1.05$, and $c = 1.025$. In this geometry we will compare three different fibre configurations: z-aligned fibres, c-aligned fibres with constant ϕ, and c-aligned fibres with spatially varying $\phi = \phi(z)$. The engineering stress for the three fibre configurations can be seen in Figure 3.25.

Instead of considering the maximum value of σ_{zz}, we will now consider the transformed Cauchy stress σ'_{zz}, defined in equation (3.72), because we will be using an anisotropic yield criterion to predict locations of failure in the tissue. Such a criterion requires the stress in the direction of the fibres, as described in Section 3.5.3. A plot of the maximum value of σ'_{zz} can be found in Figure 3.26, and distributions of σ'_{zz} can be seen in Figure 3.27.

Figures 3.25 and 3.26 show the same trend as in Section 3.6. Switching from z- to c-aligned fibres with constant ϕ increases the final engineering stress by 5% and decreases the maximum value of σ'_{zz} by 31%. In the c-aligned case, changing from a constant ϕ to a spatially-varying ϕ increases the engineering stress by 4%, and the maximum value of σ'_{zz} by 4%. The stress distributions in Figure 3.27 show that when the fibres are aligned with the z-axis, there is a large stress concentration at the edges of the most narrow part of the tendon. To determine the cause of the stress concentrations in this configuration,

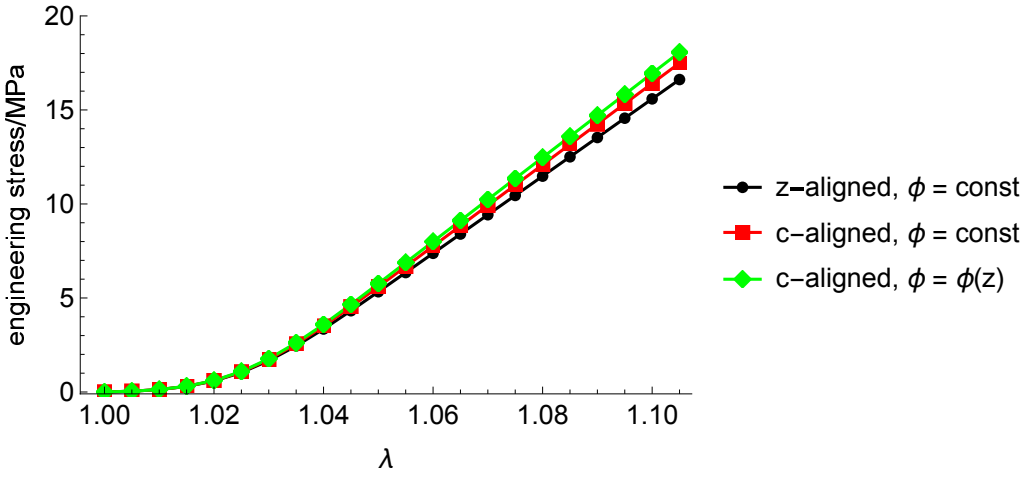

Figure 3.25: Engineering stress against stretch for the Achilles tendon with three different fibre configurations.

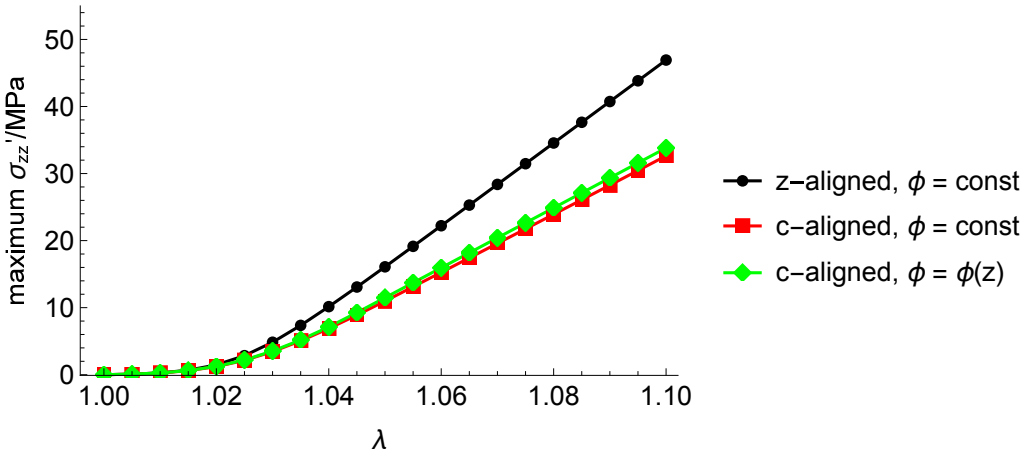

Figure 3.26: The maximum value of the Cauchy stress in the direction of the fibres σ'_{zz} as a function of stretch for three different fibre orientations within the Achilles tendon. For z-aligned fibres, the maximum value of σ'_{zz} is found at the outer edge of the smallest cross-section. For c-aligned fibres it is found in the centre of the smallest cross-section.

we consider the internal deformation in the z-direction and how this differs from the homogeneous deformation field observed in a right-circular cylinder. We define the the z-inhomogeneity at a height z in the deformed configuration to be

$$u_z = z - \lambda Z, \tag{3.77}$$

where Z is the height of the point in the undeformed body. Figure 3.28 shows the z-inhomogeneity for the three fibre configurations.

We can see from Figure 3.28 that z-aligned fibres cause a significant amount of additional deformation in the z-direction compared with the homogeneous deformation of a right-circular cylinder. The outer edge of the tendon deforms in a way that puts additional strain on the mid-section, leading to the high stress concentrations observed in Figure 3.27. For c-aligned fibres with constant ϕ, we see a more even distribution of u_z across the radius of the tendon. In this case there is still additional strain placed on the mid-section, again leading to an increase in stress in that region. For c-aligned fibres with spatially-varying ϕ, it appears from Figure 3.28 as though the deformation is homogeneous. However, adjusting the scale allows us to see that there is some slight inhomogeneity. This is shown in Figure 3.29.

The deformation deviation fields presented in Figure 3.29 are roughly ten times smaller in magnitude than for the z-aligned fibre configuration. We see similar deformation around the upper and lower edges of the tendon, but now with a thin vertical band in the very centre, which is present for both constant and spatially-varying ϕ. This is responsible for the corresponding vertical band of stress observed in Figure 3.27. By increasing the value of ϕ where the cross-sectional area is smallest, we have eliminated some of the additional deformation, leaving only the edges and the band in the centre. The central band may be explained physically if we consider fibrils passing through this part of the tendon. When we have c-aligned fibres, they are all different lengths within the tendon (ignoring any crimp). The fibrils closest to the centre of the tendon will be shortest and will therefore be stretched more in the z-direction in order to maintain the globally prescribed strain. With z-aligned fibres, all of the fibrils in this region are the same length and point in the same direction, so we do not see this effect. The additional deformation present at the edges of the tendon is related to the stiffness of the outer boundary itself. As the tendon is stretched, the convex outer boundary will

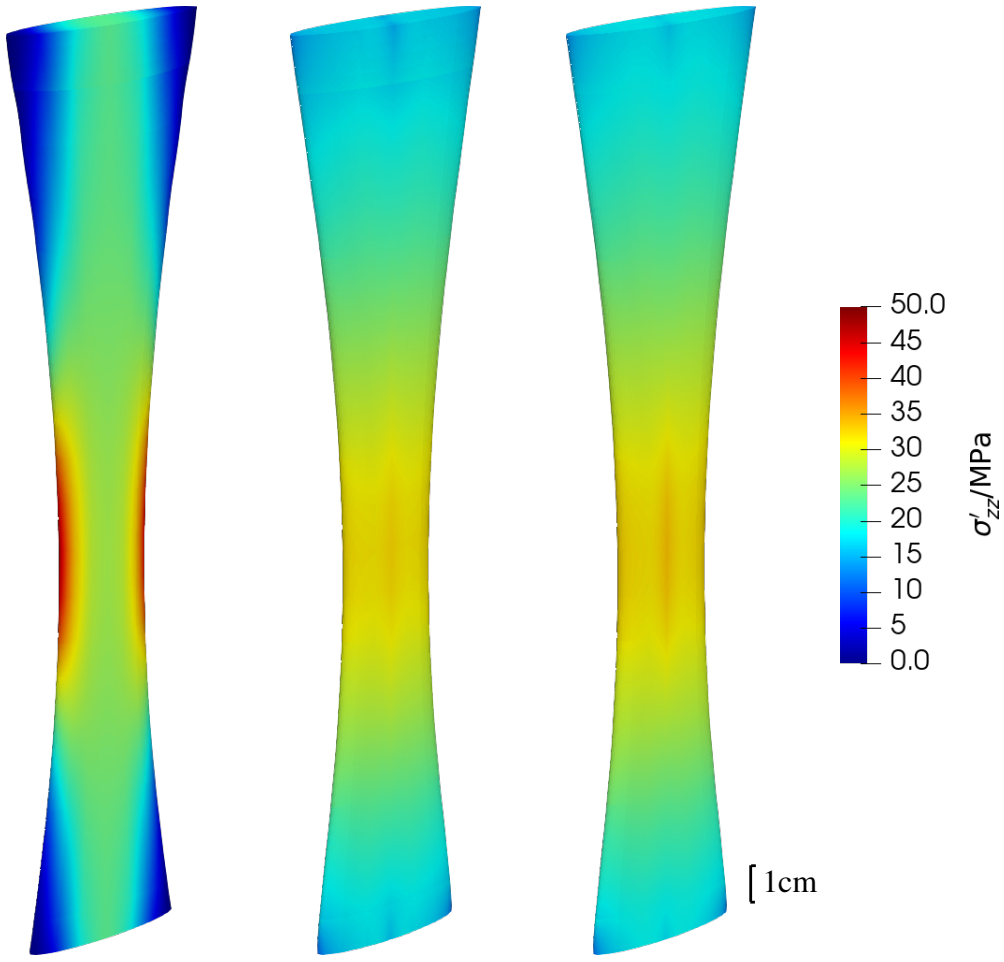

Figure 3.27: Distributions of stress in the Achilles tendon with three different fibre orientations. On the left, fibres are aligned with the longitudinal axis of the tendon (z-aligned) and collagen volume fraction is constant. In the middle, fibres follow the contours of the geometry (c-aligned) and the collagen volume fraction is constant. On the right, fibres are c-aligned and the collagen volume fraction varies with height, as shown in Figure 3.24. The stress measure used is the zz-component of the Cauchy stress rotated to be aligned with the direction of the fibres, σ'_{zz}.

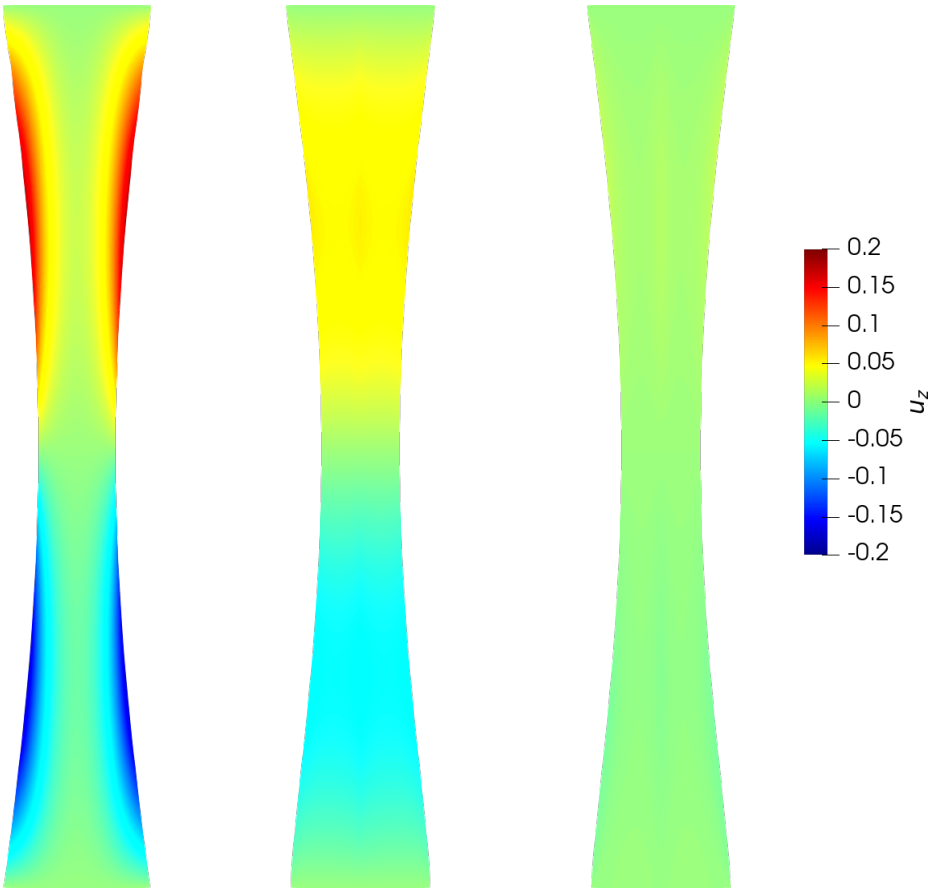

Figure 3.28: Distributions of u_z, the z-inhomogeneity defined in equation (3.77), in a cross-section of the Achilles tendon. On the left, the fibres are are z-aligned and the collagen volume fraction is constant. In the middle, the fibres are c-aligned and the collagen volume fraction is constant. On the right, the fibres are c-aligned and the collagen volume fraction is spatially-dependent.

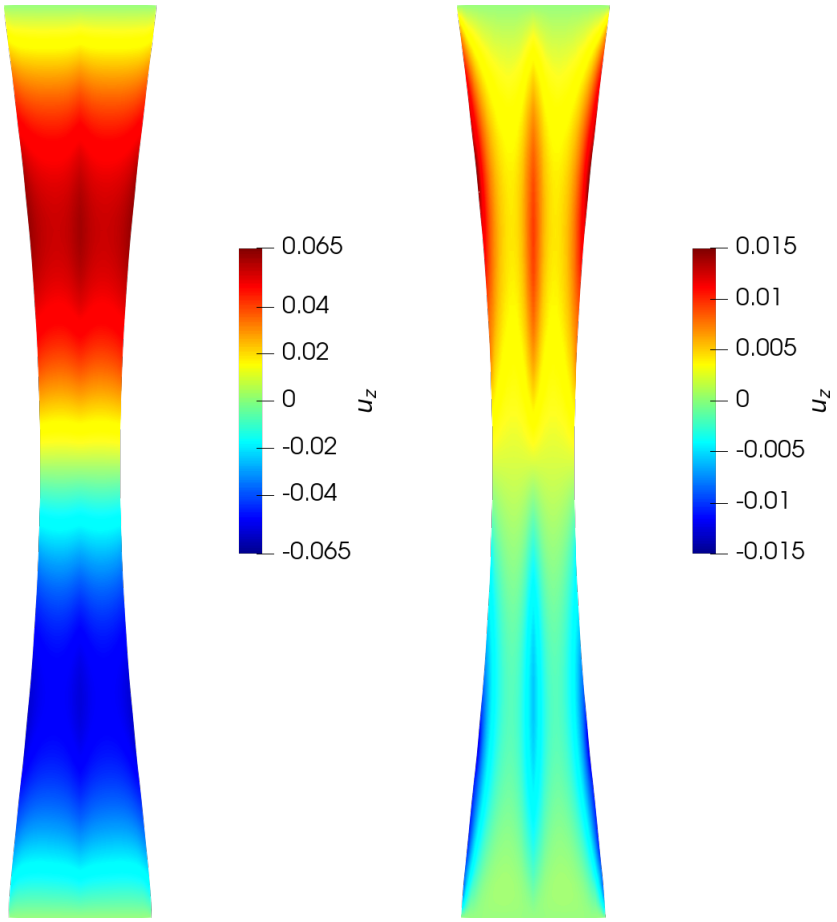

Figure 3.29: A cross-section of the Achilles tendon showing the distribution of u_z, the z-inhomogeneity defined in equation (3.77). In both plots the fibres are c-aligned. On the left, ϕ is constant, whilst on the right, $\phi = \phi(z)$. This figure shows the same quantity as Figure 3.28, but scaled to the visible range.

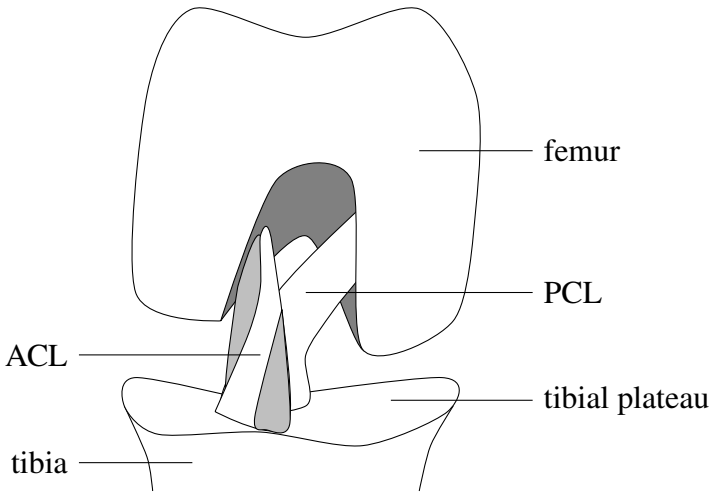

Figure 3.30: An anterior view of the junction between the femur and the tibia when the right knee is in flexion, illustrating the positioning of the cruciate ligaments. Included are the anterior cruciate ligament (ACL), comprised of two bundles of fibres wrapped around one another, and the posterior cruciate ligament (PCL). Diagram based on photographs by Petersen et al. [93]

flex, resulting in additional vertical displacement. For c-aligned fibres this effect is not strong enough to produce stress concentrations, but for z-aligned fibres the effect is significantly stronger. This may be because the largest component of force is being carried in the direction of the fibres, which for z-aligned fibres is vertically.

3.7.2 Anterior cruciate ligament

The Anterior Cruciate Ligament (ACL) connects the lateral femoral condyle to the anterior intercondylar area of the tibia, as can be seen in Figure 3.30. It is vital for joint stability and is commonly injured during high-impact sports and exercise [92], making it a good candidate for finite element modelling. The ACL has an interesting geometry, being composed of two distinct bundles of fascicles which wrap around each other between their insertion sites.

We use measurements from Fujimaki *et al.* [94] to estimate the geometric parameters required to approximate the ACL geometry within our idealised framework. We assume an upper semi-major axis of 7.3mm, a lower semi-major axis of 6.4mm, a middle semi-major axis of 4.3mm, and a length of $L = 24$mm. We use $s = 0.7$, $t_1 = 0.88$, and

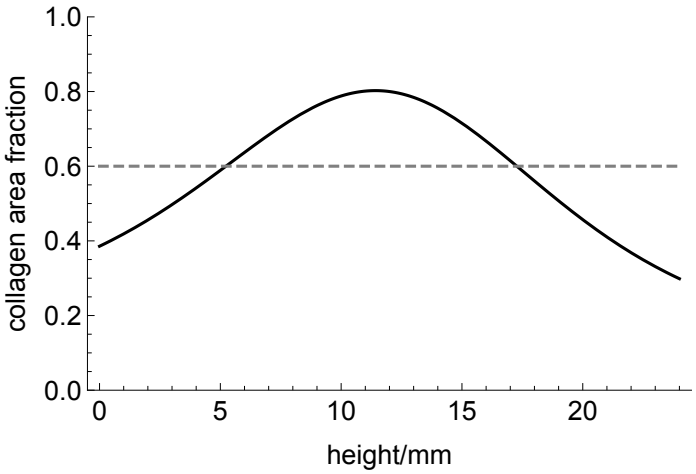

Figure 3.31: Collagen area fraction against height in the idealised model of the ACL. The solid black line shows the spatially-varying area fraction, whilst the dashed line represents the constant area fraction. In both cases the total volume of collagen is the same.

$t_2 = 0.63$. Unlike for the Achilles tendon, we do not assume that the ACL has a constant semi-minor axis, instead allowing the radius to change in both the x- and y-directions down the length of the tendon, using equation (3.58). These geometric parameter values ensure that the cross-sectional area of the ACL matches the values calculated by Fujimaki *et al*. We use the same material parameters as in the previous section, but choose $\phi_{\text{const}} = 0.6$, leading to $\phi_{\text{min}} = 0.84$. These values still fall within the range observed experimentally [20]. Figures 3.32 and 3.33 show the engineering stress and maximum value of σ'_{zz}, respectively. Switching from z-aligned fibres to c-aligned fibres shows a similar trend to the Achilles tendon with the maximum engineering stress increasing by 10% for constant ϕ and 12% for spatially-varying ϕ. We see the maximum value of σ'_{zz} decrease by 33% for constant ϕ and 32% for spatially-varying ϕ. This once again demonstrates that choosing a more realistic fibre direction has a large impact on both the average and maximum stress. We also see similar stress distributions to the Achilles tendon, as shown in Figure 3.34.

From Figure 3.34, we see stress concentrations appearing around the centre of the ACL when z-aligned fibres are used. In contrast to the Achilles tendon, this stress concentration is present around the entire circumference of the ACL, since we have not assumed a constant semi-minor axis. For the c-aligned fibres, we see the same

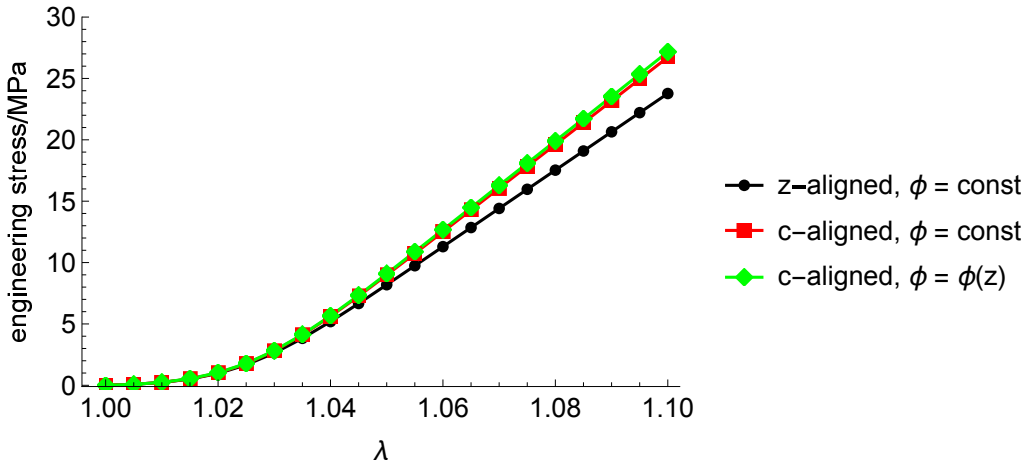

Figure 3.32: Engineering stress against stretch for the ACL with three different fibre configurations.

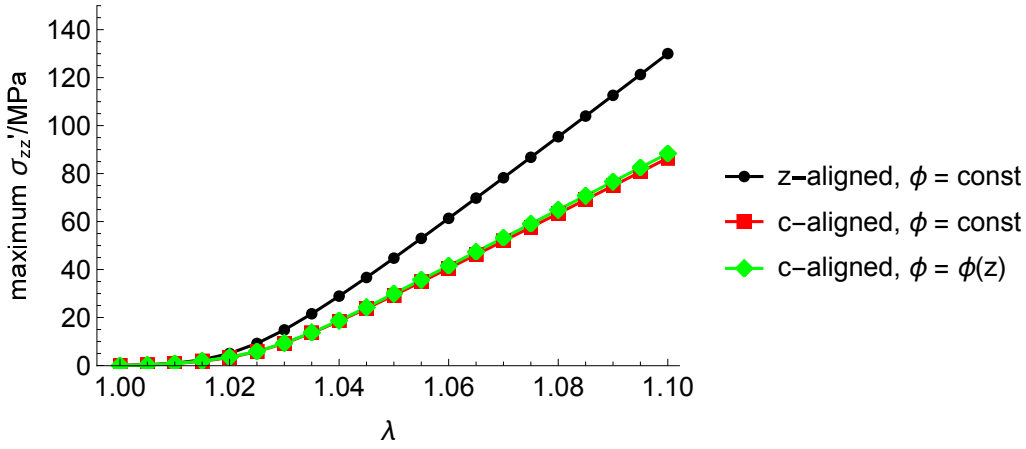

Figure 3.33: The maximum value of the Cauchy stress in the direction of the fibres σ'_{zz} as a function of stretch for three different fibre configurations within the ACL. For z-aligned fibres, the maximum value of σ'_{zz} is found at the outer edge of the smallest cross-section. For c-aligned fibres it is found in the centre of the smallest cross-section.

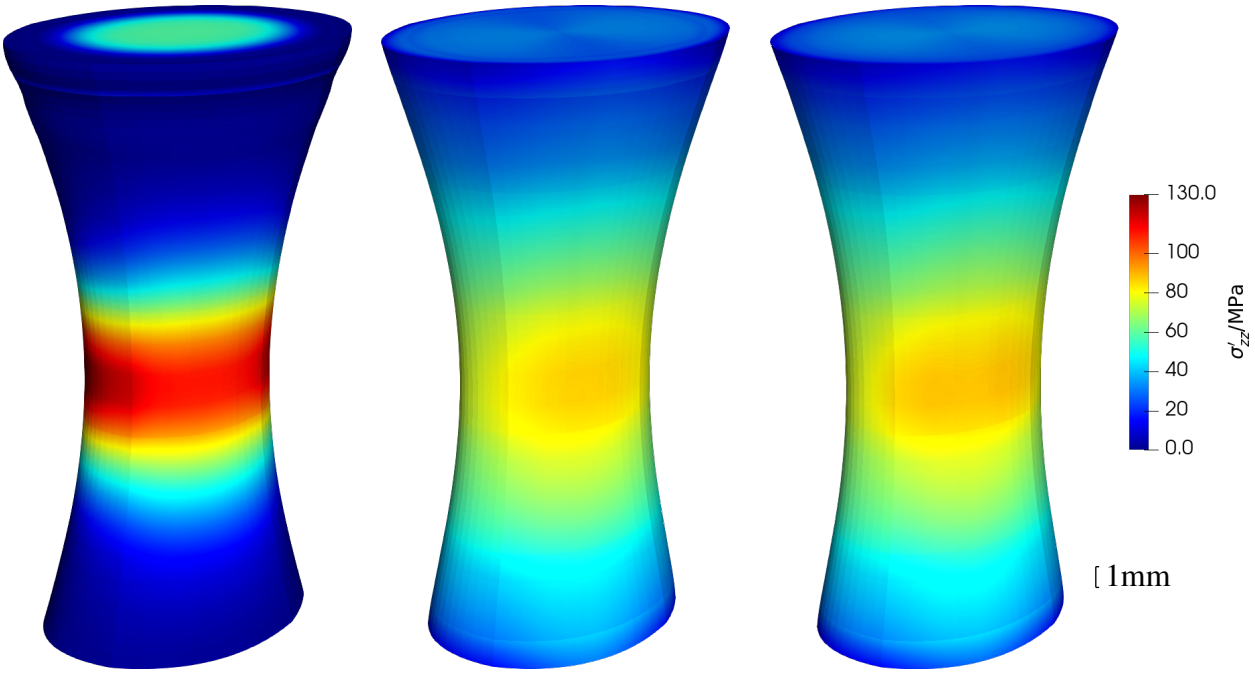

Figure 3.34: Distributions of σ'_{zz}, defined in equation (3.72), within the ACL. On the left, fibres are aligned with the z-axis. In the middle, fibres are c-aligned and ϕ is constant. On the right, fibres are c-aligned and ϕ varies in space.

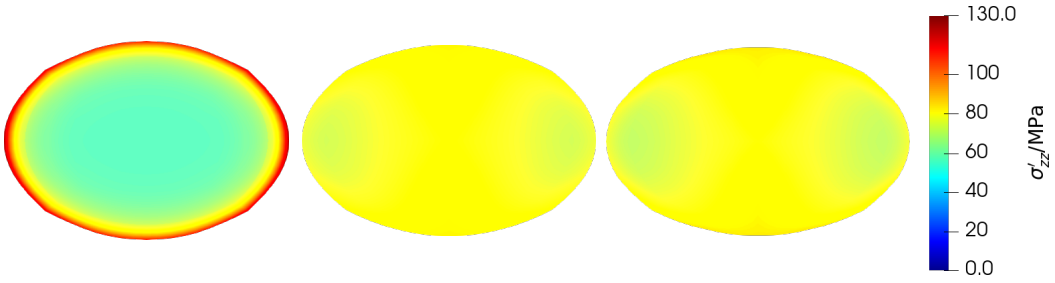

Figure 3.35: Distributions of σ'_{zz} within a central cross-section of the ACL with normal in the z-direction. On the left, fibres are aligned with the z-axis. In the middle, fibres are c-aligned and ϕ is constant. On the right, fibres are c-aligned and ϕ is spatially-varying.

vertical banding appearing on the wider faces of tendon. Figure 3.35 shows the stress distribution within a cross-section with normal in the z-direction positioned directly in the centre of the tendon. For z-aligned fibres we see that the stress concentrations do not penetrate far into the tissue, whilst for c-aligned fibres we find that the stress is more homogeneous throughout the cross-section. Figure 3.36 shows the z-inhomogeneity in a cross-section of the ACL for the three fibre configurations under consideration. Similar to the Achilles tendon, we see more deformation around the outer edges, causing the curved boundary to be pulled towards the flat ends of the tissue. For c-aligned fibres with constant ϕ, we see the deformation has been spread out across the whole radius of the ligament, as we saw in Figure 3.28 for the Achilles tendon. Interestingly, when we consider spatially-varying ϕ, we see that the direction in which the bulk of the tissue is being displaced, relative to the deformation of a right-circular cylinder, has been flipped. In all other cases, we saw material at either side of the mid-point being stretched towards the ends of the tissue relative to the homogeneous deformation, whereas in this case we see it being pulled towards the centre. This is because, in this configuration, the stiffness at the centre of the ACL is significantly higher than at the ends, causing material to be pulled towards the centre, relative to the homogeneous deformation.

Rescaling the axis of Figure 3.36 to the visible range for the c-aligned fibre configurations yields Figure 3.37. Here we see interesting structure emerging at a lower magnitude of z-inhomogeneity than the banding present in the z-aligned fibre case. For spatially-varying ϕ, we see that at the outer edge of the ACL, the boundaries displace towards the upper and lower edges, whilst the tissue in the centre moves toward the

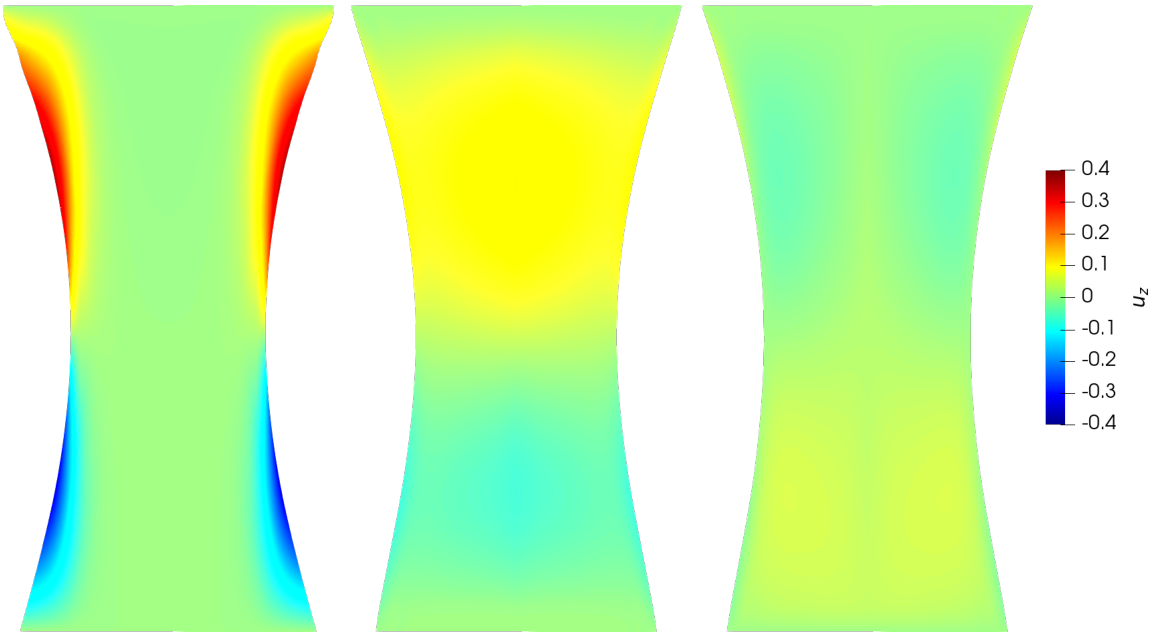

Figure 3.36: Distributions of u_z, the z-inhomogeneity defined in equation (3.77), in a cross-section of the ACL. On the left, the fibres are are z-aligned and the collagen volume fraction is constant. In the middle, the fibres are c-aligned and the collagen volume fraction is constant. On the right, the fibres are c-aligned and the collagen volume fraction is spatially-dependent.

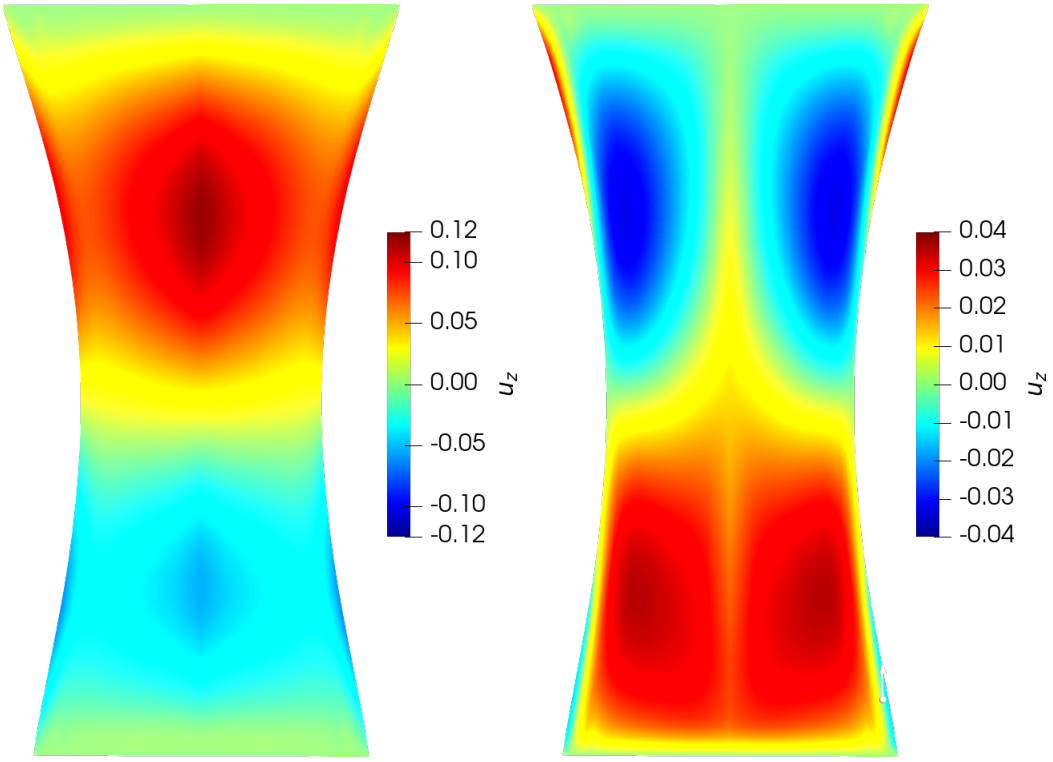

Figure 3.37: A cross-section of the ACL showing the distribution of u_z, the z-inhomogeneity defined in equation (3.77). In both plots the fibres are c-aligned. On the left, ϕ is constant, whilst on the right, $\phi = \phi(z)$. This figure shows the same quantity as Figure 3.36, but scaled to the visible range.

mid-point of the ligament, relative to the homogeneous case, as previously described.

3.8 Evaluation of yield criteria

3.8.1 Achilles tendon

In order to evaluate the performance of the von Mises and Hill yield criteria, we consider the finite element model of the Achilles tendon presented in Section 3.7.1. We choose to focus on this tendon over the ACL, because our idealised geometry more accurately represents the shape and structure of the Achilles tendon. To determine the importance of material strength anisotropy, we define the material strength factor $\gamma \in (0,1]$. We assume that the yield stress of the fibres is $\sigma_z^Y = 230$MPa and set the value of all other yield stresses to be $\sigma_i^Y = \gamma\sigma_z^Y$. This value of yield stress was chosen because it produced yielding when substituted into the von Mises yield criterion along with the finite element results in Section 3.7.1. We set the yield stresses in shear to be $\tau_{ij}^Y = \sigma_z^Y/\sqrt{3}$, leading to the following values of the Hill parameters F, G, H, L, M and N (introduced in Section 2.2.6),

$$F = \frac{1}{2}\left(\frac{1}{(\gamma\sigma_z^Y)^2} + \frac{1}{(\sigma_z^Y)^2} - \frac{1}{(\gamma\sigma_z^Y)^2}\right), \tag{3.78}$$

$$G = \frac{1}{2}\left(\frac{1}{(\sigma_z^Y)^2} + \frac{1}{(\gamma\sigma_z^Y)^2} - \frac{1}{(\gamma\sigma_z^Y)^2}\right), \tag{3.79}$$

$$H = \frac{1}{2}\left(\frac{1}{(\gamma\sigma_z^Y)^2} + \frac{1}{(\gamma\sigma_z^Y)^2} - \frac{1}{(\sigma_z^Y)^2}\right), \tag{3.80}$$

$$L = \frac{3}{2(\sigma_z^Y)^2}, \tag{3.81}$$

$$M = \frac{3}{2(\sigma_z^Y)^2}, \tag{3.82}$$

$$N = \frac{3}{2(\sigma_z^Y)^2}. \tag{3.83}$$

By setting $\gamma = 1$, the Hill criterion (given in equation (2.45)) reduces to the von Mises criterion (given in equation (2.43)). There is limited data available for the strength of soft tissue in directions transverse to the fibres and we will therefore investigate the effects of γ on failure in our finite element model. Shown in Figure 3.38 is the results of this analysis for $\lambda = 1.1$. We clearly see that for z-aligned fibres, values of $\gamma = 1$, $\gamma = 0.25$, and $\gamma = 0.1$ all produce potential regions of failure (where the yield stress

exceeds 1) around the edges of the tendon mid-substance, where the cross-sectional area is smallest. For c-aligned fibres we see that values of $\gamma = 1$ and $\gamma = 0.25$ are not low enough to produce regions of failure at this level of stretch. However when $\gamma = 0.1$, we see the edges of the tendon closer to the ends become potential regions of failure, as shown by the dark red areas in Figures 3.38(f) and 3.38(i). In this instance the matrix is weak enough so that the distortion in the transverse plane builds up enough stress to exceed the limit imposed by the criterion.

3.8.2 Analytic tension-torsion of a cylinder

To further test the validity of isotropic and anisotropic yield criteria, we now consider a slightly more complex deformation for which we can produce an analytic solution for the stress. Returning to the base problem defined in Section 3.5.1, we now impose a twist Ψ to the upper surface of the cylinder, on top of the uniaxial extension. This superposition of deformations leads to a plane at height z being subjected to a twist of $z\Psi$. Figure 3.39 shows an updated outline of the base problem. We will begin by finding an analytic expression for the stress in a transversely isotropic cylinder subject to these boundary conditions. We will then compare the isotropic von Mises yield criterion to the anisotropic Hill yield criterion using the calculated stress field.

The deformation gradient tensor and left Cauchy-Green deformation tensor are given by

$$\mathbf{F} = \begin{pmatrix} \frac{1}{\sqrt{\lambda}} & 0 & 0 \\ 0 & \frac{1}{\sqrt{\lambda}} & r\psi\lambda \\ 0 & 0 & \lambda \end{pmatrix} \quad \text{and} \quad \mathbf{B} = \begin{pmatrix} \frac{1}{\lambda} & 0 & 0 \\ 0 & \frac{1}{\lambda} + r^2\psi^2\lambda^2 & r\psi\lambda^2 \\ 0 & r\psi\lambda^2 & \lambda^2 \end{pmatrix}, \tag{3.84}$$

respectively. The fibre direction in the initial configuration is $\mathbf{M} = (0,0,1)^{\mathrm{T}}$, whilst in the deformed configuration it is given by

$$\mathbf{m} = \mathbf{F}\mathbf{M} = \begin{pmatrix} 0 \\ r\psi\lambda \\ \lambda \end{pmatrix}. \tag{3.85}$$

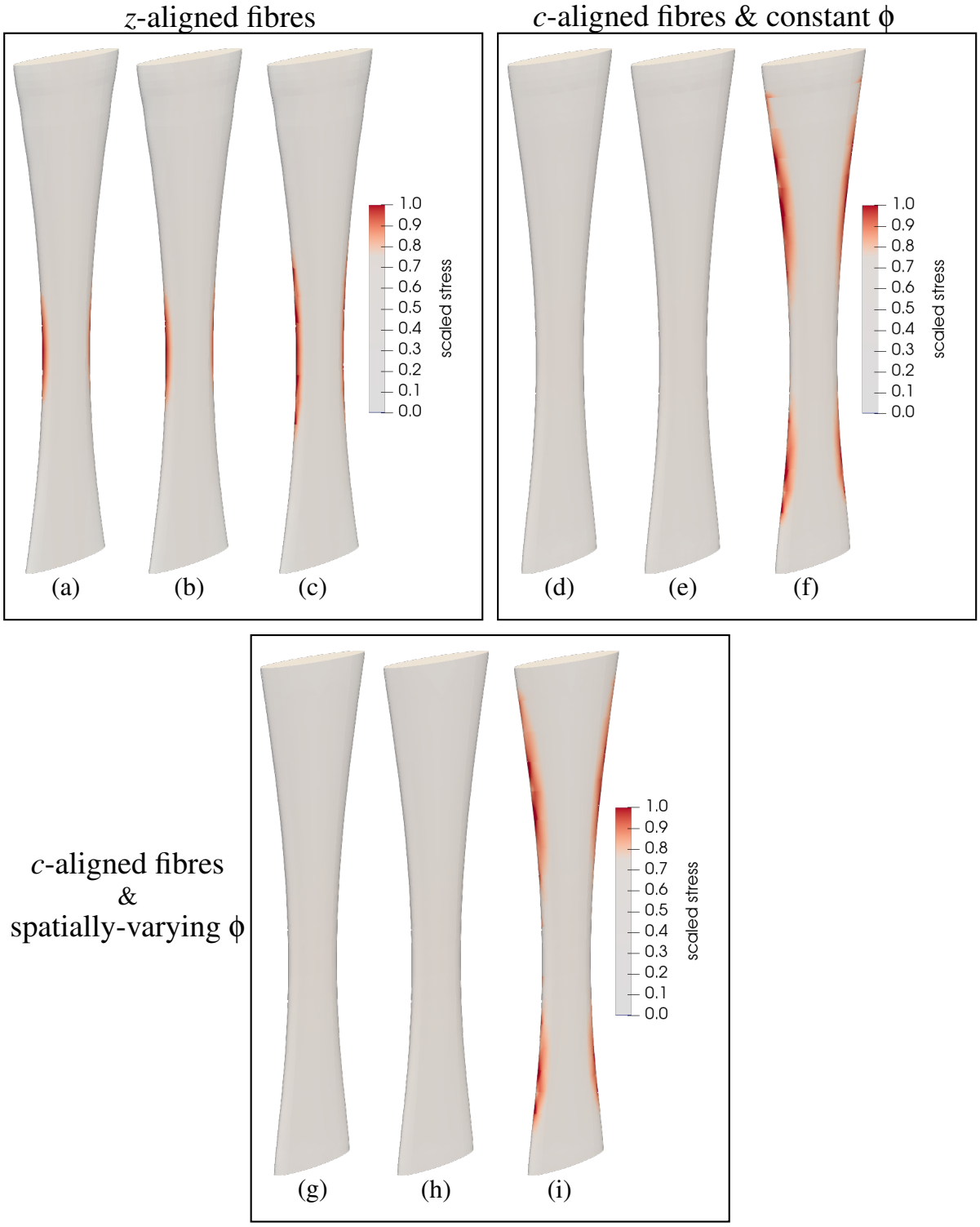

Figure 3.38: The distribution of scalar stress measures defined by different yield criteria in the Achilles tendon after having been stretched by a factor of $\lambda = 1.1$. The stress measures are scaled to the material strength – a value of 1 corresponds to a potential failure location. In (a): z-aligned fibres and von Mises stress, (b): z-aligned fibres and Hill stress with $\gamma = 0.25$, (c): z-aligned fibres and Hill stress with $\gamma = 0.1$, (d): c-aligned fibres with constant ϕ and von Mises stress, (e): c-aligned fibres with constant ϕ and Hill stress with $\gamma = 0.25$, (f): c-aligned fibres with constant ϕ and Hill stress with $\gamma = 0.1$, (g): c-aligned fibres with spatially-varying ϕ and von Mises stress, (h): c-aligned fibres with spatially-varying ϕ and Hill stress with $\gamma = 0.25$, (i): c-aligned fibres with spatially-varying ϕ and Hill stress with $\gamma = 0.1$.

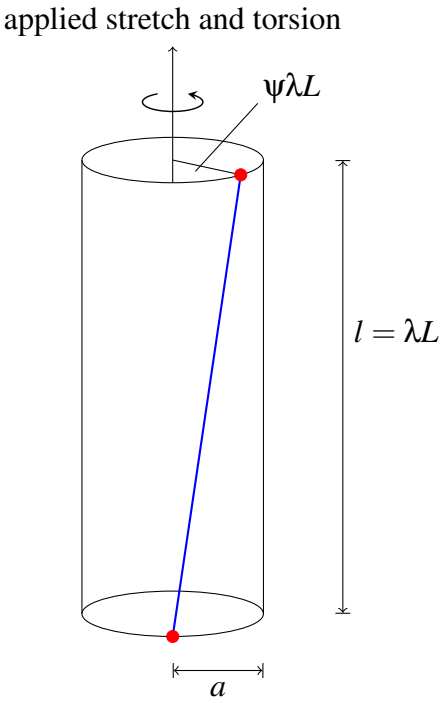

Figure 3.39: An updated version of the base problem in Figure 3.3. We now apply a twist Ψ to the top surface of the cylinder after stretching by a factor of λ.

After calculating the strain invariants we have

$$I_1 = \mathrm{Tr}(\mathbf{C}) = \frac{2}{\lambda} + \lambda^2 + r^2\lambda^2\psi^2, \tag{3.86}$$

$$I_2 = \frac{1}{2}(\mathrm{Tr}(\mathbf{C})^2 - \mathrm{Tr}(\mathbf{C^2})) = \frac{1}{\lambda^2} + 2\lambda + r^2\psi^2\lambda, \tag{3.87}$$

$$I_3 = \det(\mathbf{C}) = 1, \tag{3.88}$$

$$I_4 = \mathbf{M}\cdot(\mathbf{CM}) = \lambda^2 + r^2\lambda^2\psi^2. \tag{3.89}$$

Following the same process as in Section 3.5.1, we find that the components of the Cauchy stress are given by

$$\sigma_{11} = -p + \frac{2W_1}{\lambda}, \tag{3.90}$$

$$\sigma_{12} = \sigma_{21} = \sigma_{13} = \sigma_{31} = 0, \tag{3.91}$$

$$\sigma_{22} = -p + \frac{2W_1}{\lambda} + 2(W_1 + W_4)r^2\psi^2\lambda^2, \tag{3.92}$$

$$\sigma_{23} = \sigma_{32} = 2(W_1 + W_4)r\psi\lambda^2, \tag{3.93}$$

$$\sigma_{33} = -p + 2(W_1 + W_4)\lambda^2. \tag{3.94}$$

Inserting these into the equilibrium equations, $\nabla\cdot\sigma = \mathbf{0}$, leads to

$$\frac{\partial p}{\partial\theta} = 0 \qquad \text{and} \qquad \frac{\partial p}{\partial z} = 0, \tag{3.95}$$

for the θ- and z-components. The r-component gives

$$\begin{aligned}
&(\nabla\cdot\sigma)_r = \frac{\partial\sigma_{11}}{\partial r} + \frac{1}{r}(\sigma_{11} - \sigma_{22}) = 0 \\
\implies &\frac{\partial}{\partial r}\left[-p + \frac{2W_1}{\lambda}\right] + \frac{1}{r}\left[2(W_1 + W_4)r^2\psi^2\lambda^2\right] = 0 \\
\implies &\frac{\partial p}{\partial r} = 2(W_1 + W_4)r\psi^2\lambda^2 \\
\implies &p = (W_1 + W_4)r^2\psi^2\lambda^2 + p_0,
\end{aligned} \tag{3.96}$$

where p_0 is a constant and we have assumed that $\frac{\partial W}{\partial r} = 0$, as is the case for both the HGO and crimped fibril models. We can now apply the traction-free boundary condition to

the outer surface of the cylinder,

$$\boldsymbol{\sigma}\cdot\mathbf{n}=\mathbf{0} \qquad \text{at} \qquad r=a, \tag{3.97}$$

where $\mathbf{n}=(1,0,0)^{\mathrm{T}}$ is the outer unit normal to the curved surface of the cylinder. Application of the boundary condition yields

$$p_0=\frac{2W_1}{\lambda}-(W_1+W_4)a^2\psi^2\lambda^2. \tag{3.98}$$

Substituting (3.96) and (3.98) into (3.90)–(3.94) produces the following expressions for the components of Cauchy stress,

$$\sigma_{11}=(W_1+W_4)(a^2-r^2)\psi^2\lambda^2, \tag{3.99}$$

$$\sigma_{12}=\sigma_{21}=\sigma_{13}=\sigma_{31}=0, \tag{3.100}$$

$$\sigma_{22}=(W_1+W_4)(a^2+r^2)\psi^2\lambda^2, \tag{3.101}$$

$$\sigma_{23}=\sigma_{32}=2(W_1+W_4)r\psi\lambda^2, \tag{3.102}$$

$$\sigma_{33}=(W_1+W_4)(a^2-r^2)\psi^2\lambda^2+2(W_1+W_4)\lambda^2-\frac{2W_1}{\lambda}. \tag{3.103}$$

We can now use the yield criteria defined in Section 2.2.6 to determine whether an applied deformation will lead to failure or not. We consider a twist Ψ applied to a cylinder that has already been stretched by a factor of $\lambda=1.1$, and calculate the critical value of twist Ψ_c required for the cylinder to yield, using the same constitutive parameters as in Section 3.7.2. By using the Hill criterion, defined in equation (2.45), we can vary the degree of anisotropy in the material strength to see if there is an impact on the failure behaviour under these loading conditions. We use the same material parameters as before, assuming again that $\sigma_z^Y=230$MPa. Figure 3.40 shows σ_H as a function of Ψ for $\gamma=1$, $\gamma=0.25$, and $\gamma=0.1$. According to the Hill yield criterion, the material will yield when $\sigma_H^2-1=0$.

As can be seen from Figure 3.40, the Hill stress σ_H is initially the same value for all three tests because, until a twist is applied, the Cauchy stress has only one non-zero component, σ_{zz}. When $\gamma=1$, we have an isotropic yield criterion with the same material strength in each direction, meaning that we must apply a large twist of 8.7 radians (over two full revolutions) to the top surface of the cylinder in order to build up enough stress

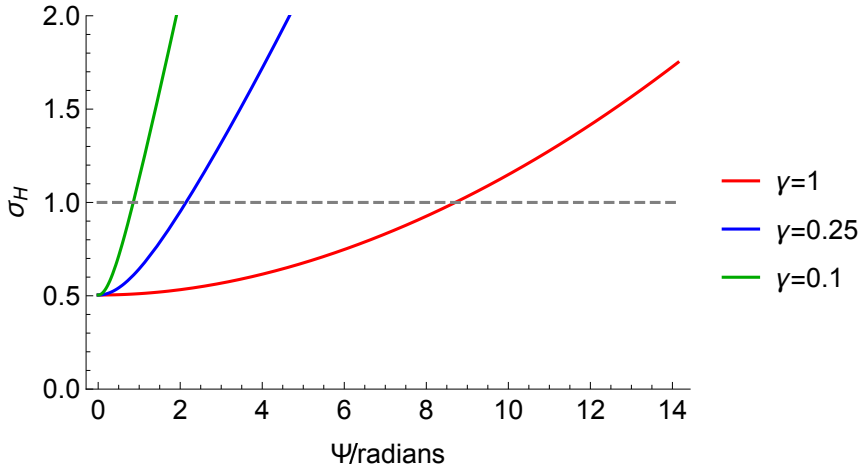

Figure 3.40: The square of the Hill stress as a function of twist in a cylindrical tendon. The red line corresponds to a material strength factor of $\gamma = 1$, meaning that the material strength is the same in all directions and the Hill stress reduces to the von Mises stress. Reducing the transverse strength of the tissue leads to the blue and green curves, which have material strength ratios of $\gamma = 0.25$, and $\gamma = 0.1$, respectively.

to achieve $\sigma_H^2 = 1$. For $\gamma = 0.1$, we find that the twist required to induce failure is 0.85 radians – a 90% decrease. We know that the stiffness of the matrix is $\sim 1,000,000$ times smaller than the stiffness of the collagen fibres [69], yet if the strength of the matrix is only 10 times smaller than that of the fibres (corresponding to $\gamma = 0.1$), the failure behaviour of the tissue changes significantly. To produce these results we used fibre and matrix stiffness values of 2.5GPa and 50MPa, respectively – a difference of only $50\times$. A more realistic stiffness ratio would counteract a large material strength ratio, because the lower relative stiffness in the matrix would prevent it from reaching its yield stress under normal conditions. To provide a more thorough evaluation of different yield criteria, we would need accurate measurements of material parameters, rather than order of magnitude estimations.

3.9 Discussion

In this chapter, we have performed finite element analysis on idealised models of tendons and ligaments in order to determine if commonly-followed modelling practices are reasonable, or if they should be reconsidered. The areas of interest highlighted by

a comprehensive literature review were: the constitutive model used to represent the tissue, the shape of the tendon/ligament, the fibre direction, and the choice of yield criterion. We assumed some generic parameter values, chosen to cover as many different tendon geometries as possible, and considered a simple deformation (uniaxial tension). We varied different geometric parameters in order to produce plots of average stress, maximum stress, and distributions of stress that can be compared quantitatively with one another and qualitatively with the literature, allowing for the critical evaluation of modelling practices.

3.9.1 Constitutive model and material parameters

Almost all of the constitutive models in the literature on finite element modelling of tendons and ligaments are phenomenological, meaning that they contain parameters that cannot all be measured experimentally (see Table 3.1). There are clearly some benefits to using a phenomenological model – namely that they are much simpler than their microstructurally-based counterparts and they are often already implemented within commercial finite element packages. This means that results can be produced quicker, and more complex geometries and deformations can be considered since the models are well-tested.

In this chapter we presented a model based solely on the tissue microstructure which is simple (it can be written down analytically), and contains only parameters that could, in principle, be measured experimentally[2]. To produce an initial set of results, we compared this crimped fibril model with the widely-used HGO model [47]. For the HGO model, we set the ground state shear modulus to $\mu = 1$MPa, and the remaining material parameters to $k_1 = 10$MPa and $k_2 = 10$. In reality, we would expect a much larger ratio between the stiffness of the matrix and the fibres [69], but for some geometries we encountered convergence issues if the stiffness ratio was too large. For the crimped fibril model we also used $\mu = 1$MPa. We set the collagen Young's modulus to $E = 10$MPa, and the fibril length distribution parameters were $a = 1.0$, $b = 1.05$, and $c = 1.025$. This value of E is much lower than is typically recorded in the literature (~ 0.8GPa [95]), but was chosen to match the value of k_1 in the HGO model. The distribution parameters were set based on the assumption that the linear region ends at around 5% strain. Both

[2]Chapter 4 contains more details on the feasibility of measuring these parameters.

models produced qualitatively similar results for all geometries, with the exception of the linearly tapered tendon with z-aligned fibres, which produced large stress concentrations around the smallest cross-section of the tendon or ligament when the HGO model was used.

The model used in this chapter was simple but contains more information about the microstructure than phenomenological models, meaning it could be used to predict how the tissue behaviour would change given sufficient microstructural information. Additionally, we can estimate the distribution parameters for different tissues based on available data without needing to perform tensile tests and fit to stress-strain data. A significant proportion of models we came across in our literature search assumed isotropy, despite the fibrous nature of soft tissue. Whilst this might provide a reasonable approximation for some tissues at small strains [96], we recommend against this choice for tendons and ligaments, given that their microstructure cannot be well-represented by an isotropic model, and because of the well-documented difference between their longitudinal and transverse mechanical properties [97, 98].

3.9.2 The effects of geometry

We first considered the base problem of a transversely isotropic, hyperelastic, right-circular cylinder subject to uniaxial extension. In this example, there is only one non-zero component of stress σ_{zz}, which is homogeneous throughout the cylinder. We opted to vary this geometry away from cylindrical so that it more closely resembled a tendon, and explore the effects this has on the mechanical response. We imposed a linear taper and an hour glass taper, and adjusted the cross-section to be elliptical. Throughout Section 3.6, we fixed the volume of the tissue so that we only studied the effects of redistributing the material into a different geometry. We determined that, with both the crimped fibril and HGO models, increasing the linear/hourglass taper resulted in higher peak stress and lower engineering stress. These variations in stress are due to the cross-sectional area changing through the length of the tendon. Where the cross-sectional area is smallest, the applied force is spread across a smaller area, leading to higher stresses. To maintain a constant volume, the cross-sectional area at the top and bottom must increase – leading to a decrease in stress. This increase in area towards the ends of the tendon/ligament may serve to reduce the stress experienced at the bone

insertion sites. We found that changing the cross-section to be elliptic had no effect on the stress distribution unless combined with an axially-varying geometry that produced a spatially-varying cross section.

3.9.3 Fibre direction

Perhaps the most significant findings from this chapter come from the fibre direction study. When assuming cylindrical geometry, we set the direction of the fibres to be equal to the longitudinal axis of the tendon/ligament. In this instance, they are also parallel to the outer curved boundary, but when we apply a transformation to the mesh, this is no longer the case. In Section 3.5.3, we proposed a fibre direction field which sought to rectify this issue, ensuring that at the edge of the tendon the fibres are parallel to the boundary, whilst in the centre they are aligned with the longitudinal axis. This is a subtle point (see Figure 3.1) which does not seem to be addressed in the literature. Several authors [74, 78, 77, 8], opt to use the local element geometry to ensure that the fibre direction follows the shape of the tendon when a realistic geometry is used, but we could not find an example where the fibre direction at the outer surface of the tendon is discussed.

For the initial tests we chose to compare two different fibre directions: z-aligned fibres (longitudinally aligned and parallel everywhere) and c-aligned fibres (contour-aligned, spatially dependent). Whilst the differences in the observed stresses for different geometries are easily predicted by carefully considering the geometry in question, the differences observed by changing the direction of the fibres are less obvious. We found that when the fibres are z-aligned, there is a stress concentration around the part of the tendon with the smallest cross-section. This region of high stress does not penetrate far into the tissue, instead forming a band of stress on the surface of the tendon. The relative magnitude of this stress concentration changes based on the geometry in question. For axisymmetric tendons, the stress is the same all the way round. For a tendon of constant width, such as the Achilles tendon, the bands appear only on the sides which vary in width, as can be seen in Figure 3.27. When we switch to c-aligned fibres, the stress concentrations are no longer present – we instead see a more even distribution of stress across the radius of the tendon, increasing in magnitude in the region with the smallest cross-section. When using realistic geometry meant to approximate

the Achilles tendon, we found that changing from z-aligned fibres to c-aligned fibres reduced the maximum value of stress in the direction of the fibres by 31%, whilst increasing the final engineering stress by 5%. For a geometry based on the ACL, the maximum stress in the direction of the fibres decreased by 33% when switching from z- to c-aligned fibres, whilst the final engineering stress increased by 10%. The effects are slightly smaller for the Achilles tendon because we assume it has a constant width, so the cross-sectional area varies less than in the ACL.

It is possible that these regions of high stress appear in the z-aligned fibre configuration because points at the edge of the tendon, above and below the mid-section, are attached to the ends of the tendon on one side and the curved outer boundary on the other. When a stretch is applied, the curved boundary is therefore subjected to forces in the vertical direction, culminating in a region of high tensile forces where the radius is at a minimum. In the c-aligned case, we do not see this stress concentration because most of the force is carried in the direction of the fibres, which follow the contours of the geometry and therefore do not expose any particular region to high tensile forces. This theory is supported by the distributions of u_z, the z-inhomogeneity presented in Figure 3.28 for the Achilles tendon and Figure 3.36 for the ACL. In these plots we see regions of the tissue at the edge of the boundary, above and below the midsection, being pulled in opposite directions – thereby contributing to the high tensile forces experienced at the centre of the tissue.

One motivation for considering c-aligned fibres is the existence of strong evidence [24, 23] suggesting that collagen fibrils are continuous throughout the length of the tendon (as discussed in Section 2.1.2). We also chose to explore the effects of a non-constant collagen volume fraction, deriving an expression (equation (3.75)) which ensures that in each tendon cross-section, there is a constant area of collagen, rather than a constant area fraction. We implemented this fibre configuration in the Achilles tendon and ACL geometries and found that the results were extremely similar to the c-aligned fibre with constant area fraction case. For the Achilles tendon, both the maximum stress in the direction of the fibres and the final engineering stress increased by 4%. For the ACL we observed a $\sim 1.8\%$ increase in the maximum stress in the direction of the fibres and a $\sim 1.5\%$ increase in the final engineering stress. The function we used for the spatially varying collagen area fraction ensures that collagen is conserved in each cross-section, but in doing so, led to a difference of $\sim 39\%$ in collagen density between

the centre and the insertion. This is significantly larger than the value reported by [89] *et al.*, who found a difference of only 9%. This may suggest that the small differences we observed in the stress distributions for the constant and non-constant area fraction configurations would be even smaller in reality.

3.9.4 Yield criteria

The von Mises stress is used extensively throughout the literature to indicate if a tendon or ligament will fail given some applied load. [75] determined that this measure is not appropriate for studying failure in soft tissues by comparing experimental data taken from porcine aorta with a finite element model which outputted the von Mises stress. This study was only conducted within a 2D model, however, so it was a further aim of this chapter to compare the suitability of the isotropic von Mises yield criterion within a 3D model of tendons/ligaments. For this study, we focussed on the Achilles tendon due to its simple structure compared with the intertwined bundles of the ACL. When using z-aligned fibres, we found that the likely regions of failure occurred at the outer edges of the midsection, in the same location as the stress concentrations were observed. In this instance, similar behaviour was observed for both isotropic and anisotropic yield criteria. For c-aligned fibres, both with constant and spatially-varying collagen area fractions, we found that under the same deformation and for the same material parameters, using an isotropic yield criterion did not predict yielding occurring in the tendon. When changing the material strength parameter to $\gamma = 0.1$, we found that in both of these fibre configurations, the Hill criterion indicated that yielding would occur. In this instance, we found concentrations of the Hill stress around the edges of the tendon on either side of the mid-section. This must be due to the in-plane deformation building up higher transverse and shear stresses which, with the weaker matrix, lead to yielding at a lower value of stretch.

Shim *et al.* [15] used finite element modelling to predict the failure location in a patient-specific model of the Achilles tendon. They used the von Mises stress for this and found that the tendon would fail around the edges of the smallest cross-section. In their work the authors do not mention the fibre direction. Assuming they set the fibre direction to coincide with to the longitudinal axis of the tendon, we can compare the results of our analysis with theirs. When we used z-aligned fibres, we determined that

both the von Mises and Hill yield criteria would predict failure in the same location as Shim *et al.* However, when we changed to the more realistic *c*-aligned fibres, we found that there was no longer a stress concentration in their proposed failure area. Instead, we found an even distribution of stress across the radius of the tendon, suggesting that the von Mises criterion would not favour the edge of the tendon over the centre. When applying a more realistic anisotropic yield criterion, we found that for a sufficiently weak matrix, failure would not initiate at the edge of the central section of the tendon, but at the edges closer to the ends. This is due to the radial contraction experienced by this part of the tendon, and the subsequent build up of transverse and shear stresses. Krueger *et al.* [99] performed a study of 303 patients with Achilles tendon rupture, determining that the location of failure was around 3–5cm from the distal (lower) insertion. Since the length of the Achilles tendon in our model is 17cm [91], this is consistent with our predictions in the *c*-aligned fibre case when the Hill criterion was used, as yielding was indicated around the upper/lower edges. It is important to note, however, that our idealised geometry will of course differ slightly from those studied by Krueger *et al*.

In this Chapter we used a single macroscopic yield criterion to predict failure in the tissue. Another approach would be to consider the matrix and fibre phases separately, and apply appropriate yield criteria to each of these. An isotropic yield criterion such as the von Mises criterion could be applied to the matrix phase, whilst a simple 1D criterion could be used to determine if the fibres would fail. This approach would simplify calculations and give us more information about the failure modes of the tissue, but would still suffer from the problems we found with the composite yield criteria, in that there is limited data available for the failure properties of the extra-collagenous matrix.

The prediction of failure in tendons and ligaments is one particularly useful application of mathematical modelling applied to soft tissue. As discussed in Chapter 1, tendon/ligament injuries can be debilitating, sometimes demanding surgical intervention and requiring months of rest. A thorough understanding of the conditions which lead to failure has the potential to help surgeons and clinicians design better procedures and treatment plans. However, it is clear from our finite element study that more experimental data is required before any reliable results can be produced. The lack of detailed information about the transverse stiffness and the material strength in each direction leads to wildly different results when yield criteria are used to predict failure location. For this reason, in the next Chapter, we seek to use a microstructural approach to study

failure in tendons and ligaments.

Chapter 4

A microstructural model of tendon failure

About

This chapter is a reproduction of an article published in the Journal of the Mechanical Behaviour of Biomedical Materials [100]. It was written by myself, Tom Shearer and Andrew L. Hazel. I conceived the initial idea behind the model, conducted the curve-fitting, and wrote the article. My co-authors and supervisors helped to direct the research, suggested modifications, confirmed and corrected derivations, and assisted in editing the paper for publication.

Abstract

Collagen fibrils are the most important structural component of tendons. Their crimped structure and parallel arrangement within the tendon lead to a distinctive non-linear stress-strain curve when a tendon is stretched. Microstructural models can be used to relate microscale collagen fibril mechanics to macroscale tendon mechanics, allowing us to identify the mechanisms behind each feature present in the stress-strain curve. Most models in the literature focus on the elastic behaviour of the tendon, and there are few which model beyond the elastic limit without introducing phenomenological parameters. We develop a model, built upon a collagen recruitment approach, that only contains microstructural parameters. We split the stress in the fibrils into elastic and

plastic parts, and assume that the fibril yield stretch and rupture stretch are each described by a distribution function, rather than being single-valued. By changing the shapes of the distributions and their regions of overlap, we can produce macroscale tendon stress-strain curves that generate the full range of features observed experimentally, including those that could not be explained using existing models. These features include second linear regions occurring after the tendon has yielded, and step-like failure behaviour present after the stress has peaked. When we compare with an existing model, we find that our model reduces the average root mean squared error from 4.53MPa to 2.29MPa, and the resulting parameter values are closer to those found experimentally. Since our model contains only parameters that have a direct physical interpretation, it can be used to predict how processes such as ageing, disease, and injury affect the mechanical behaviour of tendons, provided we can quantify the effects of these processes on the microstructure.

4.1 Introduction

Tendons are composed of a complex hierarchy of collagen-based components embedded within an extra-collagenous matrix. When modelling the mechanical response of tendons as they are stretched to failure, it is important to consider this complex microstructure and how it gives rise to the observed stress-strain behaviour illustrated in Figure 4.1. The macroscale tendon stress-strain curve can be split into four sections: I) the non-linear toe region, II) the linear region, III) the post-yield region, and IV) the macroscopic failure region. Existing microstructural models [101, 102] are able to capture this behaviour when it resembles the idealised case presented in Figure 4.1, but we will show that a significant proportion of observed stress-strain curves [20] contain features that cannot be explained using these models. These features include second linear regions (in region III) and step-like failure behaviour (in region IV), as shown in Figure 4.2. We therefore propose a new microstructural model, based on the response of individual collagen fibrils, which is capable of capturing this behaviour.

Collagen fibrils often form the basis of microstructural models because they are the smallest component of tendons for which we have reliable stress-strain data. Fibrils are crimped within the fascicle, and only become load-bearing once the tendon has been stretched enough to remove their crimp. Due to varying crimp between fibrils, the

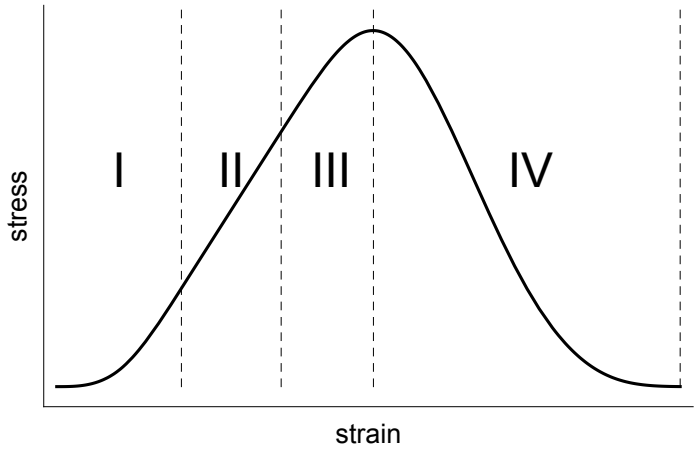

Figure 4.1: Idealised stress-strain behaviour of a tendon stretched to failure. Region I is the non-linear toe region, where collagen fibrils gradually become taut, increasing the overall tendon stiffness. Region II is the linear region, where all the fibrils are exhibiting a linearly elastic response. The end of region II is the macroscopic yield point, where yielding in the fibrils causes a reduction in gradient. Region III is the post-yield region, where fibrils begin to yield and fail. Region IV is the macroscopic failure region, where fibrils continue to fail and the whole tendon eventually ruptures.

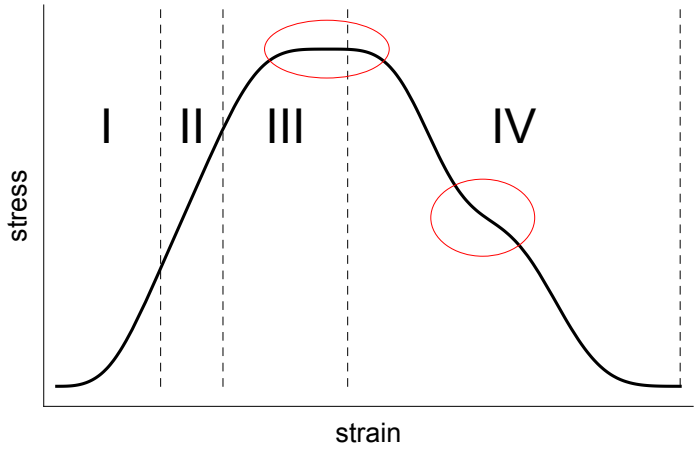

Figure 4.2: An idealised stress-strain curve demonstrating observed features (highlighted in red) which cannot be captured using existing models [101, 102]. Regions I and II are the same as in Figure 4.1, but the post-yield region (region III) shows a plateau instead of a well-defined peak. The macroscopic failure region (region IV) contains step-like failure behaviour, where the second derivative of the stress changes sign multiple times.

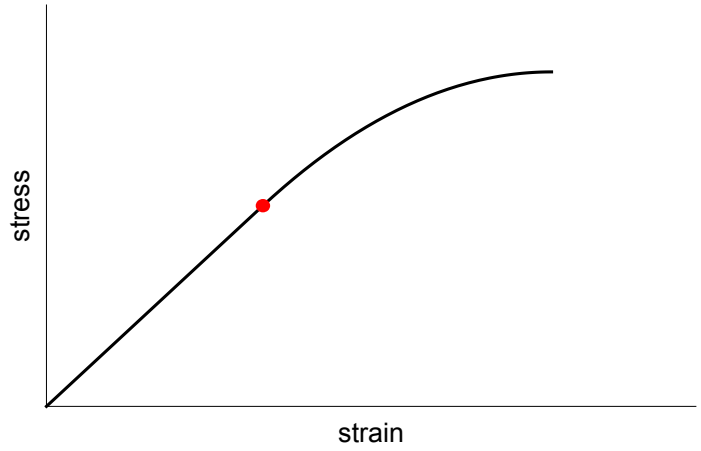

Figure 4.3: Idealised stress-strain behaviour of an individual collagen fibril stretched to failure. The fibril exhibits a linear response initially, before experiencing a decrease in gradient. Stretching beyond the linear region causes the fibril to become damaged [95], leading us to refer to the transition between linear and non-linear behaviour as the fibril yield stretch/strain, represented above by the red marker.

tendon initially exhibits a non-linear stress-strain response, as fibrils gradually become taut (region I). The tendon stiffness continues to increase until all of the fibrils are taut and we see a macroscale linear region (region II). Hijazi *et al.* [26] used scanning electron microscopy to show that stretching a tendon past the end of its linear region results in permanent damage on the fibril scale, suggesting that as we pass into the post-yield region (region III), fibrils themselves begin to yield. This is further supported by Zitnay *et al.* [103], who were able to detect damage at the molecular level in rat tail tendon fibrils, once the tendon had been stretched past its linear region. When the tendon reaches the macroscopic failure region (region IV), many of the fibrils have yielded, and some may have ruptured completely. Eventually all of the fibrils will rupture and the tendon will fail.

To build a microstructural model capable of describing the full range of tendon stress-strain behaviour observed in regions I–IV, we must look in more detail at the mechanical response of individual collagen fibrils. Many research groups have performed failure tests on isolated fibrils [95, 104, 105, 106, 107, 31], and whilst the reported material parameters show a large amount of variability, several trends still emerge. The fibril stress-strain response is most often described as linear initially, before becoming non-linear with a decreasing slope [95, 104, 105, 106, 107]. Van der Rijt *et al.* [108]

reported non-linear toe-regions for small strains (<4%), but claim that the stress-strain curve appears to be almost perfectly linear when the fibril is stretched further. For this reason, we make the assumption that the non-linear toe-region is negligible and that the initial phase of the fibril stress is linear. Figure 4.3 shows an idealised stress-strain curve for an isolated collagen fibril stretched to failure. We refer to the transition between the linear and non-linear behaviour as the fibril yield stretch/strain because there is evidence that stretching beyond this point leads to the accumulation of damage in the fibril [95]. The fibril yield strain can vary considerably between fibrils extracted from different sources. It has been reported to be approximately 6% strain in groups of rabbit patellar tendon fibrils [109], and 12% in single rat patellar tendon fibrils [105]. In fibrils extracted from sea cucumber dermis, the yield strain shows a large amount of variation, falling anywhere between 6–55% strain [104]. After yielding and experiencing a decrease in modulus, the fibrils rupture at anywhere from 7% strain [107] to over 100% strain [104]. We can conclude that there is not a single value of fibril yield/rupture strain, but rather there is a distribution of these strains present in any given tendon. We also know that the structure of fibrils in tendons is not uniform. For example, the fibril diameter follows a trimodal distribution [19]. It is possible that these mechanical and structural properties are related.

Ideally, a microstructural model will only contain parameters that can be measured experimentally. This allows the model to predict how certain processes, such as ageing, disease, or injury, may affect macroscale tendon behaviour, provided we know how the microstructural components are affected. For example, in the tendons of patients with classic Ehlers-Danlos syndrome (cEDS), the distribution of collagen fibril diameters is disrupted by a reduced quantity of collagen V [110], resulting in a diameter distribution with increased broadness and a larger mean diameter. A microstructural model that incorporates fibril diameter dependence could therefore be used to predict how the macroscale tendon properties would differ in comparison to a patient without cEDS. This approach would be particularly useful in instances where the effects of a disease on the mechanical properties of the tendon are not clear, as it would allow some properties, such as fibril diameter distribution, to be held constant whilst others, such as fibril density, are varied.

Continuum damage models are frequently used to predict the post-yield behaviour of tendons as they are stretched to failure, although they often contain parameters that

are not based on the microstructure. Natali *et al.* [111, 112] published a model where the strain energy function of the tendon is split into two parts associated with the matrix and fibrils, with each part being premultiplied by a damage function. The fibril damage function was derived by considering the number of fibrils which had yielded, assuming that the critical stretch required to remove crimp from the fibrils is normally distributed. The strain energy function used for the elastic regime, however, was phenomenological and not related to the mechanical behaviour of individual collagen fibrils. Similar models were published by by Rodríguez *et al.* [113] and Alastrué *et al.* [114], where the behaviour of collagen fibrils is described by models based on polymer mechanics. Whilst these models are capable of predicting the general behaviour of tendons stretched to failure, they are all phenomenological to some degree and, consequently, they contain parameters that cannot be directly measured. Other models have used a microstructural approach, but were limited to modelling regions I and II of the stress-strain curve [43, 51, 42].

Extending the widely used collagen recruitment model of Lanir [50], Hurschler *et al.* [101] developed an approach to model past the end of the linear region by including a yield criterion for the fibrils. By excluding both crimped and ruptured fibrils from stress calculations, Hurschler *et al.* [101] were able to get reasonable fits to data by assuming the fibril critical stretch follows a Weibull distribution. Hamedzadeh *et al.* [102] independently arrived at the same model, but extended its applicability by allowing the tissue to be compressible. They also showed how to model the effects of repeated overloading, demonstrating that it is possible to predict hysteresis whilst ignoring viscoelastic effects. The models of Hurschler *et al.* and Hamedzadeh *et al.*, which we shall refer to after their authors as the HLV and HGF models, respectively, show that it is possible to model whole tendon behaviour as it is stretched to failure by only focussing on the failure behaviour of the fibrils.

In this paper we use stress-strain data from Goh *et al.* [20] to demonstrate the need for a new microstructural model of tendon failure. This stress-strain data was collected from failure tests carried out on mouse tail tendon fascicles, extracted from mice of different ages. The authors also provide structural data in the form of fibril diameter distributions, making it possible to explore the relationship between some of the structural and mechanical properties of tendons. In Section 4.2, we attempt to fit a simplified version of the HLV and HGF models to this stress-strain data, showing that a significant

proportion (47%) of the data contains features that cannot be accounted for using these models.

In Section 4.3, we introduce a new model which is capable of capturing the range of stress-strain behaviour observed by Goh *et al*. [20]. By using distributions to represent the fibril yield and rupture stretches, we demonstrate the range of stress-strain behaviour that can be generated by varying the shape of the distributions, and their position relative to one another. The resulting model includes only parameters that can, in principle, be measured directly, and can fit a wider range of stress-strain data than previous models once appropriate distributions have been selected. In section 4.4, we present some example fits to datasets with the features illustrated in Figure 4.2. We show that the parameter values found through fitting are consistent with those found experimentally.

4.2 Fitting existing models to data

4.2.1 The elastic-rupture model

We first define the *elastic-rupture* (ER) model, which is equivalent to the HLV model [101]. We assume that the tendon is incompressible and composed of parallel, crimped fibres embedded within an isotropic matrix. We consider a simple uniaxial stretch λ applied to the tendon, in the direction of the fibres, leading to a homogeneous stress field throughout the tissue. Each fibril has a critical stretch λ_C, which is the tendon stretch required to remove the crimp from the fibril. Once a fibril is taut, it exhibits a linear elastic response until it ruptures after being stretched by a factor of λ_R. By using a probability distribution $\Lambda_C(\lambda_C)$ to represent the variation of crimp found throughout the tissue, we can compute the stress in the tendon.

The shear modulus of the matrix has been estimated to be on the order of 1kPa [69], which is $\sim$1,000,000 times smaller than the fibril Young's modulus [107]. Assuming the matrix Young's modulus is of a similar magnitude, it is negligible compared to that of the fibrils, and we therefore choose to ignore any contributions to the stress from the matrix. We further assume that the deformation occurs at a strain rate that minimizes hysteresis, allowing us to ignore viscoelastic effects. Under these assumptions, the stress

in the tendon is given by

$$\sigma_T^{ER}(\lambda) = \phi \int_1^{\infty} \sigma_f^{ER}(\lambda, \lambda_C, \lambda_R) \Lambda_C(\lambda_C) \mathrm{d}\lambda_C. \tag{4.1}$$

where ϕ is the collagen volume fraction, and σ_f^{ER} is the fibril stress. In the ER model, we define the fibril stress as

$$\sigma_f^{ER}(\lambda, \lambda_C, \lambda_R) = \begin{cases} 0, & \lambda < \lambda_C, \\ E\left(\dfrac{\lambda}{\lambda_C} - 1\right), & \lambda_C \leq \lambda < \lambda_C \lambda_R, \\ 0, & \lambda \geq \lambda_C \lambda_R, \end{cases} \tag{4.2}$$

where E is the fibril Young's modulus. For the models used in this paper, we adopt a naming approach based on the physical behaviour of the fibrils. In the ER model, the fibrils are linearly elastic until they have been stretched by a factor of λ_R, after which they rupture. Throughout this paper, we will assume that the fibril critical stretch follows a triangular distribution, as in Hamedzadeh *et al.* [102], defined by

$$\Lambda_C(\lambda_C) = \begin{cases} 0, & \lambda_C < a, \\ \dfrac{2(\lambda_C - a)}{(b-a)(c-a)}, & a \leq \lambda_C < c, \\ \dfrac{2(b - \lambda_C)}{(b-a)(b-c)}, & c \leq \lambda_C < b, \\ 0, & \lambda_C \geq b, \end{cases} \tag{4.3}$$

where a is the lower limit, b is the upper limit, and c is the mode of the distribution. We choose this form for the critical stretch distribution in order to simplify calculations, and because it allows us to write down an analytic expression for the tendon stress σ_T^{ER}. This expression can be found in B.1. Through careful choice of the parameters a, b, and c, a triangular distribution can be used to approximate other distributions which may be more realistic for collagen fibril properties, such as a Gaussian distribution.

4.2.2 Fitting approaches

We now fit the ER model to stress-strain data from Goh *et al*. [20]. This data was gathered from mouse tail tendon fascicles, extracted from mice of different ages, which were stretched to failure. Along with stress-strain data, Goh *et al*. provide the tendon yield strain for each test specimen, and the mean collagen volume fraction for each age group. The authors defined the tendon yield strain to be the point with maximum gradient between the origin and the peak stress, after fitting a fifth order polynomial to the data. We explored two different fitting approaches, one which uses the yield stretch provided by Goh *et al*., and one which does not. In both cases we use the collagen volume fraction found by Goh *et al*. These two approaches are outlined below:

> *Generic fitting approach*: Fitting for all of the model parameters: a, b, c, E, and λ_R, using the whole range of stress-strain data (regions I–IV).
>
> *Physically motivated fitting approach*: We assume $a = 1$, meaning that some of the fibrils immediately become taut upon stretching the tendon. We set the fibril rupture stretch λ_R to be equal to the macroscopic yield point, provided by Goh *et al*. We then fit for the parameters b, c, and E using the data in regions I and II.

In both fitting approaches, we use the analytic form of the tendon stress (see B.1) along with a non-linear least squares method to find the fitting parameters. When using the generic fitting approach, it was often the case that the parameter values found were unphysical. For example, in Figure 4.4, $b > \lambda_R$, suggesting that some fibrils begin to rupture before all of the fibrils have become taut. Whilst this seems reasonable if there is a large range of fibril critical stretch values, it contradicts evidence from Hijazi *et al*. [26], that damage only occurs in the fibrils once the entire tendon has been stretched beyond the end of the macroscopic linear region (i.e. $\lambda_R \geq b$). Furthermore, the generic fitting approach often leads to unrealistically high values of collagen fibril Young's modulus E. In Figure 4.4 we have $E = 6658$MPa, which is significantly larger than the highest value we could find in any paper where isolated collagen fibrils have been stretched to failure (1900 ± 500MPa for bovine achilles tendon fibrils under ambient conditions [115]). Using the generic fitting approach requires the entire range of stress-strain data (regions I–IV), in order to determine the parameters a, b, c, E, and λ_R. If we were only interested in modelling the elastic tendon behaviour (regions I–II), the

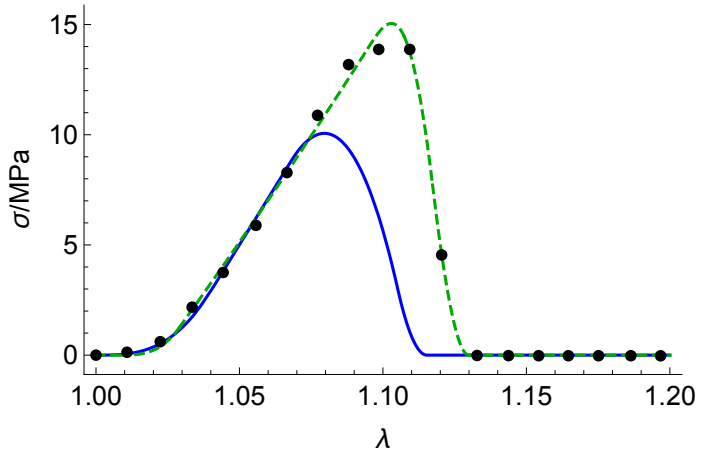

Figure 4.4: The ER model fitted to data from Goh *et al.* [20], using two different fitting approaches. The green dashed line was found using the generic fitting approach, whilst the solid blue line is the result of using the physically motivated fitting approach. The parameters from the generic fitting approach are: $E = 6658$MPa, $a = 1.008$, $b = 1.107$, $c = 1.095$, and $\lambda_R = 1.020$. The parameters for the physically motivated fitting approach are: $E = 386.7$MPa, $a = 1.0$, $b = 1.044$, $c = 1.035$, and $\lambda_R = 1.068$. The collagen volume fraction for both fittings is $\phi = 0.56$, which was taken from Goh *et al.* [20]. The root mean squared error for the generic approach is 0.264MPa, whilst for the physically motivated approach it is 3.43MPa. The generic fitting approach provides a superior fit, but at the cost of unphysical parameter values.

ER model could be modified by changing the fibril stress, defined in equation (4.2), so that the fibrils never rupture ($\lambda_R = \infty$). Since this elastic version of the model is defined by the same set of parameters, excluding λ_R, we should be able to determine the elastic parameters (a, b, c, and E) with the data from regions I and II alone. In other words, we should not need to stretch a tendon to failure in order to determine the parameters that define the pre-yield portion of the stress-strain curve. The physically motivated fitting approach ensures that $\lambda_R \geq b$, and that the elastic parameters are determined using the elastic part of the stress-strain data alone. Figure 4.4 shows an example of these two fitting approaches on the same set of data.

The restrictions placed on the model's parameters when using the physically motivated fitting approach mean that in the vast majority of cases, it is not possible to get a good fit to the data in regions III and IV. The magnitude of the post-yield stress is consistently underestimated, as can be seen in Figure 4.4, suggesting that there is something missing from the model. Although the ER model can provide a reasonable fit in

certain cases when the generic fitting approach is used, we instead choose to modify the model so that we can still use the physically motivated fitting approach. This ensures that all fitting parameters are realistic, and that the elastic parameters are consistent with the values we would find if the tendon was not stretched to failure.

4.2.3 Features that cannot be accounted for

The ER model is only capable of describing the mechanical response of tendons in the cases where the stress-strain curve looks similar to the idealised response illustrated in Figure 4.1. In the stress-strain data from Goh *et al*. [20], a significant proportion of the data contains features that cannot be captured using the ER model, even when the constitutive behaviour of the fibrils is adjusted to more closely resemble experimental data. In this section we describe these features, discuss their prevalence, and demonstrate why a new model is required to capture them. A summary of the information presented in this section, split according to the age of the mouse from which the fascicle was extracted, can be seen in Table B.1 of B.2.

4.2.3.1 Additional linear regions

The idealised stress-strain curve in Figure 4.1 contains one linear region, in the elastic part of the response. Some sets of stress-strain data from Goh *et al*. [20] also contain a second linear region, present after the tendon has yielded. The gradient of this second linear section can vary, but is always less than the gradient of the first linear section. In some cases we see a small decrease in gradient as the tendon yields and enters a second linear region, followed by a well-defined peak in the stress. In other cases, the gradient of the second linear region is close to zero, and the stress reaches a plateau rather than a well-defined peak.

To determine whether a stress-strain curve contains a second linear region, we first isolate the data points before the peak. We then interpolate the data using splines over 50 equally spaced points, and look for groups of at least 10 interpolated data points where the gradient does not vary by over 10% of the maximum global gradient. Using this approach we find that 86 of 260 sets of data ($\sim$33%) contain a second linear region.

Our analysis showed that the peak can vary dramatically in broadness. Data with well-defined peaks can often be fitted using the ER model, but when the peak is wider,

the ER model fails to capture the post-yield behaviour. This may be due to the fact that the ER model does not incorporate fibril plasticity, leading to an underestimation in the magnitude of the post-yield stresses at the tendon scale. The failings of the ER model are most apparent in the 33% of cases where there is a clear second linear region. Without adding fibril plasticity to the ER model, we cannot possibly achieve a plateau in the macroscale stress-strain curve.

4.2.3.2 Step-like failure behaviour

The second feature that cannot be accounted for using the ER model is step-like failure behaviour in the macroscopic failure region. In the idealised stress-strain curve presented in Figure 4.1, the gradient of the stress in region IV begins at zero, decreasing smoothly until it reaches a minimum value, before increasing back to zero. This behaviour can be described using the ER model. In the experimental data from Goh *et al*. [20], some of the stress-strain curves seem to show steps in this region, where the second derivative of the stress changes sign multiple times.

We classify a set of data as exhibiting step-like failure behaviour if there is at least one data point in region IV with a larger gradient than both of its neighbouring points. Using this criterion, we find that 54 of 260 sets of data ($\sim$21%) contain step-like failure behaviour. This is a significant proportion of the data, further supporting the need for an improved model.

4.3 The elastic-plastic-distribution model

4.3.1 General framework

By making biologically-motivated adjustments to the ER model, we can begin to account for the stress-strain features described in Section 4.2.3. The first of these is to modify the constitutive behaviour of the fibrils so that once they have been stretched by a factor of λ_Y, they yield and begin to undergo plastic deformation. The second is to introduce distributions for the fibril yield stretch λ_Y, and rupture stretch λ_R. We call the resulting model the *elastic-plastic-distribution* (EPD) model. In the EPD model, we

define the fibril stress to be

$$\sigma_f^{EPD}(\lambda,\lambda_C,\lambda_Y,\lambda_R) = \begin{cases} 0, & \lambda < \lambda_C, \\ E\left(\dfrac{\lambda}{\lambda_C} - 1\right), & \lambda_C \leq \lambda < \lambda_C\lambda_Y, \\ p(\lambda,\lambda_C,\lambda_Y,\lambda_R), & \lambda_C\lambda_Y \leq \lambda < \lambda_c\lambda_R, \\ 0, & \lambda \geq \lambda_C\lambda_R, \end{cases} \tag{4.4}$$

where $p(\lambda,\lambda_C,\lambda_Y,\lambda_R)$ is the plastic stress in a yielded fibril. Experimental evidence suggests that, when selecting a functional form for p, we should choose a "flat" function which has a lower gradient than the initial linear portion of the fibril stress. We believe that in instances where the macroscale tendon stress is displaying a broad/flattened peak, the majority of fibrils are also exhibiting flattened stress-strain behaviour.

We assume that the fibril critical stretch λ_C, yield stretch λ_Y, and rupture stretch λ_R, follow a multivariate distribution $\Lambda(\lambda_C,\lambda_Y,\lambda_R)$. We then find the stress in the tendon by integrating the fibril stress over this distribution,

$$\sigma_T^{EPD}(\lambda) = \phi \int_1^\infty \int_1^\infty \int_1^\infty \sigma_f^{EPD}(\lambda,\lambda_C,\lambda_Y,\lambda_R)\Lambda(\lambda_C,\lambda_Y,\lambda_R)\mathrm{d}\lambda_C\mathrm{d}\lambda_Y\mathrm{d}\lambda_R. \tag{4.5}$$

4.3.2 Simplifying assumptions

In order to demonstrate how the EPD model can be used to produce the range of macroscale stress-strain curves observed experimentally, we make two simplifying assumptions. Firstly, we assume that the fibrils are bilinear elasto-plastic, choosing the following form for p,

$$p(\lambda,\lambda_C,\lambda_Y,\lambda_R) = E(1-k)(\lambda_Y - 1) + Ek\left(\frac{\lambda}{\lambda_C} - 1\right), \tag{4.6}$$

where $k \in [0,1]$ is a factor describing the decrease in gradient after the fibril has yielded. Secondly, we assume that the critical, yield, and rupture stretches are independent of each other, so that the distribution $\Lambda(\lambda_C,\lambda_Y,\lambda_R)$ can be written as

$$\Lambda(\lambda_C,\lambda_Y,\lambda_R) = \Lambda_C(\lambda_C)\Lambda_Y(\lambda_Y)\Lambda_R(\lambda_R). \tag{4.7}$$

We further assume that $\Lambda_C(\lambda_C)$, $\Lambda_Y(\lambda_Y)$, and $\Lambda_R(\lambda_R)$ are all triangular distributions. By changing the values of the parameters defining the yield and rupture stretch distributions, we can control the width of the macroscale stress-strain curve in regions III and IV. This amount of control is not possible using the ER model, and is required in order to fit the range of data observed experimentally.

4.3.3 Marginal distributions

In the HGF model [102], the authors define a damage distribution by stretching the critical stretch distribution by a factor of λ_R, their single value of rupture stretch. This damage distribution describes the proportion of fibrils in the tendon that have failed for a given value of tendon stretch. We can also compute equivalent distributions for the yield and rupture stretch when we have distributions, rather than single values.

A fibril with critical stretch λ_C, and yield stretch λ_Y, will yield when the tendon stretch is equal to $\lambda = \lambda_C\lambda_Y$. We consider the joint distribution of critical stretch and yield stretch, and use this relation to define the following function

$$g(\lambda_C, \lambda) = \Lambda_C(\lambda_C)\Lambda_Y\left(\frac{\lambda}{\lambda_C}\right). \tag{4.8}$$

We then define $\overline{\Lambda_Y}(\lambda)$ as the marginal distribution found by integrating $g(\lambda_C, \lambda)$ with respect to λ_C,

$$\overline{\Lambda_Y}(\lambda) = \int_1^\infty g(\lambda_C, \lambda)\mathrm{d}\lambda_C = \int_1^\infty \lambda_C(\lambda_C)\Lambda_Y\left(\frac{\lambda}{\lambda_C}\right)\mathrm{d}\lambda_C. \tag{4.9}$$

We can follow a similar process in order to determine the marginal rupture distribution $\overline{\Lambda_R}(\lambda)$. The resulting distributions, once normalised, can be used to describe the proportion of fibrils that have yielded or ruptured for a given tendon stretch λ. Hamedzadeh *et al*. [102] show the tendon stress-strain curve obtained using their model when the damage distribution (marginal rupture distribution in our model) and critical stretch distribution overlap. If these distributions overlap, then the first fibril may fail before the last fibril becomes taut, a scenario we argued against when justifying the physically motivated fitting approach. It is possible, however, that the marginal *yield* distribution and the marginal rupture distribution can overlap in our model. As discussed in Section 4.1,

there is a large range of yield and rupture strain values reported in the literature, even for fibrils extracted from the same source. It is therefore possible that as a tendon is stretched to failure, some fibrils rupture before others have yielded.

4.3.4 Varying the stretch distributions

By varying the shape, position, and spread of the yield stretch and rupture stretch distributions, it is possible to produce macroscale stress-strain curves with the full range of features observed experimentally. Figure 4.5 shows the effects of varying the separation between the distributions, with all other parameters fixed. To produce this figure we used generic parameter values, varying only the mean rupture stretch, to demonstrate the effects this has on the macroscale tendon stress. Based on the limited data in the literature, any of these arrangements could be possible, and we provide a more detailed discussion about the possible values of the distribution parameters in Section 4.5.

When the distributions overlap, there is a well-defined peak with no second linear region. Increasing the separation between the yield and rupture distributions causes a plateau to appear in the macroscale stress-strain curve, for values of tendon stretch between the marginal distributions. In this region, when there is no overlap, all of the fibrils are deforming plastically. By choosing the constitutive behaviour of the fibrils to be bilinear elasto-plastic, this leads to a second linear region. The spread of the yield and rupture distributions also affects the macroscale stress-strain curve, as can be seen in Figures 4.6 and 4.7.

In Figure 4.6 we see that changing the spread of the rupture distribution, whilst holding the yield distribution constant, changes the shape of the peak and increases the width of region IV. As the spread increases, there is more overlap, and the peak becomes sharper. This is due to the fibrils rupturing sooner, and therefore no longer contributing to the macroscale stress. Figure 4.5 shows how translating the rupture stretch distribution to the right can result in a significant increase to the magnitude of the post-yield stress. Varying the spread of the rupture distribution, however, changes the shape of the peak without causing a significant increase in the magnitude of the stress in region III.

The results displayed in Figure 4.7 demonstrate how the macroscale stress-strain

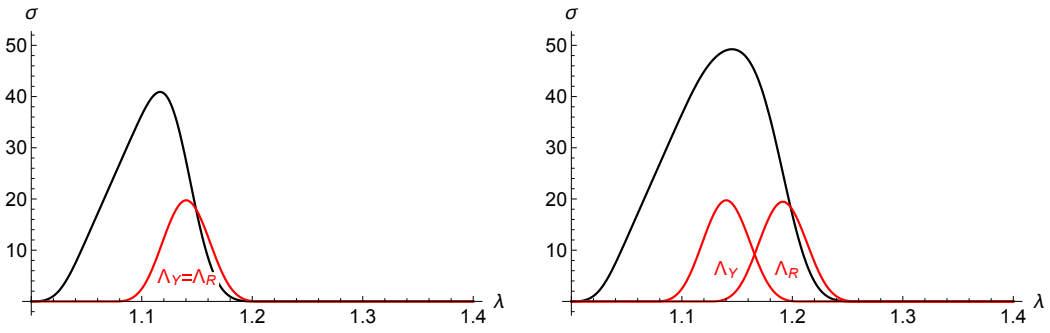

(a) $\mu_R - \mu_Y = 0$ (b) $\mu_R - \mu_Y = 0.05$

(c) $\mu_R - \mu_Y = 0.1$ (d) $\mu_R - \mu_Y = 0.15$

Figure 4.5: The effects of varying the separation between the yield stretch and rupture stretch distributions, on the macroscale stress-strain curve. The yield distribution was fixed and the position of the rupture distribution was varied. Symmetric triangular distributions were used for all of the stretch distributions. The black curves show the stress in the tendon, whilst the red curves show the marginal yield and rupture distributions used to generate them. The mean value of the (original, not marginal) yield and rupture distributions are μ_Y and μ_R, respectively. μ_Y remains fixed at $\mu_Y = 1.1125$. We choose a value of $k = 0$ to illustrate how varying the separation between the two distributions can lead to a plateau in the tendon stress.

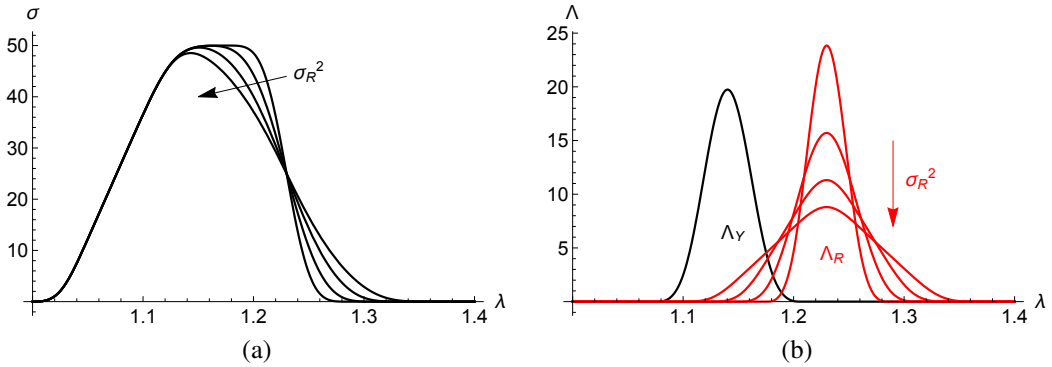

Figure 4.6: When the mean values of the yield and rupture distributions are held constant and the variance of the rupture distribution is increased, the macroscale stress strain-curve changes as shown in (a). The corresponding marginal distributions are shown in (b). The arrows point in the direction of increasing variance, σ_R^2.

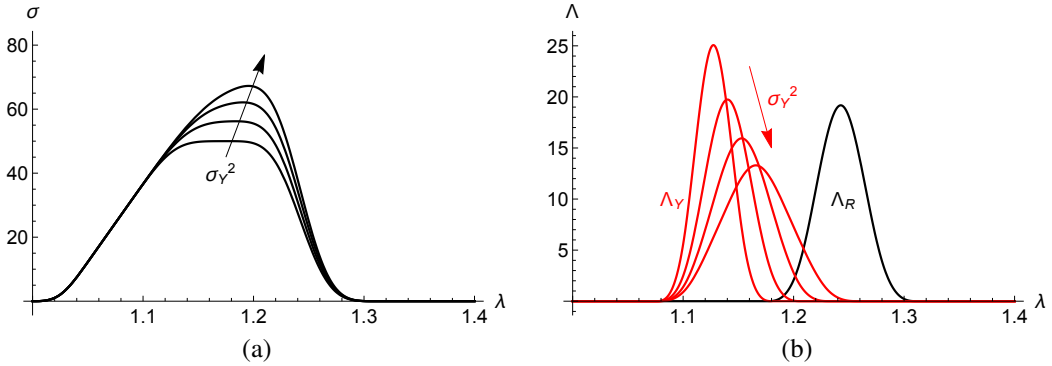

Figure 4.7: Shown in (a) is the macroscale stress-strain curve obtained when the rupture stretch distribution is held constant and the variance of the yield stretch distribution is changed. The marginal distributions that generate these curves can be seen in (b). The variance is changed by increasing the upper limit of the distribution, whilst holding the lower limit constant. This is done so that the macroscale yield point remains constant in all of the stress-strain curves in (a). The arrows point in the direction of increasing variance, σ_Y^2.

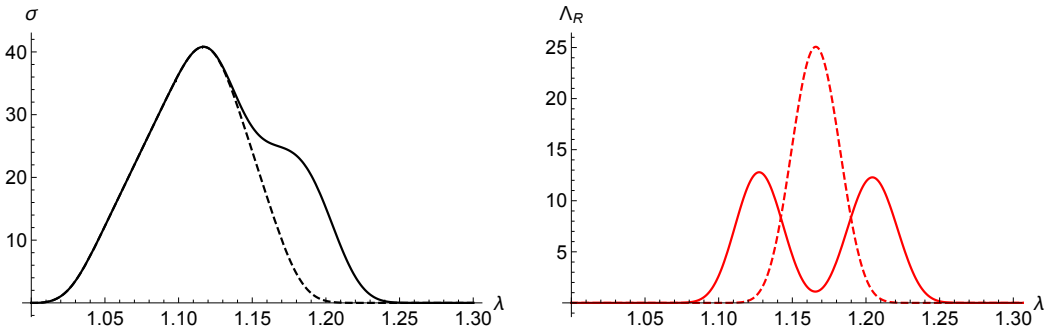

Figure 4.8: Changing the fibril rupture distribution from unimodal to bimodal causes the stress in the macroscopic failure region to exhibit step-like behaviour. Shown in (a) is the macroscopic stress-strain curve generated from the rupture distributions whose marginal counterparts are shown in (b). Dashed and solid lines correspond to the unimodal distribution and bimodal distribution, respectively. In the bimodal case, fewer fibrils are rupturing when the tissue stretch λ falls between the modes, leading to a region in the macroscale stress-strain curve where the gradient becomes less steep.

curve is affected when the rupture distribution is fixed and the spread of the yield distribution is varied. In doing this we choose to fix the lower bound of the yield distribution so that the macroscale yield point remains the same. By increasing the spread in the yield distribution, we are delaying the yielding of fibrils, causing an increase in the magnitude of the post-yield stress. We also increase the amount of overlap between the marginal distributions, leading to a sharper peak. The stress in the macroscopic failure region (region IV) is not affected by these changes.

The distributions used to generate the stress-strain curves in Figures 4.5, 4.6, and 4.7 have all been unimodal triangular distributions. Allowing the rupture distribution to be multimodal causes the stress in the macroscopic failure region to exhibit step-like behaviour, as shown in Figure 4.8. Whilst there is no direct evidence that collagen fibril failure strain follows a multimodal distribution, we consider this case because it is a simple way to introduce step-like failure behaviour on the macroscale. See Section 4.5 for a full discussion on alternative ways to account for step-like failure behaviour.

When the rupture distribution used to generate the macroscale stress-strain curve is multimodal and has a sufficiently wide gap between the peaks, we see a corresponding region of the stress-strain curve where the gradient of the stress becomes less steep. As the tendon stretch approaches the next peak, the gradient of the stress becomes more

negative again as fibrils continue to fail and no longer contribute to the total stress. This leads to step-like behaviour, as shown in Figure 4.8.

4.4 Fitting the improved model to data

In this section we use the physically motivated fitting approach to show that the EPD model can be used to generate realistic stress-strain curves, with microstructural parameters that fall within the range of values observed experimentally.

We continue to use the stress-strain data from Goh *et al*. [20], using the following process to find appropriate parameter values:

1. We assume the fibril critical stretch λ_C follows a triangular distribution, defined by the parameters a, b, and c, as described in equation (4.3).

2. We use the method outlined in Section 4.2 to determine the elastic parameters and use the macroscopic yield point provided by Goh *et al* [20] to separate the data into elastic and inelastic parts. To reduce the number of fitting parameters we assume that the critical stretch distribution is symmetric so that $c = (a+b)/2$.

3. We assume that both the fibril yield stretch λ_Y, and fibril rupture stretch λ_R, follow symmetric triangular distributions, given by Λ_Y and Λ_R, respectively. There is not enough data available to make an informed decision about the forms of either of these distributions. Triangular distributions are used to simplify calculations and to ensure that Λ_Y and Λ_R have finite support. Additionally, a symmetric triangular distribution can be defined using just the range of observed values, making the resulting fitting parameters easy to compare with the limited data available in the literature.

4. We label the yield stretch distribution parameters as a_Y and b_Y, and the rupture stretch distribution parameters as a_R and b_R.

5. We then use a nonlinear least squares method (`scipy.optimize.curve_fit` in Python 3) to determine the five remaining parameters: a_Y, b_Y, a_R, b_R, and k.

6. If the algorithm described in section 4.2.3.2 detects step-like failure behaviour, we replace the rupture stretch distribution with a bimodal triangular distribution, defined by

$$\Lambda_R^{\text{bimodal}}(\lambda_R) = \frac{1}{1+W}(\Lambda_R^{(1)}(\lambda_R) + W\Lambda_R^{(2)}(\lambda_R)), \tag{4.10}$$

where $\Lambda_R^{(1)}$ and $\Lambda_R^{(2)}$ are unimodal triangular distributions, as defined in equation (4.3), with distribution parameters ($a_R^{(1)}$, $b_R^{(1)}$, $c_R^{(1)}$) and ($a_R^{(2)}$, $b_R^{(2)}$, $c_R^{(2)}$), respectively. The relative weighting between the two modes is given by W. In these instances we assume $\Lambda_R^{(1)}$ and $\Lambda_R^{(2)}$ are both symmetric and fit for $a_R^{(1)}$, $b_R^{(1)}$, $a_R^{(2)}$, $b_R^{(2)}$, and W.

We also fitted the ER model to the same data, assuming that the fibril critical stretch followed a symmetric triangular distribution to ensure a fair comparison. We adopted the generic fitting approach for the ER model to get the best fit possible, but in many cases this still provided a poor fit because the ER model cannot generate plateaus or step-like failure behaviour. Of the 262 sets of stress-strain data from Goh *et al*., we excluded 39 (15%) because they contained fewer data points than fitting parameters. The remaining fits had an average root mean squared error (RMSE) of 2.29MPa compared to 4.53MPa for the ER model. Using the EPD model reduced the RMSE in 183 of the non-excluded cases (82%). In instances where step-like failure behaviour was detected, changing from a unimodal to a bimodal rupture stretch distribution reduced the average RMSE of those tests from 2.19MPa to 1.50MPa. Histograms of the fitting parameters can be seen in B.3. When defining the physically motivated fitting approach in section 4.2.2, we state that the macroscopic yield point should correspond to the point at which the first fibril yields. In the EPD model this is equivalent to setting a_Y equal to the macroscopic yield point. Whilst this can provide a good fit in some cases, we opted to remove this restriction when fitting both models to the whole set of data, because in some cases it is too restrictive. This could be an indication that some fibrils begin to yield before others have become taut, or that the yield point determined by Goh *et al*. is inaccurate.

Figure 4.9 shows an example of the EPD model fitted to data from Goh *et al*. [20], containing a plateau region rather than a well-defined peak. We can achieve a good fit to this data by assuming the yield stretch and rupture stretch follow symmetric triangular distributions. The RMSE for the fit is 1.13MPa, compared with 7.39MPa for

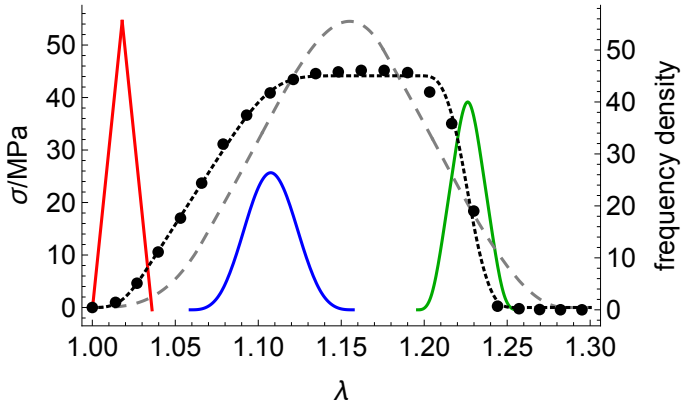

Figure 4.9: The black dashed line shows the EPD model, with bilinear elastoplastic fibrils, fitted to data from Goh *et al* [20]. The critical stretch distribution, shown in red, was found by fitting the purely elastic model to the data in regions I and II. The blue and green curves show the marginal yield and rupture distributions, defined in equation (4.9). The right hand axis refers to these distributions. The critical, yield, and rupture stretch were assumed to follow symmetric triangular distributions. The macroscale stress-strain curve contains a plateau region which could not be accounted for using previous models. The crimp distribution parameters are $a = 1.0$ and $b = 1.036$. The fibril Young's modulus is $E = 895.7$MPa, and $k = 0$. The yield stretch distribution parameters are $a_Y = 1.059$ and $b_Y = 1.117$. The rupture stretch distribution parameters are $a_R = 1.196$ and $b_R = 1.213$. The RMSE for the fit is 1.13MPa. The grey dashed line shows the ER model fitted to the same data, where the RMSE is 7.39MPa.

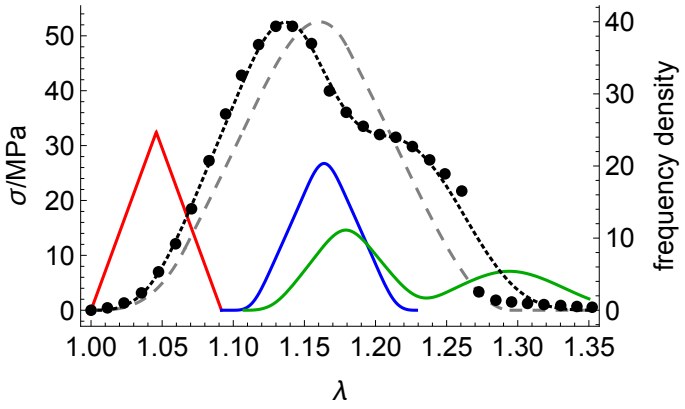

Figure 4.10: The EPD model fitted to data from Goh *et al.* [20] containing a well-defined peak and step-like failure behaviour. The black dashed line shows the stress, whilst the red, blue, and green curves show the critical stretch, the marginal yield stretch, and the marginal rupture stretch distributions, respectively. A bimodal rupture distribution is able to capture the step-like failure behaviour observed at the tendon level. The crimp distribution parameters are $a = 1.0$ and $b = 1.081$. The fibril Young's modulus is $E = 1160$MPa, and $k = 0.349$. The yield stretch distribution parameters are $a_Y = 1.088$ and $b_Y = 1.112$. The rupture stretch distribution parameters are $a_R^{(1)} = 1.095$, $b_R^{(1)} = 1.131$, $a_R^{(2)} = 1.159$, and $b_R^{(2)} = 1.263$. The second peak of the rupture stretch distribution has a weighting of $W = 0.72$ relative to the first peak. The RMSE for the fit is 2.21MPa.The grey dashed line shows the ER model fitted to the same data, with a RMSE of 7.57MPa.

the ER model using the generic fitting approach. The error is considerably larger for the ER model because it cannot generate a second linear region. The initial non-linear toe region covers the support of the critical stretch distribution and the region between the supports of the critical stretch and marginal yield distributions corresponds to the macroscale linear region. Fibrils begin to yield when the tendon stretch falls within the support of the marginal yield distribution, leading to a decrease in the gradient of the stress. There is then a region before fibrils start failing, where all fibrils are deforming plastically. The stress then decreases to zero as fibrils begin to rupture.

Figure 4.10 shows a second set of data from Goh *et al.* [20], containing a well-defined peak along with step-like failure behaviour in region IV. The same fitting procedure was followed, but using a bimodal triangular distribution for the rupture stretch, in order to capture the step-like failure behaviour in region IV. The root mean squared error for the fit in Figure 4.10 is 2.21MPa, compared with 7.57MPa for the ER model

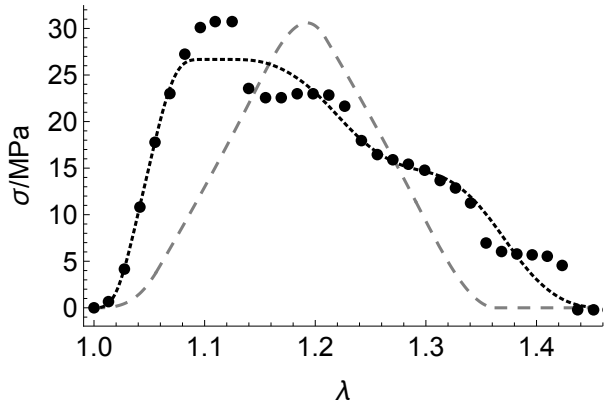

Figure 4.11: The black dashed line shows the EPD model, with a bimodal rupture stretch distribution, fitted to data from Goh *et al* [20] (RMSE = 2.02MPa). The data contains more than one step in the macroscopic failure region and so it would require more than two modes in the rupture stretch distribution to capture this behaviour. The grey dashed line shows the ER model fitted to the same data (RMSE = 8.51MPa).

using the generic fitting approach. The resulting yield and rupture stretch distributions overlap, leading to a well-defined peak in the stress. This also means that there is a range of tendon stretch values λ, where there simultaneously exists undamaged, yielded, and ruptured fibrils. The stress in the tendon begins to decrease as fibrils rupture, and once the tendon stretch passes into the region between the rupture distribution peaks, the gradient of the stress becomes less negative, because fewer fibrils are rupturing. As λ passes into the second rupture distribution peak, the gradient becomes more negative, and the tendon eventually fails.

Although the EPD model presents a good fit in the majority of cases, it can sometimes fail to capture the observed behaviour. Figures 4.11 and 4.12 show two examples where this is the case.

The EPD model fails to capture the multiple steps present in the stress-strain data shown in Figure 4.11. These could be captured by using a rupture stretch distribution with more than two modes, but due to the low number of data points we chose not to attempt this. In Figure 4.12, the assumption that the critical stretch distribution is symmetric leads to a poor fit in regions I and II, causing the peak stress to be underestimated.

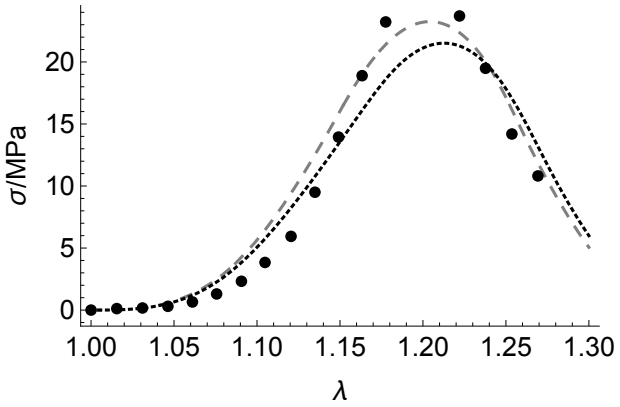

Figure 4.12: The black dashed line shows the EPD model fitted to data from Goh *et al* [20] (RMSE = 2.45MPa). Assuming that the critical stretch distribution is symmetric leads to a poor overall fit. The grey dashed line shows the ER model fitted to the same data (RMSE = 1.84MPa).

4.5 Discussion

We have shown that we can construct a mathematical model of tendon failure by splitting the fibril stress into elastic and plastic parts, and allowing the fibril yield stretch and rupture stretches to follow distributions, rather than being single-valued. When a single value of these parameters is used, as in the ER model, the plastic behaviour of the tendon is determined entirely by the critical stretch distribution. In at least 47% of cases (see B.2) it is not possible to get a good fit using the ER model because the stress-strain data contains a second linear region, step-like failure behaviour, or both. The EPD model provides a microstructural explanation for these features, and has the additional benefit of only including parameters that can be measured directly.

The introduction of a plastic stress function to the fibril constitutive behaviour is not new. Hamedzadeh *et al*. [102] define their model in terms of a general fibril constitutive behaviour, thereby encompassing that part of the EPD model. The key difference in our approach is with the use of distributions to describe the fibril yield stretch and rupture stretch. Whilst modifying the fibril stress to become more flat can generate second linear regions, it is not enough to produce the range of behaviour observed by Goh *et al* [20]. We must have a combination of both flattening fibril stress and a distribution of fibril yield stretch in order to capture all observed behaviour in region III. Without a distribution of yield stretch, the transition between a first and second linear region

will be fixed by the fibril crimp distribution, meaning that sets of data with a narrow region I but a wide region III cannot be fitted using the model. Without a distribution of fibril rupture stretch, we cannot produce step-like failure behaviour at the tendon scale without also incorporating it at the fibril scale. Failure tests carried out on individual collagen fibrils show that this would not be realistic.

By using distributions to represent the failure properties of collagen fibrils, we are able to encapsulate the variation observed between the stress-strain curves of individual fibrils. There is not enough data available to study specific forms of these distributions, but we know that they will be heavily influenced by the structural properties of the fibrils. For example, changes in cross-link density synonymous with tendon maturation have been shown to alter the mechanical properties of fibrils, affecting the yield stretch in particular [116]. To model such a change using the framework introduced in this paper, we would simply feed this change into the yield stretch distribution, which would alter the whole tendon stress-strain curve.

Our model does not contain any direct dependence on collagen fibril diameter, but there is some evidence to suggest that step-like failure could be due to the tendon possessing a multimodal distribution of fibril diameters. Yamamoto *et al.* [107] were able to determine a relationship between collagen fibril diameter and failure strain, for fibrils extracted from mouse tail tendons. Fibrils with a larger diameter seemed to fail at larger strains. It could be the case that in stress-strain data where we see step-like failure behaviour, there is a multimodal distribution of collagen fibril diameters, leading to a multimodal distribution of fibril failure strain. Although it is common to see multimodal fibril diameter distributions in tendons [19], the diameter distributions recorded by Goh *et al.* [20] seem to be unimodal for mice in the age groups where step-like failure is most commonly observed (see Table B.1 in B.2). Whilst this seems to contradict the theory that the step-like behaviour is due to groups of fibrils with different diameters failing in turn, it does not rule it out. The diameter distributions recorded by Goh *et al.* [20] were found by taking the average across multiple fascicles, whilst the stress-strain data itself is from single fascicles. We cannot find the diameter distribution of a tendon and then stretch it to failure, as these are both destructive procedures. It remains plausible that the fascicles whose stress-strain curves contained step-like failure behaviour possess a multimodal diameter distribution, but that the average diameter distribution for that age group appears to be unimodal. Another possibility is that the relationship

between collagen fibril diameter and rupture stretch is more complex than the linear relationship suggested by Yamamoto *et al.* [107], somehow causing the unimodal diamater distribution to result in a multimodal rupture stretch distribution. It could also be the case that it is the distribution of rupture stretch that gives rise to the distribution of diameters as the tendon matures, i.e. the fibrils may grow differently depending on their initial mechanical properties.

Using a multimodal distribution to represent the fibril failure strain is not the only way to account for the step-like failure behaviour observed at the macroscale. We can also produce this behaviour by having a multimodal distribution of critical stretch, representing a scenario where different fibre bundles have a different mean length. Step-like failure behaviour would therefore occur when these bundles fail at different times during a deformation. One attractive part of this approach is that it ties together the behaviour in every region of the tendon stress-strain curve, reducing the freedom brought about by the large number of parameters in the EPD model. However, if a tendon possesses a multimodal distribution of critical stretch, we would expect to see multiple distinct linear regions with increasing gradient before the tendon yields. We do not see this in any of the stress-strain data from Goh *et al.* [20] where step-like failure is observed. It would still be possible to produce step-like failure behaviour with a single linear elastic region if there was a large amount of overlap between the yield stretch distribution and the additional modes of the critical stretch distribution. This would mean that fibrils in the first group begin to yield before fibrils in the other groups become taut, preventing additional linear regions and leading to steps in the macroscopic failure region. Fitting such a model to the data from Goh *et al.* would prove difficult in cases where all three distributions overlap due to the low number of data points in some of the tests.

Step-like failure could also be due to technical issues with the experiment, rather than due to the tissue microstructure itself. Clamping apparatus could cause fibre bundles to become differentially loaded, leading to some failing before others. Whilst this may have had an impact on the stress-strain data we were using, we chose to explore how this behaviour could arise from physiological differences in the tendon microstructure. In the absence of strong evidence for either the rupture stretch distribution or the critical stretch distribution being multimodal, we chose to do our fitting with the former for the sake of simplicity.

In order to get a sense of how our model compares with the ER model, we fitted both

models to data from Goh *et al.* [20]. We chose to follow the physically motivated fitting approach for the EPD model, but opted to leave the lower bound of the yield stretch distribution a_Y as a fitting parameter, rather than setting it equal to the macroscopic yield point. Whilst this can lead to cases where some fibrils yield before others have become taut, the macroscopic yield data provided by Goh *et al.* proved to be too restrictive when used to fix the value of a_Y. To get a fair comparison between the EPD and ER models, we used symmetric triangular critical stretch distributions throughout, assuming that the lower bound of the critical stretch distribution a_C is equal to 1. This helped us to reduce the number of fitting parameters and lower the risk of overfitting. We found that in 82% of cases the EPD model provided a better fit than the ER model. In many of the remaining cases, the overall quality of the fit was hindered by a poor fit in the elastic region. This was often due to the assumption of symmetry in the critical stretch distribution, leading to an underestimation of the modulus, and a poor fit overall. The average RMSE reduced from 4.50MPa using the ER model, to 2.29MPa with the EPD model. The value of the plasticity parameter k found through fitting often did not change from its initial value of $k = 0$, suggesting that either it is not always that important to the model, or it cannot be determined from tendon stress-strain data alone.

It is difficult to judge whether the distributions used to generate the stress-strain curves in Figures 4.9 and 4.10 are realistic because in all the references we could find, only a small number of collagen fibrils are stretched to failure. Liu *et al.* [105] state that for fibrils extracted from rat patellar tendons, the yield point falls between 10% and 20% strain. In Figure 4.9, the lower and upper bounds of the yield distribution are at 6% strain and 12% strain, respectively, whilst in Figure 4.10, the yield distribution is bounded between 8% and 14% strain. The histograms of a_Y and b_Y presented in Figure B.1 in B.3 paint a similar picture: the mean values of a_Y and b_Y are 1.06 (6% strain) and 1.12 (12% strain), respectively. Despite the data from Goh *et al.* [20] and Liu *et al.* [105] coming from different sources, we believe that the similarities between the range of fibril yield strains observed experimentally, and the values we have found through our fitting, suggest that the EPD model is suitable for modelling the post-yield tendon behaviour (region III).

Fibrils tested by Liu *et al.* [105] failed between 35% and 107% strain. Yamamoto *et al.* quote a failure strain of 34 ± 11% for fibrils extracted from mouse tail tendons [106], and in a follow up paper, a range of 7–81% [107]. All of these ranges exceed the

upper bounds of the rupture distributions presented in Figures 4.9 and 4.10, which are 23% and 25%, respectively. In fact, over all the fittings, the mean value of b_R was found to be 1.22 (22% strain). Liu *et al.* [105] claim that because the tendon failure strain is typically much lower than the fibril rupture strain, there must be another component that is limiting the strength of the tendon, such as proteoglycans. We believe there are several reasons why the fibril rupture strain appears to be much larger than the tendon failure strain. Firstly, in tests carried out on individual collagen fibrils, the sections of fibril stretched to failure are much shorter than the entire length of the fibril. The fibrils tested by Yamamoto *et al.* [107] had a length of 19–64μm, and whilst reliable data on the length of mouse tail tendon fibrils is not available, fibrils have been traced along the entire length (125μm) of the mouse stapedius tendon [23]. If tail tendon fibrils are at least as long as those found in the stapedius tendon, then we can assume the sections tested by Yamamoto *et al.* were also significantly shorter than the total length of the fibril. Baldwin *et al.* [117] provide evidence that collagen fibrils, extracted from bovine tail, possess regions of mechanical susceptibility, due to a variation in structure along the length of the fibril. If fibrils are continuous throughout the length of the tendon, then the strength of the tendon will be limited by the strength of the weakest parts of its fibrils. By only testing small sections of fibrils to failure, rather than entire fibrils, these weakest sections are likely to be missed. This would lead to an overestimation of the fibril strength, potentially having a large effect on the perceived failure strain of collagen fibrils, depending on the frequency and strength of the regions of mechanical susceptibility. This idea is supported by evidence from Svensson *et al.* [118], who found that the failure strain of longer sections of fibril ($>$100μm) extracted from rat tail tendons was around 9%, prompting them to come to similar conclusions. This is closer to the values we found through fitting, but still exceeded the failure strain of the whole tendon, which was found to be around 5%. Secondly, it is possible that fibrils are subjected to inhomogeneous strains within the tendon. This could be due to the geometry of the tendon, or because the mechanical properties of the fibrils vary through the length of the tendon. An inhomogeneous strain applied to a fibril could cause it to rupture at a lower value of end-to-end strain than it would otherwise rupture at, outside of the tendon. Although some of the fibril failure strains reported in the literature [104, 107] exceed the upper bounds of the rupture distributions used to generate the stress-strain curves in this paper, the quality of fit achieved demonstrates that the EPD model is still useful for

modelling failure in tendons.

Throughout this paper we make a number of simplifying assumptions that may have a significant effect on its performance when it is used to model more complex deformations. We assume that fibrils are continuous and that damage on the macroscale occurs when the fibrils themselves become damaged. Whilst this approach is able to capture many of the stress-strain features observed experimentally, it may be necessary to extend the model to include interfibrillar sliding in order to fully capture all of the observed post-yield behaviour. There is some evidence that fibrils are discontinuous throughout the length of tendons [119, 120, 32], and if the length of a fibril is shorter than some critical length [25], slippage between the fibril and the matrix will occur before the fibril itself can yield. Szczesny *et al.* [27, 28] have shown that models based on this approach can be used to recreate the post-yield behaviour of tendons, getting good fits to experimental data. On the other hand, Craig *et al.* [22] provide evidence that collagen fibrils in rat tail tendons are at least as long as the critical length required for fibrils to be structurally continuous.

The stress-strain curves of fibrils extracted from energy storing tendons have been shown to include an additional region of strain-stiffening, not present in the response of fibrils from positional tendons [31, 121]. The inclusion of interfibrillar sliding may be necessary in order to relate this behaviour to the macroscale tendon response. As imaging techniques improve and we get a better sense of the true length distribution of collagen fibrils, we will understand more about the mechanisms that lead to tendon failure. It may be possible in future to develop a failure model based on fibril length distribution, where fibrils below the critical length will slip, and those above the critical length will yield.

There are several other simplifications we make that can be easily included when the model presented in this paper is used within a finite strain formulation. These include contributions to the stress from the extra-collagenous matrix, and the effects of fibre orientation. In the model presented by Hamedzadeh *et al.* [102], the authors compute the stress in a way that allows them to incorporate a distribution of fibre orientation and a matrix term. A similar approach could be used to make our model more realistic, where the stress in the direction of the fibres is described using the the expression in equation (4.5), with additional structural information imposed on top.

4.6 Addendum

This section is an addendum to the published work presented within this chapter, and seeks to provide an additional explanation for the stress-strain features observed in the data collected by Goh et al. [20]. In developing the EPD model, we sought a simple constitutive explanation to the wide range of failure behaviour observed experimentally, and we found that we were able to capture this behaviour by adapting existing elastic models to incorporate distributions of fibril failure properties. However, we fail to consider a number of important effects observed in fracture mechanics which could also explain these features, and which would need to be carefully considered when applying the EPD model to more complex deformations. First is the concept of strain localisation. In our continuum model of soft tissue there is no inherent length scale, whereas in real materials, failure will typically occur within a finite volume defined by some internal length scale [122]. As a tendon is stretched, the specific regions which fail first will be determined by inhomogeneities in the microstructure or the stress field (as a result of the geometry or the applied deformation). This is in contrast to our proposed model where, in the 1D case, since both the material properties and stress concentration are homogeneous, failure occurs simultaneously at all points in the tissue. After failure has been initiated in a small region of the tissue, the force being carried by the now ruptured fibrils must be transferred to the surrounding tissue, further increasing the risk of failure in adjacent fibrils. This could lead to a cascading effect, where groups of fibrils rupture as a crack propagates through the tissue. The step-like failure behaviour observed by Goh et al. [20] could be attributed to such an event, rather than being the result of a statistical distribution of fibril failure properties. Additionally, strain localisation could result in a jump in global strain whilst the engineering stress remains roughly constant because most of the material is undamaged. This could potentially lead to a plateau region in the stress-strain curve without the need for the entire tissue to be undergoing plastic deformation at the same point in time.

Another explanation for the plateaus observed in the stress-strain curve could come from the cross-link density of the tendon. In Section 2.1.2.2, cross-linking was introduced and a paper by Puxkandl et al. was discussed [32]. In this paper, it was found that exposing rats to BAPN, a lysyl oxidase inhibiting drug, reduced the density of enzymatic cross-links in their tail tendons, and the resulting stress-strain curves appeared to

have plateau regions. It is therefore possible that the plateau regions observed by Goh et al. [20] were the result of a reduced density of cross-links between collagen molecules.

Chapter 5

Conclusion

The aim of this thesis was to establish if modelling assumptions commonly applied to models of tendons and ligaments are appropriate, or if they need to be reconsidered. When conducting finite element modelling of tendons/ligaments, there are many decisions that one must make. The choice of constitutive model, geometry, fibre direction, the degree of anisotropy, and the stress measure used to represent the solution all have the potential to affect the predictions of the model. Our comparisons between a phenomenological and microstructural constitutive model show that, provided the model incorporates the appropriate degree of anisotropy, there is little qualitative difference between the two approaches. However, microstructural models should be preferred because they contain more information about the microstructure, along with measurable parameters that can be compared with existing experimental data. We found that the fibre direction is extremely important, and failure to properly consider the direction of fibres at the surface of the tendon can lead to stress concentrations which are not present when a more realistic fibre orientation is used. Finally, we discussed the use of the isotropic von Mises stress, showing that it produces different results to stress measures derived from anisotropic yield criteria.

After considering the applicability of isotropic and anisotropic yield criteria to soft tissue, we applied a simple 1D yield criterion to the individual collagen fibrils, and from this, derived an expression for the stress in the tissue as a whole. The resulting model incorporated distributions of fibril failure properties and was able to provide a good fit to experimental data, with microstructural parameters that fell within the range of values

found in the literature. This model, however, was only applied to a deformation in 1D.

There are many ways in which our work could be extended, but perhaps the most obvious would be to apply the constitutive model derived in Chapter 4 to a finite element model. This would allow us to judge the new model in a more complex 3D deformation, rather than just the 1D deformation considered within Chapter 4, and compare with stress-based yield criteria. We made attempts at this but were unable to successfully implement our model within non-cylindrical geometries. This may be because we assumed that a material described by this constitutive model would be hyperelastic, but that the microstructural failure model resulted in a non-convex strain energy function. It would also be beneficial to see a comparison between our idealised geometry and a geometry based on 3D scans of real tendons/ligaments. This would allow us to ensure that our results are not exclusive to the specific geometry we tested.

We believe that the work presented in this thesis has achieved many of the goals that we initially set out to achieve. We have produced results that could have an impact on future finite element models of tendons and ligaments, particularly when it comes to fibre direction. Additionally, the microstructural model we present in Chapter 4 provides a good foundation for future models which can be extended to 3D and used in more complex deformations. We sought to emphasise how microstructural models provide more useful information than phenomenological models, because their parameters are based on the underlying biology. We believe that we have achieved this by always relating the macroscale mechanical behaviour to the microstructure. However, because of the ambitious nature of our initial goals, there are certain places where we fell short. In particular, we only considered simple deformations. If we had applied more realistic boundary conditions to the tendons/ligaments in our finite element models, we may have learned more about the validity of the underlying assumptions.

Bibliography

[1] Pekka Kannus. Structure of the tendon connective tissue. *Scandinavian journal of medicine & science in sports*, 10(6):312–320, 2000.

[2] Chavaunne T Thorpe and Hazel RC Screen. Tendon structure and composition. *Metabolic influences on risk for tendon disorders*, pages 3–10, 2016.

[3] J Kastelic, I Palley, and E Baer. A structural mechanical model for tendon crimping. *Journal of biomechanics*, 13(10):887–893, 1980.

[4] Itai Gans, Julia S Retzky, Lynne C Jones, and Miho J Tanaka. Epidemiology of recurrent anterior cruciate ligament injuries in national collegiate athletic association sports: the injury surveillance program, 2004-2014. *Orthopaedic journal of sports medicine*, 6(6):2325967118777823, 2018.

[5] David J Biau, Caroline Tournoux, Sandrine Katsahian, Peter Schranz, and Rémy Nizard. Acl reconstruction: a meta-analysis of functional scores. *Clinical Orthopaedics and Related Research®*, 458:180–187, 2007.

[6] K Markatos, MK Kaseta, SN Lallos, DS Korres, and N Efstathopoulos. The anatomy of the acl and its importance in acl reconstruction. *European Journal of Orthopaedic Surgery & Traumatology*, 23(7):747–752, 2013.

[7] Jeremy Suggs, Conrad Wang, and Guoan Li. The effect of graft stiffness on knee joint biomechanics after acl reconstruction—-a 3d computational simulation. *Clinical biomechanics*, 18(1):35–43, 2003.

[8] Robert W Westermann, Brian R Wolf, and Jacob M Elkins. Effect of acl reconstruction graft size on simulated lachman testing: a finite element analysis. *The Iowa orthopaedic journal*, 33:70, 2013.

[9] Hamid Naghibi, Dennis Janssen, Tony Van Tienen, Sebastiaan Van de Groes, Ton Van de Boogaard, and Nico Verdonschot. A novel approach for optimal graft positioning and tensioning in anterior cruciate ligament reconstructive surgery based on the finite element modeling technique. *The knee*, 27(2):384–396, 2020.

[10] Thomas Young. *On the functions of the heart and arteries*. Print. W. Bulmer, 1809.

[11] Wei-qiu Chen. The renaissance of continuum mechanics. *Journal of Zhejiang University SCIENCE A*, 15(4):231–240, 2014.

[12] Peter Fratzl. Cellulose and collagen: from fibres to tissues. *Current opinion in colloid & interface science*, 8(1):32–39, 2003.

[13] YC Fung. Elasticity of soft tissues in simple elongation. *American Journal of Physiology-Legacy Content*, 213(6):1532–1544, 1967.

[14] Dominique P Pioletti, L Rakotomanana, JF Benvenuti, and PF Leyvraz. Finite element model of the human anterior cruciate ligament. pages 561–568, 2020.

[15] Vickie B Shim, Justin W Fernandez, Prasad B Gamage, Camille Regnery, David W Smith, Bruce S Gardiner, David G Lloyd, and Thor F Besier. Subject-specific finite element analysis to characterize the influence of geometry and material properties in achilles tendon rupture. *Journal of biomechanics*, 47(15):3598–3604, 2014.

[16] Peter Fratzl. Collagen: structure and mechanics, an introduction. In *Collagen*, pages 1–13. Springer, 2008.

[17] Yuan-cheng Fung. *Biomechanics: mechanical properties of living tissues*. Springer Science & Business Media, 2013.

[18] DAD Parry, GRG Barnes, and AS Craig. A comparison of the size distribution of collagen fibrils in connective tissues as a function of age and a possible relation between fibril size distribution and mechanical properties. *Proceedings of the Royal Society of London. Series B. Biological Sciences*, 203(1152):305–321, 1978.

[19] Joan Chang, Richa Garva, Adam Pickard, Ching-Yan Chloé Yeung, Venkatesh Mallikarjun, Joe Swift, David F Holmes, Ben Calverley, Yinhui Lu, Antony Adamson, et al. Circadian control of the secretory pathway maintains collagen homeostasis. *Nature cell biology*, 22(1):74–86, 2020.

[20] Kheng Lim Goh, David F Holmes, Yin Hui Lu, Karl E Kadler, and Peter P Purslow. Age-related dataset on the mechanical properties and collagen fibril structure of tendons from a murine model. *Scientific data*, 5(1):1–13, 2018.

[21] Kheng Lim Goh, DF Holmes, Yinhui Lu, Peter P Purslow, KE Kadler, Daniel Bechet, and Timothy James Wess. Bimodal collagen fibril diameter distributions direct age-related variations in tendon resilience and resistance to rupture. *Journal of applied physiology*, 113(6):878–888, 2012.

[22] Alan S Craig, Mervyn J Birtles, James F Conway, and David AD Parry. An estimate of the mean length of collagen fibrils in rat tail-tendon as a function of age. *Connective tissue research*, 19(1):51–62, 1989.

[23] Rene B Svensson, Andreas Herchenhan, Tobias Starborg, Michael Larsen, Karl E Kadler, Klaus Qvortrup, and S Peter Magnusson. Evidence of structurally continuous collagen fibrils in tendons. *Acta Biomaterialia*, 50:293–301, 2017.

[24] Paolo P Provenzano and Ray Vanderby Jr. Collagen fibril morphology and organization: implications for force transmission in ligament and tendon. *Matrix Biology*, 25(2):71–84, 2006.

[25] Bhagwan D Agarwal, Lawrence J Broutman, and K Chandrashekhara. *Analysis and performance of fiber composites*. John Wiley & Sons, 2017.

[26] Khaled M Hijazi, Kathy L Singfield, and Samuel P Veres. Ultrastructural response of tendon to excessive level or duration of tensile load supports that collagen fibrils are mechanically continuous. *Journal of the mechanical behavior of biomedical materials*, 97:30–40, 2019.

[27] Spencer E Szczesny and Dawn M Elliott. Interfibrillar shear stress is the loading mechanism of collagen fibrils in tendon. *Acta biomaterialia*, 10(6):2582–2590, 2014.

[28] Spencer E Szczesny and Dawn M Elliott. Incorporating plasticity of the interfibrillar matrix in shear lag models is necessary to replicate the multiscale mechanics of tendon fascicles. *Journal of the mechanical behavior of biomedical materials*, 40:325–338, 2014.

[29] Spencer E Szczesny, Kristen L Fetchko, George R Dodge, and Dawn M Elliott. Evidence that interfibrillar load transfer in tendon is supported by small diameter fibrils and not extrafibrillar tissue components. *Journal of Orthopaedic Research*, 35(10):2127–2134, 2017.

[30] Jeremy D Eekhoff, Fei Fang, and Spencer P Lake. Multiscale mechanical effects of native collagen cross-linking in tendon. *Connective tissue research*, 59(5):410–422, 2018.

[31] Rene B Svensson, Hindrik Mulder, Vuokko Kovanen, and S Peter Magnusson. Fracture mechanics of collagen fibrils: influence of natural cross-links. *Biophysical journal*, 104(11):2476–2484, 2013.

[32] R Puxkandl, I Zizak, O Paris, J Keckes, W Tesch, S Bernstorff, P Purslow, and P Fratzl. Viscoelastic properties of collagen: synchrotron radiation investigations and structural model. *Philosophical Transactions of the Royal Society of London. Series B: Biological Sciences*, 357(1418):191–197, 2002.

[33] Lena Kjellén and Ulf Lindahl. Proteoglycans: structures and interactions. *Annual review of biochemistry*, 60(1):443–475, 1991.

[34] Robert G Spiro. Glycoproteins. *Advances in protein chemistry*, 27:349–467, 1973.

[35] Michael J Sherratt. Tissue elasticity and the ageing elastic fibre. *Age*, 31(4):305–325, 2009.

[36] Jay D Humphrey. Continuum biomechanics of soft biological tissues. *Proceedings of the Royal Society of London. Series A: Mathematical, Physical and Engineering Sciences*, 459(2029):3–46, 2003.

[37] Anthony James Merrill Spencer. *Continuum mechanics*. Courier Corporation, 2004.

[38] Albert Edward Green and Wolfgang Zerna. *Theoretical elasticity*. Courier Corporation, 1992.

[39] Anthony James Merrill Spencer. *Continuum mechanics*, chapter 10, pages 135–152. Courier Corporation, 2004.

[40] WF Decraemer, MA Maes, VJ Vanhuyse, and P Vanpeperstraete. A non-linear viscoelastic constitutive equation for soft biological tissues, based upon a structural model. *Journal of biomechanics*, 13(7):559–564, 1980.

[41] G Limbert, Mark Taylor, and J Middleton. Three-dimensional finite element modelling of the human acl: simulation of passive knee flexion with a stressed and stress-free acl. *Journal of biomechanics*, 37(11):1723–1731, 2004.

[42] Tom Shearer, William J Parnell, Barbara Lynch, Hazel RC Screen, and I David Abrahams. A recruitment model of tendon viscoelasticity that incorporates fibril creep and explains strain-dependent relaxation. *Journal of Biomechanical Engineering*, 142(7):071003, 2020.

[43] Tom Shearer. A new strain energy function for the hyperelastic modelling of ligaments and tendons based on fascicle microstructure. *Journal of biomechanics*, 48(2):290–297, 2015.

[44] A Wineman. Nonlinear viscoelastic solids—a review. *Mathematics and mechanics of solids*, 14(3):300–366, 2009.

[45] Haojie Mao. Modeling the head for impact scenarios. In *Basic Finite Element Method as Applied to Injury Biomechanics*, pages 469–502. Elsevier, 2018.

[46] Ronald S Rivlin. Large elastic deformations of isotropic materials iv. further developments of the general theory. *Philosophical transactions of the royal society of London. Series A, Mathematical and physical sciences*, 241(835):379–397, 1948.

[47] Gerhard A Holzapfel, Thomas C Gasser, and Ray W Ogden. A new constitutive framework for arterial wall mechanics and a comparative study of material models. *Journal of elasticity and the physical science of solids*, 61(1):1–48, 2000.

[48] DE Beskos and JT Jenkins. A mechanical model for mammalian tendon. *Journal of Applied Mechanics*, 42(4):755, 1975.

[49] Maria Comninou and Ioannis Vassiliou Yannas. Dependence of stress-strain nonlinearity of connective tissues on the geometry of collagen fibres. *Journal of Biomechanics*, 9(7):427–433, 1976.

[50] Yan Lanir. Constitutive equations for fibrous connective tissues. *Journal of biomechanics*, 16(1):1–12, 1983.

[51] Tom Shearer. A new strain energy function for modelling ligaments and tendons whose fascicles have a helical arrangement of fibrils. *Journal of biomechanics*, 48(12):3017–3025, 2015.

[52] Jacob Lubliner. *Plasticity theory*. Courier Corporation, 2008.

[53] Rodney Hill. *The mathematical theory of plasticity*, volume 11. Oxford university press, 1998.

[54] Tim Bevan, Nadege Merabet, Jack Hornsby, Paul N Watton, and Mark S Thompson. A biomechanical model for fibril recruitment: evaluation in tendons and arteries. *Journal of Biomechanics*, 74:192–196, 2018.

[55] James Haughton, Simon Cotter, William J Parnell, and Tom Shearer. Bayesian inference on a microstructural, hyperelastic model of tendon deformation. *arXiv preprint arXiv:2201.04865*, 2022.

[56] Namrata Gundiah, Mark B Ratcliffe, and Lisa A Pruitt. Determination of strain energy function for arterial elastin: Experiments using histology and mechanical tests. *Journal of biomechanics*, 40(3):586–594, 2007.

[57] CK Chua, SH Teh, and RKL Gay. Rapid prototyping versus virtual prototyping in product design and manufacturing. *The international journal of advanced manufacturing technology*, 15(8):597–603, 1999.

[58] Lefteris Benos, Dimitar Stanev, Leonidas Spyrou, Konstantinos Moustakas, and Dimitrios E Tsaopoulos. A review on finite element modeling and simulation of

the anterior cruciate ligament reconstruction. *Frontiers in Bioengineering and Biotechnology*, 8, 2020.

[59] Fabio Galbusera, Maren Freutel, Lutz Dürselen, Marta D'Aiuto, Davide Croce, Tomaso Villa, Valerio Sansone, and Bernardo Innocenti. Material models and properties in the finite element analysis of knee ligaments: a literature review. *Frontiers in bioengineering and biotechnology*, 2:54, 2014.

[60] DR Veronda and RA Westmann. Mechanical characterization of skin—finite deformations. *Journal of biomechanics*, 3(1):111–124, 1970.

[61] FA Bandak, RE Tannous, and T Toridis. On the development of an osseo-ligamentous finite element model of the human ankle joint. *International Journal of Solids and Structures*, 38(10-13):1681–1697, 2001.

[62] Yuhua Song, Richard E Debski, Volker Musahl, Maribeth Thomas, and Savio L-Y Woo. A three-dimensional finite element model of the human anterior cruciate ligament: a computational analysis with experimental validation. *Journal of biomechanics*, 37(3):383–390, 2004.

[63] Hirotaka Sano, Ikuko Wakabayashi, and Eiji Itoi. Stress distribution in the supraspinatus tendon with partial-thickness tears: an analysis using two-dimensional finite element model. *Journal of shoulder and elbow surgery*, 15(1):100–105, 2006.

[64] Yaodong Gu, Jianshe Li, XJ Ren, and MJ Lake. Finite element analysis of achilles tendon in jumping phase. In *ISBS-Conference Proceedings Archive*, 2007.

[65] YD Gu, JS Li, MJ Lake, XJ Ren, and YJ Zeng. The mechanical response of achilles tendon during different kinds of sports. *Communications in numerical methods in engineering*, 24(12):2077–2085, 2008.

[66] Hirotaka Sano, Taku Hatta, Nobuyuki Yamamoto, and Eiji Itoi. Stress distribution within rotator cuff tendons with a crescent-shaped and an l-shaped tear. *The American journal of sports medicine*, 41(10):2262–2269, 2013.

[67] Răzvan Aniţaş and DO Lucaciu. Finite element analysis of the achilles tendon while running. *Acta Marisiensis-Seria Medica*, 59(1):8–11, 2013.

[68] Colin R Firminger, Ifaz T Haider, Olivia L Bruce, John W Wannop, Darren J Stefanyshyn, and W Brent Edwards. Are subject-specific models necessary to predict patellar tendon fatigue life? a finite element modelling study. *Computer Methods in Biomechanics and Biomedical Engineering*, pages 1–11, 2021.

[69] Tom Shearer, Chavaunne T Thorpe, and Hazel RC Screen. The relative compliance of energy-storing tendons may be due to the helical fibril arrangement of their fascicles. *Journal of the Royal Society Interface*, 14(133):20170261, 2017.

[70] Pathan Farha, DA Mahajan, and SY Gajjal. Finite element analysis of anterior cruiciate ligaments. *International Journal of Research and Scientific Innovation*, Volume I Issue VII:213–218.

[71] Richard E Debski, Jeffrey A Weiss, William J Newman, Susan M Moore, and Patrick J McMahon. Stress and strain in the anterior band of the inferior glenohumeral ligament during a simulated clinical examination. *Journal of shoulder and elbow surgery*, 14(1):S24–S31, 2005.

[72] Mitchell S Hortin and Anton E Bowden. Quantitative comparison of ligament formulation and pre-strain in finite element analysis of the human lumbar spine. *Computer methods in biomechanics and biomedical engineering*, 19(14):1505–1518, 2016.

[73] Wencke Hansen, Vickie B Shim, Steven Obst, David G Lloyd, Richard Newsham-West, and Rod S Barrett. Achilles tendon stress is more sensitive to subject-specific geometry than subject-specific material properties: a finite element analysis. *Journal of biomechanics*, 56:26–31, 2017.

[74] JMT Penrose, GM Holt, M Beaugonin, and DR Hose. Development of an accurate three-dimensional finite element knee model. *Computer methods in biomechanics and biomedical engineering*, 5(4):291–300, 2002.

[75] Christopher E Korenczuk, Lauren E Votava, Rohit Y Dhume, Shannen B Kizilski, George E Brown, Rahul Narain, and Victor H Barocas. Isotropic failure

criteria are not appropriate for anisotropic fibrous biological tissues. *Journal of biomechanical engineering*, 139(7), 2017.

[76] E Pena, B Calvo, MA Martinez, and M Doblare. A three-dimensional finite element analysis of the combined behavior of ligaments and menisci in the healthy human knee joint. *Journal of biomechanics*, 39(9):1686–1701, 2006.

[77] John C Gardiner and Jeffrey A Weiss. Subject-specific finite element analysis of the human medial collateral ligament during valgus knee loading. *Journal of orthopaedic research*, 21(6):1098–1106, 2003.

[78] Mark A Baldwin, Chadd Clary, Lorin P Maletsky, and Paul J Rullkoetter. Verification of predicted specimen-specific natural and implanted patellofemoral kinematics during simulated deep knee bend. *Journal of biomechanics*, 42(14):2341–2348, 2009.

[79] Shunji Hirokawa and Reiji Tsuruno. Three-dimensional deformation and stress distribution in an analytical/computational model of the anterior cruciate ligament. *Journal of biomechanics*, 33(9):1069–1077, 2000.

[80] Jeffrey A Weiss, Bradley N Maker, and Sanjay Govindjee. Finite element implementation of incompressible, transversely isotropic hyperelasticity. *Computer methods in applied mechanics and engineering*, 135(1-2):107–128, 1996.

[81] RS Marlow. A general first-invariant hyperelastic constitutive model. *Constitutive Models for Rubber*, pages 157–160, 2003.

[82] Cornelius Lanczos. *The variational principles of mechanics*. University of Toronto press, 2020.

[83] J Tinsley Oden. *Finite elements of nonlinear continua*. Courier Corporation, 2006.

[84] Matthias Heil and Andrew L Hazel. oomph-lib–an object-oriented multi-physics finite-element library. In *Fluid-structure interaction*, pages 19–49. Springer, 2006.

[85] Murat Kaya, Nazım Karahan, and Barış Yılmaz. Tendon structure and classification. In Hasan Sözen, editor, *Tendons*, chapter 2. IntechOpen, Rijeka, 2019.

[86] L-H Yahia and G Drouin. Microscopical investigation of canine anterior cruciate ligament and patellar tendon: collagen fascicle morphology and architecture. *Journal of orthopaedic research*, 7(2):243–251, 1989.

[87] Kuo Kan Liang. Efficient conversion from rotating matrix to rotation axis and angle by extending rodrigues' formula. *arXiv preprint arXiv:1810.02999*, 2018.

[88] Jae Ho Yoo, Seung Rim Yi, and Jin Hong Kim. The geometry of patella and patellar tendon measured on knee mri. *Surgical and radiologic anatomy*, 29(8):623–628, 2007.

[89] TJA Mommersteeg, L Blankevoort, RJGM Kooloos, JCM Hendriks, JMG Kauer, and R Huiskes. Nonuniform distribution of collagen density in human knee ligaments. *Journal of orthopaedic research*, 12(2):238–245, 1994.

[90] Mahmut Nedim Doral, Mahbub Alam, Murat Bozkurt, Egemen Turhan, Ozgür Ahmet Atay, Gürhan Dönmez, and Nicola Maffulli. Functional anatomy of the achilles tendon. *Knee Surgery, Sports Traumatology, Arthroscopy*, 18(5):638–643, 2010.

[91] Neil D Reeves and Glen Cooper. Is human achilles tendon deformation greater in regions where cross-sectional area is smaller? *Journal of Experimental Biology*, 220(9):1634–1642, 2017.

[92] Scott G McLean and Mélanie L Beaulieu. Complex integrative morphological and mechanical contributions to acl injury risk. *Exercise and sport sciences reviews*, 38(4):192–200, 2010.

[93] Wolf Petersen and Thore Zantop. Anatomy of the anterior cruciate ligament with regard to its two bundles. *Clinical Orthopaedics and Related Research®*, 454:35–47, 2007.

[94] Yoshimasa Fujimaki, Eric Thorhauer, Yusuke Sasaki, Patrick Smolinski, Scott Tashman, and Freddie H Fu. Quantitative in situ analysis of the anterior cruciate

ligament: length, midsubstance cross-sectional area, and insertion site areas. *The American journal of sports medicine*, 44(1):118–125, 2016.

[95] Zhilei L Shen, Mohammad Reza Dodge, Harold Kahn, Roberto Ballarini, and Steven J Eppell. Stress-strain experiments on individual collagen fibrils. *Biophysical journal*, 95(8):3956–3963, 2008.

[96] Evgeny Gladilin, Stefan Zachow, Peter Deuflhard, and H-C Hege. A biomechanical model for soft tissue simulation in craniofacial surgery. In *Proceedings International Workshop on Medical Imaging and Augmented Reality*, pages 137–141. IEEE, 2001.

[97] Brent K Hoffmeister, Scott M Handley, Samuel A Wickline, and James G Miller. Ultrasonic determination of the anisotropy of young's modulus of fixed tendon and fixed myocardium. *The Journal of the Acoustical Society of America*, 100(6):3933–3940, 1996.

[98] Po-Ling Kuo, Pai-Chi Li, and Meng-Lin Li. Elastic properties of tendon measured by two different approaches. *Ultrasound in medicine & biology*, 27(9):1275–1284, 2001.

[99] M Krueger-Franke, CH Siebert, and S Scherzer. Surgical treatment of ruptures of the achilles tendon: a review of long-term results. *British journal of sports medicine*, 29(2):121, 1995.

[100] James Gregory, Andrew L Hazel, and Tom Shearer. A microstructural model of tendon failure. *Journal of the mechanical behavior of biomedical materials*, 122:104665, 2021.

[101] C Hurschler, B Loitz-Ramage, and R Vanderby Jr. A structurally based stress-stretch relationship for tendon and ligament. *Journal of biomechanical engineering*, 119(4):392–399, 1997.

[102] Amir Hamedzadeh, T Christian Gasser, and Salvatore Federico. On the constitutive modelling of recruitment and damage of collagen fibres in soft biological tissues. *European Journal of Mechanics-A/Solids*, 72:483–496, 2018.

[103] Jared L Zitnay, Yang Li, Zhao Qin, Boi Hoa San, Baptiste Depalle, Shawn P Reese, Markus J Buehler, S Michael Yu, and Jeffrey A Weiss. Molecular level detection and localization of mechanical damage in collagen enabled by collagen hybridizing peptides. *Nature communications*, 8(1):1–12, 2017.

[104] Zhilei Liu Shen, Mohammad Reza Dodge, Harold Kahn, Roberto Ballarini, and Steven J Eppell. In vitro fracture testing of submicron diameter collagen fibril specimens. *Biophysical journal*, 99(6):1986–1995, 2010.

[105] Yehe Liu, Roberto Ballarini, and Steven J Eppell. Tension tests on mammalian collagen fibrils. *Interface focus*, 6(1):20150080, 2016.

[106] Noritaka Yamamoto. Tensile strength of single collagen fibrils isolated from tendons. *European Journal of Biophysics*, 5(1):1, 2017.

[107] Noritaka Yamamoto and Shun Nakamura. Relationships between the tensile strength and diameter of collagen fibrils isolated from mouse tail tendons. *Journal of Biomechanical Science and Engineering*, 12(3):16–00511, 2017.

[108] Joost AJ Van Der Rijt, Kees O Van Der Werf, Martin L Bennink, Pieter J Dijkstra, and Jan Feijen. Micromechanical testing of individual collagen fibrils. *Macromolecular bioscience*, 6(9):697–702, 2006.

[109] Hiroshi Miyazaki and Kozaburo Hayashi. Tensile tests of collagen fibers obtained from the rabbit patellar tendon. *Biomedical Microdevices*, 2(2):151–157, 1999.

[110] Mei Sun, Brianne K Connizzo, Sheila M Adams, Benjamin R Freedman, Richard J Wenstrup, Louis J Soslowsky, and David E Birk. Targeted deletion of collagen v in tendons and ligaments results in a classic ehlers-danlos syndrome joint phenotype. *The American journal of pathology*, 185(5):1436–1447, 2015.

[111] AN Natali, PG Pavan, EL Carniel, and C Dorow. A transversally isotropic elasto-damage constitutive model for the periodontal ligament. *Computer Methods in Biomechanics and Biomedical Engineering*, 6(5-6):329–336, 2003.

[112] AN Natali, PG Pavan, EL Carniel, ME Lucisano, and G Taglialavoro. Anisotropic elasto-damage constitutive model for the biomechanical analysis of tendons. *Medical engineering & physics*, 27(3):209–214, 2005.

[113] José F Rodríguez, Fernando Cacho, José A Bea, and Manuel Doblaré. A stochastic-structurally based three dimensional finite-strain damage model for fibrous soft tissue. *Journal of the Mechanics and Physics of Solids*, 54(4):864–886, 2006.

[114] V Alastrué, JF Rodríguez, B Calvo, and M Doblaré. Structural damage models for fibrous biological soft tissues. *International Journal of solids and Structures*, 44(18-19):5894–5911, 2007.

[115] Colin A Grant, David J Brockwell, Sheena E Radford, and Neil H Thomson. Effects of hydration on the mechanical response of individual collagen fibrils. *Applied Physics Letters*, 92(23):233902, 2008.

[116] Baptiste Depalle, Zhao Qin, Sandra J Shefelbine, and Markus J Buehler. Influence of cross-link structure, density and mechanical properties in the mesoscale deformation mechanisms of collagen fibrils. *Journal of the mechanical behavior of biomedical materials*, 52:1–13, 2015.

[117] Samuel J Baldwin, Josh Sampson, Christopher J Peacock, Meghan L Martin, Samuel P Veres, J Michael Lee, and Laurent Kreplak. A new longitudinal variation in the structure of collagen fibrils and its relationship to locations of mechanical damage susceptibility. *Journal of the mechanical behavior of biomedical materials*, 110:103849, 2020.

[118] Rene B Svensson, Stuart T Smith, Patrick J Moyer, and S Peter Magnusson. Effects of maturation and advanced glycation on tensile mechanics of collagen fibrils from rat tail and achilles tendons. *Acta biomaterialia*, 70:270–280, 2018.

[119] Benjamin E Peterson and Spencer E Szczesny. Dependence of tendon multiscale mechanics on sample gauge length is consistent with discontinuous collagen fibrils. *Acta Biomaterialia*, 117:302–309, 2020.

[120] HS Gupta, J Seto, S Krauss, P Boesecke, and HRC Screen. In situ multi-level analysis of viscoelastic deformation mechanisms in tendon collagen. *Journal of structural biology*, 169(2):183–191, 2010.

[121] Andrew S Quigley, Stéphane Bancelin, Dylan Deska-Gauthier, François Légaré, Laurent Kreplak, and Samuel P Veres. In tendons, differing physiological requirements lead to functionally distinct nanostructures. *Scientific reports*, 8(1):1–14, 2018.

[122] T. Christian Gasser. *Continuum Mechanics*, pages 91–165. Springer International Publishing, Cham, 2021.

Appendix A

A.1 The Cayley-Hamilton Theorem

The Cayley-Hamilton Theorem states that a 3×3 matrix $\mathbf{A}$ satisfies its own characteristic equation [37], i.e.

$$\mathbf{A}^3 - \mathbf{A}^2 \mathrm{Tr}\mathbf{A} + \frac{1}{2}\mathbf{A}\left[(\mathrm{Tr}\mathbf{A})^2 - \mathrm{Tr}\mathbf{A}^2\right] - \mathbf{I}\det\mathbf{A} = \mathbf{0}. \tag{A.1}$$

A.2 Derivation of crimped fibril strain energy function

After evaluating the integral in equation (2.54), we find that the stress in the fibres is equal to

$$\sigma(\lambda) = E(A + B\lambda + C\lambda^2 + D\lambda\log\lambda), \tag{A.2}$$

where A, B, C, and D are constants defined by

$$A = \begin{cases} 0, & \lambda < a, \\ \dfrac{-a^2}{(a-b)(a-c)}, & a \le \lambda < c, \\ \dfrac{-bc}{(a-b)(b-c)} - \dfrac{a}{a-b}, & c \le \lambda < b, \\ -1, & \lambda \ge b, \end{cases}$$

$$B = \begin{cases} 0, & \lambda < a, \\ \dfrac{2a\log a}{(a-b)(a-c)}, & a \le \lambda < c, \\ \dfrac{2a\log a}{(a-b)(a-c)} + \dfrac{2c\log c}{(a-c)(b-c)}, & c \le \lambda < b, \\ \dfrac{2a\log a}{(a-b)(a-c)} - \dfrac{2b\log b}{(a-b)(b-c)} + \dfrac{2c\log c}{(a-c)(b-c)}, & \lambda \ge b, \end{cases} \tag{A.3}$$

$$C = \begin{cases} 0, & \lambda < a, \\ \dfrac{1}{(a-b)(a-c)}, & a \le \lambda < c, \\ \dfrac{1}{(a-b)(b-c)}, & c \le \lambda < b, \\ 0, & \lambda \ge b, \end{cases}$$

$$D = \begin{cases} 0, & \lambda < a, \\ \dfrac{-2a}{(a-b)(a-c)}, & a \le \lambda < c, \\ \dfrac{-2b}{(a-b)(b-c)}, & c \le \lambda < b, \\ 0, & \lambda \ge b, \end{cases}$$

where a, b, and c are the lower bound, upper bound, and mode of the critical stretch distribution $\Lambda_C(\lambda_C)$, respectively. To get the corresponding strain energy function, we follow the procedure described in [43]. We equate the part of equation (2.36) associated with the fibres with equation (A.2), giving

$$2I_4 \frac{\partial W_f}{\partial I_4} = E(A + B\lambda + C\lambda^2 + D\lambda\log\lambda). \tag{A.4}$$

Using the fact that $I_4 = \lambda^2$ and solving for W_f, we arrive at

$$W_f(I_4) = \phi E \left(\frac{A}{2} \log I_4 + (B-D)\sqrt{I_4} + \frac{C}{2} I_4 + \frac{D}{2} \sqrt{I_4} \log I_4 + F \right), \tag{A.5}$$

where A, B, C, and D, are as defined in equation (A.3), but with $\lambda = \sqrt{I_4}$. The constant F can be found by enforcing $W_f(1) = 0$, leading to

$$F = \left(D - B - \frac{C}{2} \right) \Bigg|_{I_4=1}. \tag{A.6}$$

Assuming that the matrix is isotropic and can be represented as a Neo-Hookean material, we can write down the full strain energy function as

$$W(I_1, I_4) = (1-\phi)\frac{\mu}{2}(I_1 - 3) + \phi E \left(\frac{A}{2} \log I_4 + (B-D)\sqrt{I_4} + \frac{C}{2} I_4 + \frac{D}{2} \sqrt{I_4} \log I_4 + F \right). \tag{A.7}$$

Appendix B

B.1 Analytic expression for the stress in the elastic-rupture model

When using the ER model, it is possible to determine an analytic expression for the stress in the tendon when the fibril critical stretch follows a triangular distribution. In this case, the tendon stress is given by

$$\sigma_T^{ER}(\lambda) = A^{ER} + B^{ER}\lambda + C^{ER}\lambda^2 + D^{ER}\lambda\log\lambda, \tag{B.1}$$

where A^{ER}, B^{ER}, C^{ER}, and D^{ER} are piecewise constants defined by

$$A^{ER} = \begin{cases} 0, & \lambda < a \quad \text{and} \quad \lambda/\lambda_R < a, \\ \dfrac{-a^2}{(a-b)(a-c)}, & a \le \lambda < c \quad \text{and} \quad \lambda/\lambda_R < a, \\ \dfrac{-bc}{(a-b)(b-c)} - \dfrac{a}{a-b}, & c \le \lambda < b \quad \text{and} \quad \lambda/\lambda_R < a, \\ -1, & \lambda \ge b \quad \text{and} \quad \lambda/\lambda_R < a, \\ 0, & a \le \lambda < c \quad \text{and} \quad a \le \lambda/\lambda_R < c, \\ \dfrac{c^2}{(a-c)(c-b)}, & c \le \lambda < b \quad \text{and} \quad a \le \lambda/\lambda_R < c, \\ \dfrac{b}{a-b} + \dfrac{ac}{(a-b)(a-c)}, & \lambda \ge b \quad \text{and} \quad a \le \lambda/\lambda_R < c, \\ 0, & c \le \lambda < b \quad \text{and} \quad c \le \lambda/\lambda_R < b, \\ \dfrac{b^2}{(a-b)(b-c)}, & \lambda \ge b \quad \text{and} \quad c \le \lambda/\lambda_R < b, \\ 0, & \lambda \ge b \quad \text{and} \quad \lambda/\lambda_R \ge b, \end{cases}$$

$$B^{ER} = \begin{cases} 0, & \lambda < a \quad \text{and} \quad \lambda/\lambda_R < a, \\ \dfrac{2a\log a}{(a-b)(a-c)}, & a \le \lambda < c \quad \text{and} \quad \lambda/\lambda_R < a, \\ \dfrac{2a\log a}{(a-b)(a-c)} + \dfrac{2c\log c}{(a-c)(b-c)}, & c \le \lambda < b \quad \text{and} \quad \lambda/\lambda_R < a, \\ \dfrac{2a\log a}{(a-b)(a-c)} - \dfrac{2b\log b}{(a-b)(b-c)} + \dfrac{2c\log c}{(a-c)(b-c)}, & \lambda \ge b \quad \text{and} \quad \lambda/\lambda_R < a, \\ \dfrac{2a[\lambda_R(1-\log\lambda_R)-1]}{\lambda_R(a-b)(a-c)}, & a \le \lambda < c \quad \text{and} \quad a \le \lambda/\lambda_R < c, \\ \dfrac{2c\log c}{(a-c)(b-c)} + \dfrac{2a[\lambda_R(1-\log\lambda_R)-1]}{\lambda_R(a-b)(a-c)}, & c \le \lambda < b \quad \text{and} \quad a \le \lambda/\lambda_R < c, \\ \dfrac{-2b\log b}{(a-b)(b-c)} + \dfrac{2c\log c}{(a-c)(b-c)} + \dfrac{2a[\lambda_R(1-\log\lambda_R)-1]}{\lambda_R(a-b)(a-c)}, & \lambda \ge b \quad \text{and} \quad a \le \lambda/\lambda_R < c, \\ \dfrac{2b[\lambda_R(1-\log\lambda_R)-1]}{\lambda_R(a-b)(b-c)}, & c \le \lambda < b \quad \text{and} \quad c \le \lambda/\lambda_R < b, \\ \dfrac{-2b\log b}{(a-b)(b-c)} + \dfrac{2b[\lambda_R(1-\log\lambda_R)-1]}{\lambda_R(a-b)(b-c)}, & \lambda \ge b \quad \text{and} \quad c \le \lambda/\lambda_R < b, \\ 0, & \lambda \ge b \quad \text{and} \quad \lambda/\lambda_R \ge b, \end{cases}$$

$$C^{ER} = \begin{cases} 0, & \lambda < a \quad \text{and} \quad \lambda/\lambda_R < a, \\ \dfrac{1}{(a-b)(a-c)}, & a \le \lambda < c \quad \text{and} \quad \lambda/\lambda_R < a, \\ \dfrac{1}{(a-b)(b-c)}, & c \le \lambda < b \quad \text{and} \quad \lambda/\lambda_R < a, \\ 0, & \lambda \ge b \quad \text{and} \quad \lambda/\lambda_R < a, \\ \dfrac{(\lambda_R-1)^2}{\lambda_R^2(a-b)(a-c)}, & a \le \lambda < c \quad \text{and} \quad a \le \lambda/\lambda_R < c, \\ \dfrac{1}{\lambda_R^2(a-b)(a-c)} + \dfrac{1}{(a-b)(b-c)} - \dfrac{2}{\lambda_R(a-b)(a-c)}, & c \le \lambda < b \quad \text{and} \quad a \le \lambda/\lambda_R < c, \\ \dfrac{(1-2\lambda_R)}{\lambda_R^2(a-b)(a-c)}, & \lambda \ge b \quad \text{and} \quad a \le \lambda/\lambda_R < c, \\ \dfrac{(\lambda_R-1)^2}{\lambda_R^2(a-b)(b-c)}, & c \le \lambda < b \quad \text{and} \quad c \le \lambda/\lambda_R < b, \\ \dfrac{(1-2\lambda_R)}{\lambda_R^2(a-b)(b-c)}, & \lambda \ge b \quad \text{and} \quad c \le \lambda/\lambda_R < b, \\ 0, & \lambda \ge b \quad \text{and} \quad \lambda/\lambda_R \ge b, \end{cases}$$

$$D^{ER} = \begin{cases} 0, & \lambda < a \quad \text{and} \quad \lambda/\lambda_R < a, \\ \dfrac{-2a}{(a-b)(a-c)}, & a \le \lambda < c \quad \text{and} \quad \lambda/\lambda_R < a, \\ \dfrac{-2b}{(a-b)(b-c)}, & c \le \lambda < b \quad \text{and} \quad \lambda/\lambda_R < a, \\ 0, & \lambda \ge b \quad \text{and} \quad \lambda/\lambda_R < a, \\ 0, & a \le \lambda < c \quad \text{and} \quad a \le \lambda/\lambda_R < c, \\ \dfrac{-2b}{(a-b)(b-c)} + \dfrac{2a}{(a-b)(a-c)}, & c \le \lambda < b \quad \text{and} \quad a \le \lambda/\lambda_R < c, \\ \dfrac{2a}{(a-b)(a-c)}, & \lambda \ge b \quad \text{and} \quad a \le \lambda/\lambda_R < c, \\ 0, & c \le \lambda < b \quad \text{and} \quad c \le \lambda/\lambda_R < b, \\ \dfrac{2b}{(a-b)(b-c)}, & \lambda \ge b \quad \text{and} \quad c \le \lambda/\lambda_R < b, \\ 0, & \lambda \ge b \quad \text{and} \quad \lambda/\lambda_R \ge b, \end{cases}$$

B.2 Age breakdown of features present in stress-strain data

Age group	N_{total}	N_{linear}	N_{steps}	N_{either}	N_{both}
1.6 month	27	7 (26%)	16 (59%)	20 (74%)	3 (11%)
2.6 month	25	13 (52%)	14 (56%)	19 (76%)	8 (32%)
4.0 month	17	7 (41%)	7 (41%)	11 (65%)	3 (18%)
11.5 month	34	16 (47%)	3 (9%)	18 (53%)	1 (3%)
23.0 month	33	7 (21%)	3 (9%)	9 (27%)	1 (3%)
29.0 month	43	11 (26%)	4 (9%)	14 (33%)	1 (2%)
31.5 month	40	13 (33%)	3 (8%)	15 (38%)	1 (3%)
35.3 month	41	12 (29%)	4 (10%)	15 (37%)	1 (2%)
total:	260	86 (33%)	54 (21%)	121 (47%)	19 (7%)

Table B.1: The number of stress-strain curves from Goh *et al*. [20] containing second linear regions N_{linear}, and step-like failure behaviour N_{steps} for each age group of mice, as described in Section 4.2.3. N_{either} gives the number with either a second linear region, step-like failure behaviour, or both. The final column gives the number with both N_{both}.

B.3 Fitting parameters

This section contains histograms showing the spread of the fitting parameters obtained when we fit the EPD model to 223 sets of stress-strain data from Goh *et al*. [20]. For a tendon with a distribution of critical stretch $\Lambda_C(\lambda_C)$, we can find the mean crimp angle θ by computing

$$\theta = \int_1^\infty \arccos\left(\frac{1}{\lambda_C}\right)\Lambda_C(\lambda_C)\mathrm{d}\lambda_C. \tag{B.2}$$

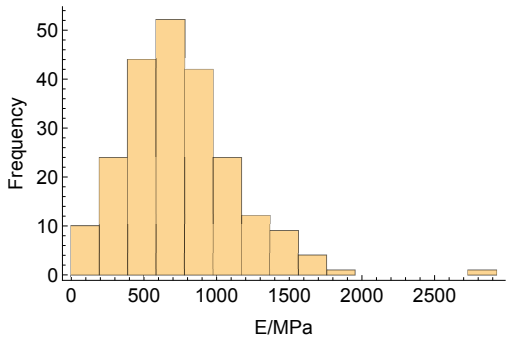

(a) Collagen fibril Young's modulus.

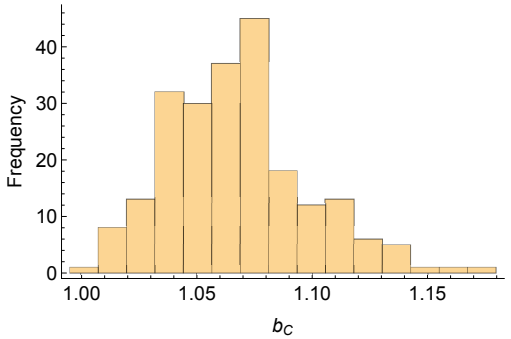

(b) Upper limit of the fibril critical stretch distribution.

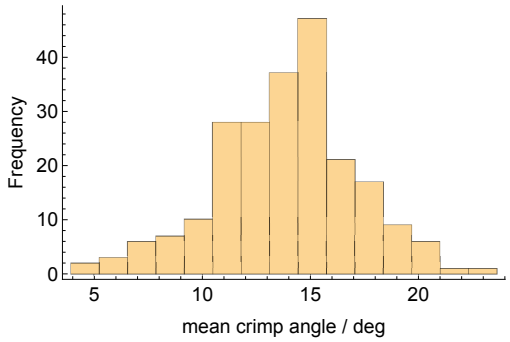

(c) Mean crimp angle found using equation (B.2).

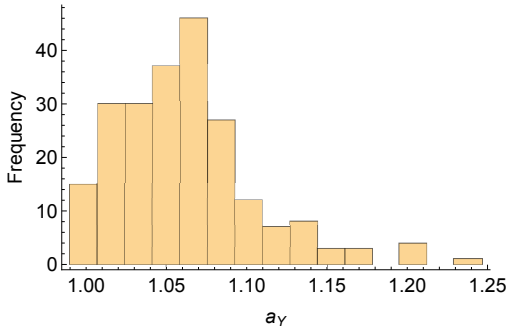

(d) Lower limit of fibril yield stretch distribution.

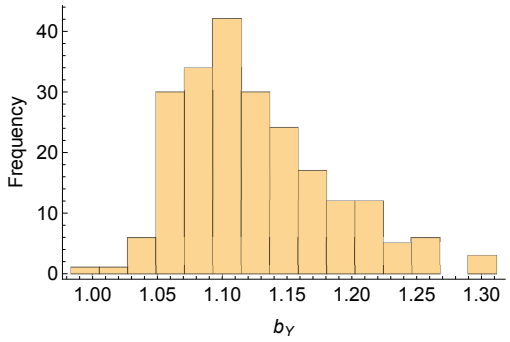

(e) Upper limit of the fibril yield stretch distribution.

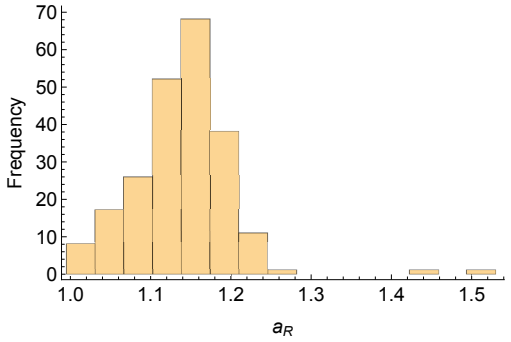

(f) Lower limit of the fibril rupture stretch distribution.

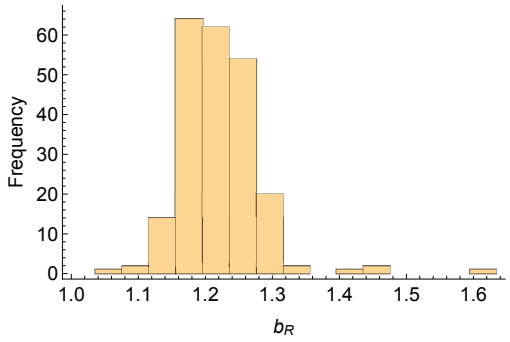

(g) Upper limit of the fibril rupture stretch distribution.

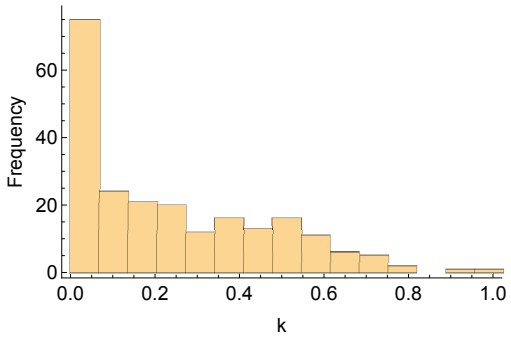

(h) The plasticity parameter k often did not change from its initial value of $k = 0$, which corresponds to the case of perfect plasticity.

Figure B.1: Histograms of the EPD model parameters found by applying the fitting routine described in Section 4.4 to stress-strain data from Goh *et al.* [20].